

**Master thesis and internship[BR]- Master's thesis : Virtual Shaker Testing:
Modelling, vibration analysis, and experimental validation of an electrodynamic
shaker model coupled to a test specimen[BR]- Integration Internship**

Auteur : Adam, Caroline

Promoteur(s) : Golinval, Jean-Claude

Faculté : Faculté des Sciences appliquées

Diplôme : Master en ingénieur civil en aérospatiale, à finalité spécialisée en "aerospace engineering"

Année académique : 2021-2022

URI/URL : <http://hdl.handle.net/2268.2/14589>

Avertissement à l'attention des usagers :

Tous les documents placés en accès ouvert sur le site le site MatheO sont protégés par le droit d'auteur. Conformément aux principes énoncés par la "Budapest Open Access Initiative"(BOAI, 2002), l'utilisateur du site peut lire, télécharger, copier, transmettre, imprimer, chercher ou faire un lien vers le texte intégral de ces documents, les disséquer pour les indexer, s'en servir de données pour un logiciel, ou s'en servir à toute autre fin légale (ou prévue par la réglementation relative au droit d'auteur). Toute utilisation du document à des fins commerciales est strictement interdite.

Par ailleurs, l'utilisateur s'engage à respecter les droits moraux de l'auteur, principalement le droit à l'intégrité de l'oeuvre et le droit de paternité et ce dans toute utilisation que l'utilisateur entreprend. Ainsi, à titre d'exemple, lorsqu'il reproduira un document par extrait ou dans son intégralité, l'utilisateur citera de manière complète les sources telles que mentionnées ci-dessus. Toute utilisation non explicitement autorisée ci-avant (telle que par exemple, la modification du document ou son résumé) nécessite l'autorisation préalable et expresse des auteurs ou de leurs ayants droit.

Master's thesis carried out to obtain the degree of Master of
Science in aerospace Engineering



**Virtual Shaker Testing:
Modelling, vibration analysis, and experimental
validation of an electrodynamic shaker model
coupled to a test specimen**

By ADAM Caroline (s172593)

Academic supervisor: GOLINVAL Jean-Claude

Industrial supervisor: HOFFAIT Sébastien

UNIVERSITY OF LIÈGE
School of Engineering and Computer Science
Academic Year 2021-2022

Acknowledgements

I would like to sincerely thank all the people who helped me in the realisation of this work.

First of all, I would like to particularly thank Sophie Denis and Sébastien Hoffait for all the efforts they have deployed in helping me realise the present research. They helped me a lot and gave me excellence advice to achieve this work. Thanks also to Louis Dechambre who guided me too through my work and who assisted me during all my experimental tests.

Secondly, I would like to thank Pr. Golinval who accepted to be the academic supervisor of my work but also Pr. Bröls to be part of my jury.

Then I would like to present my gratitude to the CEO Daniel Simon who accepted me as an intern in his company. Moreover, I am really grateful to the whole V2i staff who made this internship very pleasant. Thanks for their helpfulness and assistance when I needed it. They all helped me to integrate into the company and to grow from this interesting experience.

Particularly, I would like to thank Pierre Bernard and Loïc Verhees who helped me during the setup of the experimental parts of this work. And I also would like to thank Jérôme Ligot and Mathieu Bertha who shared their knowledge with me several times for the more theoretical aspects of my work.

Finally, I would like to thank my family and my friends for the support they have given me throughout my studies. Thank you for helping and advising me on countless occasions.

Abstract

In many engineering domains, it is important to be able to prove that a structure can sustain the vibrations it will undergo during its lifetime. In this purpose, the specimen is subjected to vibration test campaigns. However, these tests may become very expensive and time-consuming if they damage the structure to be tested, if some beating phenomena occur, if the device is over-tested, etc. To avoid such issues, a solution is to virtually simulate these tests in order to predict the interactions between the structure under test and the electrodynamic shaker. In this work, a virtual shaker testing is built to this end. Two methods are presented. The first one couples the finite element model of the specimen to the lumped parameter model of the shaker. The second one couples the experimental model of the specimen to the lumped parameter model of the shaker.

The first objective of this work is to design a lumped parameter model valid for any electromechanical shaker. A method is developed to compute the parameters involved in this model. This one is applied on two different shakers: a small 100-lbf shaker (i.e., 445 N) and a largest 120-kN shaker. Thanks to experimental tests, the parameters of these shakers are identified and introduced in the lumped mass model. Vibration campaigns are then simulated for these two shakers. The results are conclusive, the simulations are close to the physical test results. It allows to validate the models of these shakers.

The second objective of this study is to couple the model of the structure to be tested to the shaker model. The first method consists in building a finite element model of the specimen and to numerically couple it to the lumped mass model of the shaker. This method is tested on both shakers. For both of them, the amplitude of the peaks is well identified but not all peaks are detected. Indeed, some features of the system are not represented by the model. The second method predicts the frequency response function of a specimen coupled to the shaker based on the responses of both subsystems. To obtain the response of the specimen, a ping test is performed and an experimental superelement is built. This method is then experimentally validated.

Finally, a special emphasis is put on the model of the expander, a tooling that allows testing large structures on the 120-kN shaker. Its numerical model is updated thanks to experimental tests and is then coupled to its shaker model. This structure is very complex and difficult to model so the coupling to the shaker is not fully satisfying. But it allows to predict dangerous phenomena that would occur at high frequencies excitation.

Keywords: Virtual shaker testing, Electrodynamic shaker, Lumped parameter model, Parameter identification, Model updating, Testing prediction.

Contents

1	Introduction	1
1.1	Context and motivation	1
1.2	Objectives	3
1.3	Structure of the report	4
2	State-of-the-art	5
2.1	Electrodynamic shaker operation	5
2.2	Virtual Shaker Testing	7
2.3	Model of the electrodynamic shaker	8
2.3.1	Mechanical model	9
2.3.2	Electrical model	10
2.3.3	Electromechanical model	11
2.3.4	Shaker mechanical features	12
2.4	Parameter identification methods	13
3	Shaker modelling	16
3.1	Methodology	16
3.1.1	Mechanical parameters	17
3.1.2	Electrical parameters	21
3.1.3	Experimental measurements	23
3.1.4	Introduction of the parameters in the numerical model	24
3.2	Validation of the shaker model	25
3.2.1	Preliminary tests: 100-lbf shaker	25
3.2.2	More advanced tests: 120-kN shaker	29
3.3	Conclusion	43
4	Coupling of a specimen to the shaker	44
4.1	Methodology	44
4.1.1	Numerical model of a specimen coupled to the shaker	44
4.1.2	Experimental model of specimen coupled to the shaker	55
4.2	100-lbf shaker: beam case	58
4.2.1	Numerical coupling between specimen and shaker	58

4.2.2	Experimental coupling between specimen and shaker	61
4.3	120-kN shaker: head expander case	64
4.3.1	Model of the head expander	64
4.3.2	Experimental modal analysis: impact testing	67
4.3.3	Improvement of the model	72
4.3.4	Comparison of numerical and experimental modes and frequencies after model update	74
4.3.5	Validation of the model	78
4.3.6	Addition of the load support guidance	81
4.4	Conclusion	90
5	Conclusion and perspectives	91
	Appendices	94
	Appendix A Shaker specifications	95
	Appendix B LSCE method	96
	Appendix C PolyMAX stabilisation diagram	98
	Appendix D Vibration test reports	100
	Bibliography	110

Nomenclature

Abbreviations

CAD	Computer-Aided Design
DoF	Degree of Freedom
DUT	Device Under Test
EMA	Experimental Modal Analysis
FBS	Frequency-Based Substructuring
FEM	Finite Element Model
FFT	Fast Fourier Transform
FRF	Frequency Response Function
IRF	Impulse Response Function
LCR	Inductance, capacity and resistance
LSCE	Least-Squares Complex Exponential
LSFD	Least-Squares Frequency Domain
NRMSD	Normalised Root Mean Square Difference
p-LSCE	Polyreference Least-Squares Complex Exponential
PSD	Power Spectral Density
RMS	Root Mean Square
RMSD	Root Mean Square Difference
SE	Super-Element

VPT Virtual Point Transformation

VST Virtual Shaker Testing

Symbols

ϕ	Matrix of transformation
ψ	Eigenmode vector
\mathbf{C}	Damping matrix
\mathbf{K}	Stiffness matrix
\mathbf{M}	Mass matrix
Δf	Frequency resolution
Δt	Time resolution
λ_k	Pole
ω_k	Natural pulsation
ζ_k	Damping ratio
B	Magnetic field strength
c_b	Damping of shaker body suspensions
c_c	Damping of shaker coil suspensions
c_s	Damping of shaker table suspensions
E_{bemf}	Back electromotive force
$f_{0_{HF}}$	Second natural frequency of non loaded test
$f_{0_{LF}}$	First natural frequency of non loaded test

$f_{l_{HF}}$	Second natural frequency of loaded test	K_v	Voltage/velocity coefficient
		L	Coil inductance
$f_{l_{LF}}$	First natural frequency of loaded test	l	Coil length per turn
g	Amplifier gain	m_b	Mass of the shaker body
$H_{acc,i_{HF}}$	Acceleration-over-current FRF at high frequency	m_c	Mass of the shaker coil
$H_{acc,i_{LF}}$	Acceleration-over-current FRF at low frequency	m_t	Mass of the shaker table
		n	Number of coil turns
I	Laplace transform of the current i	R	Coil resistance
i	Current flowing through the coil	T	Acquisition period of time
k_b	Stiffness of shaker body suspensions	V	Voltage at coil terminals
k_c	Stiffness of shaker coil suspensions	V_{in}	Output amplifier voltage
K_f	Force/current coefficient	V_{out}	Input amplifier voltage
k_g	Stiffness of the bearing guidance	W	Frequency bandwidth of interest
k_i	Stiffness of the isolation support	X_t	Laplace transform of the table displacement x_t
k_s	Stiffness of shaker table suspensions		

Chapter 1

Introduction

1.1 Context and motivation

In the engineering domain, vibration campaigns are performed to validate structures before they can be released. The aim is to ensure they will sustain a certain level of vibrations during their lifetime. The real operational conditions must be accurately represented during this kind of campaign to simulate precisely the stresses they will undergo in their real world lifetime.

However, vibration campaigns are not always easily performed. Indeed, some vibration tests are difficult to pass on specimens. For example, if the ratio between the mass of the tested structure and the mass of the shaker is too large, the coupling between the shaker and the specimen may become problematic. Alternatively, if the required level of acceleration is high or if the control point is in a wobbly position, the controllers that avoid a too large table acceleration may not allow to pass the test. Moreover, there usually are some interactions between the structure to be tested, the electrodynamic shaker and the vibration controller. Another issue is that such campaigns may be expensive and time-consuming. And longer tests may postpone the industrialisation of the prototypes and thus lead to a significant monetary loss.

Numerically simulating the test campaigns allows reducing these issues. Indeed, if these vibration tests can be simulated before doing any physical test, it reduces the risk to damage the shaker or the structure being tested during qualification test campaigns. It is also a gain of time because it permits to predict the dynamic behaviour and to properly define in advance the parameters involved in the physical test. The test execution can then be optimised and over-testing issues are avoided.

This defines the concept of virtual shaker testing. It allows to simulate the behaviour of any electrodynamic shaker but also its interaction with the structure to be tested on

this shaker. A virtual shaker testing is usually composed of three parts. The first one is the model of the shaker. The second one is the model of the specimen coupled to the model of the shaker. The last one is to simulate the control of a test on this shaker. However, the virtual shaker testing is a domain not yet fully addressed and some researches still need to be done.

Obviously, the requirements to represent closely the reality in a simulating environment are complex. The boundary conditions between the structure under test and the shaker device must accurately represent the reality. All the parameters that could have an impact on the dynamic behaviour of the structure under test have to be taken into account. However, the system made of the shaker and the structure to be tested constitute a very complex system. Not every detail need to be modelled, only what is strictly necessary to reproduce the targeted behaviour of the specimen.

This work is realised in the context of an internship in the V2i company. One of their main core activities is to perform vibration campaigns for other enterprises in order to improve industrial safety and reliability. They offer their services with theoretical and experimental expertise. All researches for this master thesis are done inside this company with the help of its employees and by using their equipment, hardware and software, for the experimental parts.

The usefulness of such a virtual shaker testing can be shown by a simple example of test at V2i. Clients had asked to test a heavy equipment for transport application. It had a more than 400-kg mass. They needed a support to test it so that it would be suspended and they did not want the equipment/tooling assembly to have natural frequencies below 20 Hz. V2i had then designed a tooling responding to these requests. The equipment and the tooling had first been tested individually and they satisfied the clients' specifications. After that, the assembly had been tested horizontally on the table of the shaker and the requests were still valid. But, when it has been tested on the expander in the vertical configuration, the assembly had natural frequencies in the vicinity of 10 Hz. This had scared the clients but it was only a rigid body mode resulting from the coupling between the assembly equipment/tooling and the shaker. To conclude, if these tests could have been first simulated these frightening results would have been predicted by the model.

In fact, when V2i receives a customer's demand, they get some specifications. They then check if these are compatible with the maximum force that the shaker can provide and if the required displacement of the table of the shaker will not be too large. The big advantage of the virtual shaker testing is that it could predict the coupling of the device

under test with the shaker and could predict the feasibility of a test.

1.2 Objectives

The global objective of this work is to implement a virtual shaker model. This master thesis is thus divided in two main parts: the modelling of an electrodynamic shaker by a lumped parameter model, and the coupling of the specimen model to the shaker model.

The first objective is to design, implement and validate a robust methodology to create an electromechanical model of any electrodynamic shaker. In order to numerically simulate a shaker, it is first needed to determine the lumped parameters involved in its model. Few pieces of information are given by the manufacturers about the masses of the different components, their stiffness or damping coefficients, etc. It is therefore very difficult to identify all the parameters involved in the model. As a consequence, it is needed to develop a method that will allow to identify these lumped parameters.

However, the aim of the virtual shaker testing is to predict how a structure reacts when it is tested. Therefore, the second objective of this work is to design, implement and validate a methodology to couple to the shaker model a numerical or an experimental model of a specimen or an accessory such as the expander. The expander is an additional tooling which is fixed on the shaker to allow to test relatively large structures when shakers vibrate in the vertical configuration. It is needed to correctly model it to introduce it in the virtual shaker testing.

It has to be noted that there exists shakers of very different sizes. It can go from tiny shakers with for example 5-N forces to large shaker with forces of several thousands of Newton. In this work, the targeted size is rather the latter. However, the developed methods will be tried on a 100-lbf shaker (i.e., 445 N) before being applied on the largest one. To visualise this difference of sizes, three different shakers are shown: a 5-N shaker in Figure 1.1, a 100-N shaker in Figure 1.2 and a 120-kN shaker in Figure 1.3.



Figure 1.1: 5-N Shaker.



Figure 1.2: 100-N shaker.



Figure 1.3: 120-kN shaker.

1.3 Structure of the report

This work is divided in three main parts. The first one briefly presents what has already been done in the domain of the virtual shaker testing. The second one explains how to model an electrodynamic shaker and the last one describes how to couple the model of a specimen to the numerical model of the shaker.

The first part of this study details how an electrodynamic shaker works, and how all its components are connected. After that, the aim of a virtual shaker testing and its main constituents are presented. It is then shown how to model the shaker, its mechanical and electrical parts. The whole electromechanical model is then constituted. The features and the limitations of a shaker are introduced. Finally, existing methods to identify the model parameters are proposed.

The second part of this work explains how to model a shaker. The methodology to follow is first presented then is validated with two practical cases. Two different shakers are modelled and the simulations are compared with experimental tests.

Finally, the third part explains how to couple the model of a specimen to the model of the shaker thanks to a numerical and an experimental specimen model. Again, this methodology is applied to both shakers. Moreover, in this chapter, the focus is done on a specific structure: the expander, the studied specimen. Its behaviour is extensively studied.

Chapter 2

State-of-the-art

In this chapter, the components of an electrodynamic shaker are described so that the reader clearly understands how it works. After that, it is explained how a Virtual Shaker Testing (VST) is developed and what has already been done within V2i company on this topic. A generic model of the shaker is then built and both electrical and mechanical sides are studied. Finally, the existing methods for identifying the parameters of a shaker are presented.

2.1 Electrodynamic shaker operation

The structure of an electrodynamic shaker has the same fundamentals as a loudspeaker: a vibration is induced by a current flowing in a coil that is suspended within a magnetic field. However, an electrodynamic shaker is more robust and heavier than a loudspeaker. Guides and suspensions are added. The shaker can be considered as an electro-mechanical system [1].

Figure 2.1 illustrates the following explanations about the physics of the electrodynamic shaker. As seen on this diagram, the coil of wire is suspended in a radial magnetic field, acting in a perpendicular plane to the coil axis. When a current flows through this coil, a longitudinal force proportional to this current is created and transmitted to the table where the specimen is fixed [2]. This is what makes the specimen under test vibrate.

A complex permeable arrangement must be constructed to create the radial magnetic field [3]: it is produced thanks to a magnetic permeable circuit around a polarised cylindrical magnet. This last one is a permanent magnet for small shakers and an electro-magnet for large shakers. The two poles of this magnet are placed in front of each other thanks to an inner pole and an outer pole. The inner pole is connected to the north face of the magnet to transmit the flux. The outer pole is attached to the south face. This outer pole is made of a permeable disk. This permeable disk is linked to a permeable

tube which is then connected to an hollow permeable disk; the coil is suspended in this hole. This allows to transmit the flux from the south face of the magnet to this disk. Therefore, the inner pole, which is inside the coil, is north-polarised while the outer pole, that surrounds the coil, is south-polarised. The radial flux normal to the coil axis is thus created. The air gaps between these poles have to be as small as possible in order to minimise the reluctance of the magnetic circuit. The fixed magnetic field is then maximised.

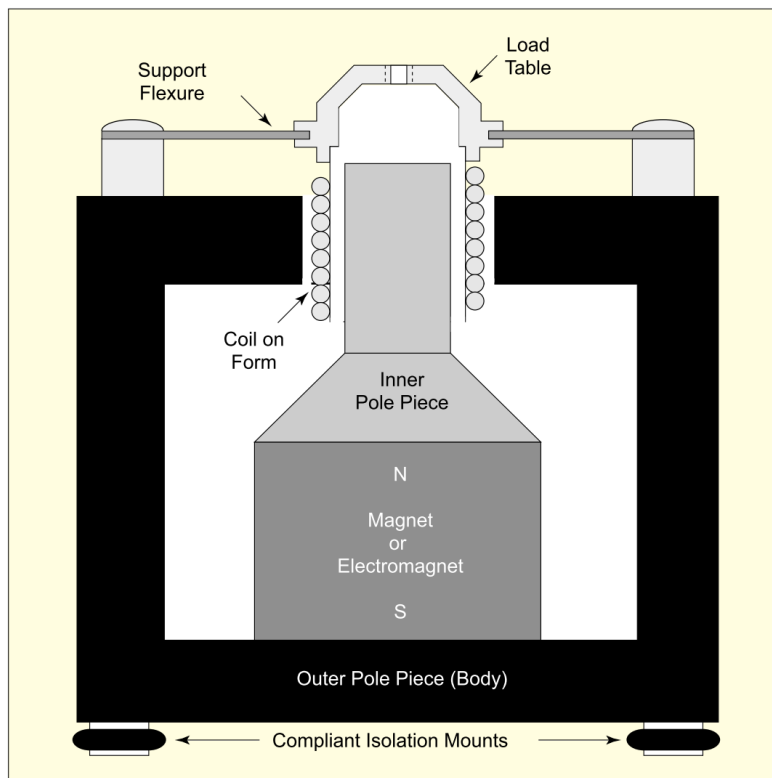


Figure 2.1: Section view of shaker mechanical structure [2].

The coil is centred in the gap between the inner and outer poles and moves axially (i.e. vertically in Figure 2.1) with no motion in the other directions. To avoid lateral motions, an elastic suspension system is used, called *support flexure*. This is made of flexible metal sheets that have a high yield strength. It is illustrated in Figure 2.2. Intuitively, it can be seen that this piece allows a vertical motion but that its torsional rigidity is significant.



Figure 2.2: Support flexure of the coil.

The piece that allows to link the load table and the coil is called the *coil on form*. In older designs, it was made of a thin stiff tube. The coil was welded around its external diameter and the upper extremity is fixed to the table. In modern designs, an epoxy stabilised coil is directly fixed to a light magnesium table structure by using epoxy bonding techniques.

The table, the coil and the coil on form are the moving elements. They constitute the *shaker armature* while the exciter base holding the magnetic elements is called the *shaker body* [4]. It usually is isolated from the ground thanks to pneumatic suspensions.

2.2 Virtual Shaker Testing

The aim of the virtual shaker testing is to simulate a vibration campaign of a specific structure on a virtual electrodynamic shaker. To build this virtual testing, three different components must be modelled: the shaker, the structure and the control system [5]. They constitute the three main blocks shown in Figure 2.3. The first step is therefore to model the electrodynamic shaker. The second one is to represent the device that it is intended to be tested and then to couple it to the model of the shaker. The last step is to implement the model of the controller that controls the shaker during experimental vibration test campaigns.

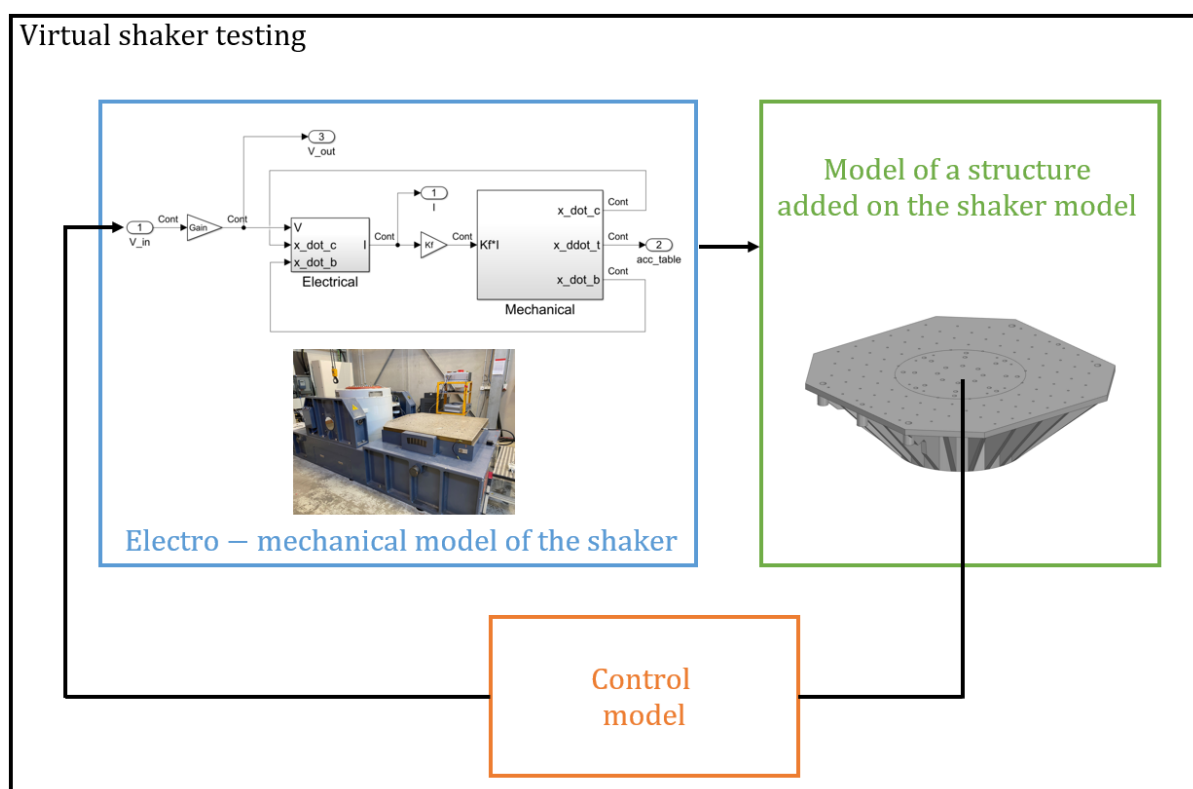


Figure 2.3: Principle of virtual shaker testing.

The first objective is to model an electrodynamic shaker. In this master thesis, a special focus is made on a large 120-kN shaker. A model of a similar electrodynamic shaker is already existing, developed in V2i [6]. However, the shaker is not exactly the same and the identified parameters in this previous model have been determined manually. No method has been followed to determine the lumped parameters.

In this work, only the vertical configuration of the shaker is modelled but it could also be done for the horizontal position. V2i have tried to model this horizontal operation mode but it is far more complex [6]. Indeed, it will be seen later that in the vertical position, the shaker may be modelled by a spring-mass system. In the horizontal position, the table of the shaker slides on an oil film rather than being maintained by the flexure mounts. The dynamics of this coupling system as well as the identification of the parameters are much more complex.

The second stage to build a VST is the coupling of a specimen model to the shaker model. To establish this coupling, a superelement is used. It is connected to the table of the shaker and the reaction of the structure on the shaker table is computed. Moreover, it gives access to the information of any point of the specimen so that the controller model can be applied on any point of the structure model.

The last stage of the VST is to integrate the controller model. References [6] and [7] explain what has already been done within V2i about VST. They have used a controller model, provided by *Siemens LMS*, to build a complete virtual shaker model. The aim is to imitate the controller hardware that is used to operate the shaker during experimental tests. However, this will not be used in the present research work because its application field is very limited. Indeed, it can not operate beyond 200 Hz while the goal of the VST developed in this work is to predict the behaviour of a structure and the shaker for a broad frequency range. The goal is to model dynamic phenomena at least up to 2 000 Hz because it is the limit of allowable excitation frequencies specified in the concerned shaker norms. A new model of the controller could be developed but it is beyond the scope of this work. Therefore, no control will be used in this work and the latter will focus only on the two first blocks of the VST: the shaker model and the coupling of a specimen model to the shaker model.

2.3 Model of the electrodynamic shaker

There are different ways to model an electrodynamic shaker. The level of complexity depends on the objectives of this modelling. For example, in the space domain, spacecrafts experience a large variety of loads in all the directions and need accurate testing sys-

tems. Performing vibration test campaigns is extremely expensive and risky. A specific test specimen is often produced exclusively for testing purposes and this piece is often unique. No mistake can be afforded. A reliable numerical model is therefore a valuable asset to anticipate the test results, and maybe to replace some of the (costly) real test sequences. For example, to mimic loads undergone by a satellite launcher, the ESA has developed the HYDRA shaker [8]. This six degrees-of-freedom table shaker is made of height hydraulic actuators. In order to virtually test the interactions between the shaker and the spacecraft, the ESA has built a finite element of the whole HYDRA structure [5]. This can be observed in Figure 2.4.

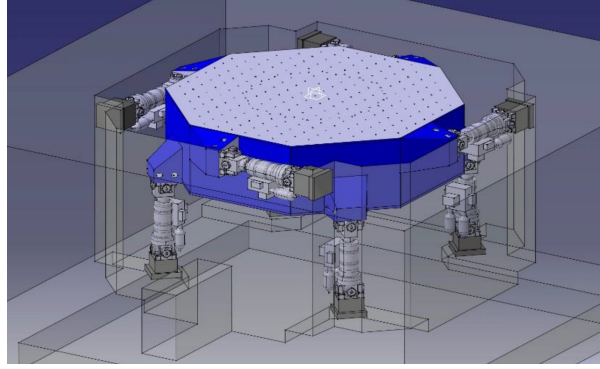


Figure 2.4: CAD model of the HYDRA shaker [5].

However, in this master thesis, it is assumed that the shaker table is infinitely rigid and that the table vibrates in the vertical direction only. Therefore, such a complete model is not needed. In this case, the electrodynamic shaker may be simply modelled by lumped masses and a one-dimensional model can be considered.

Different electromechanical models using lumped parameters have been developed in numerous previous works. Most of them are one dimensional with either two degrees of freedom as in [1] and [9] or three degrees of freedom as it is in [2, 4, 10, 11, 12]. In these works, the shaker is represented by a simple lumped-mass model and only the vertical degrees of freedom are first considered. However, in [13], the rotational degrees of freedom are taken into account to be able to represent the torsion or in-plane rotation.

2.3.1 Mechanical model

In this work, a 3-DoF one-dimensional mechanical model is used. These are represented by the vertical translations of three different masses as illustrated in Figure 2.5: the mass of the coil m_c , the mass of the shaker body m_b and the mass of the shaker table m_t [2]. The vertical displacements relative to these masses are respectively denoted x_c , x_b , and x_t .

The connections between these elements are also shown in Figure 2.5. The suspensions of the table that link it to the shaker body of the shaker are modelled by a spring k_s and a damper c_s . Additionally, since the armature is considered as being elastic, the coil and the table do not move rigidly. They are connected by a spring k_c and a damper c_c . Finally, the isolation system of the shaker from the ground is modelled as a spring k_b and a damper c_b .

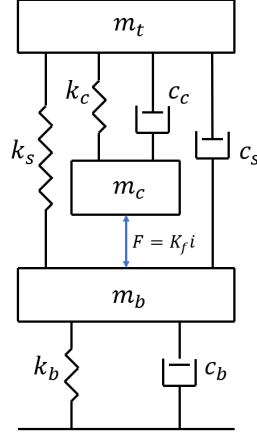


Figure 2.5: Mechanical model [2].

2.3.2 Electrical model

Such a mechanical model is then coupled to an electrical model, illustrated in Figure 2.6.

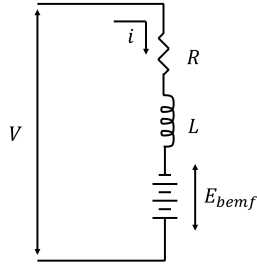


Figure 2.6: Electrical model [2].

This coupling between the mechanical and electrical domains is two-sided [12]. Firstly, when a current passes through the coil, a force proportional to the current acts on it. The magnitude of this force F [N] is given by *Ampere's law* which writes:

$$F = Blni = K_f i, \quad (2.1)$$

where B is the magnetic field strength [T], l is the coil length per turn [m], n is the number of turns [-], i is the current flowing through the coil [A], and K_f is the force/current coefficient [N/A]. This force applies simultaneously on the mass of the coil and on the

mass of the shaker body in opposite direction. The mass of the latter must therefore be significantly larger than the mass of the coil/table assembly.

Secondly, a voltage is created at the terminals of the coil when it moves inside the magnetic field. This voltage is proportional to the velocity of the coil according to *Faraday's law* which writes:

$$E_{bemf} = Bln\dot{x}_c = K_v\dot{x}_c, \quad (2.2)$$

where E_{bemf} is the back electromotive force [V], \dot{x}_c is the relative velocity of the coil with respect to the magnetic field [m/s], and K_v is the voltage/velocity coefficient [V/(m/s)].

The coil is defined by its electrical resistance R and inductance L [9]. These induce a complex electrical impedance $Z = R + j\omega L$ at the input terminals of the shaker [2], where ω is the pulsation. The electrical circuit may then be modelled by the following equation:

$$V(t) = Ri(t) + L\frac{di(t)}{dt} + E_{bemf}(t). \quad (2.3)$$

And by using Eq. 2.2, it comes:

$$V(t) = L\frac{di(t)}{dt} + Ri(t) + K_v\dot{x}_c. \quad (2.4)$$

This equation models the electrical part of an electrodynamic shaker.

2.3.3 Electromechanical model

As it is shown in [2], by integrating the equations of motion in Equation 2.4 as a function of the current passing through the coil, the equations of the system are obtained (cf. Equation 2.5). Further chapters explain how to solve these equations to simulate the dynamic behaviour of the shaker.

$$\begin{aligned} \begin{bmatrix} m_c & 0 & 0 & 0 \\ 0 & m_t & 0 & 0 \\ 0 & 0 & m_b & 0 \\ 0 & 0 & 0 & 0 \end{bmatrix} \begin{pmatrix} \ddot{x}_c \\ \ddot{x}_t \\ \ddot{x}_b \\ \frac{d^2 i}{dt^2} \end{pmatrix} + \begin{bmatrix} c_c & -c_c & 0 & 0 \\ -c_c & c_c + c_s & -c_s & 0 \\ 0 & -c_s & c_s + c_b & 0 \\ -K_v & 0 & K_v & L \end{bmatrix} \begin{pmatrix} \dot{x}_c \\ \dot{x}_t \\ \dot{x}_b \\ \frac{di}{dt} \end{pmatrix} + \\ \begin{bmatrix} k_c & -k_c & 0 & -K_f \\ -k_c & k_c + k_s & -k_s & 0 \\ 0 & -k_s & k_s + k_b & K_f \\ 0 & 0 & 0 & R \end{bmatrix} \begin{pmatrix} x_c \\ x_t \\ x_b \\ i \end{pmatrix} = \begin{pmatrix} 0 \\ 0 \\ 0 \\ V \end{pmatrix}. \end{aligned} \quad (2.5)$$

2.3.4 Shaker mechanical features

On electrodynamic shakers, the isolation mounts mode is usually identified at low frequency, the suspension mode at medium frequency and the coil mode at high frequency [14]. Two of these modes are easily observed on the measured Frequency Response Functions (FRFs) of the acceleration of the table over the current flowing through the coil. A theoretical example is shown in Figure 2.7. There is a first peak appearing on this function which is highly damped. It corresponds to the suspension mode.

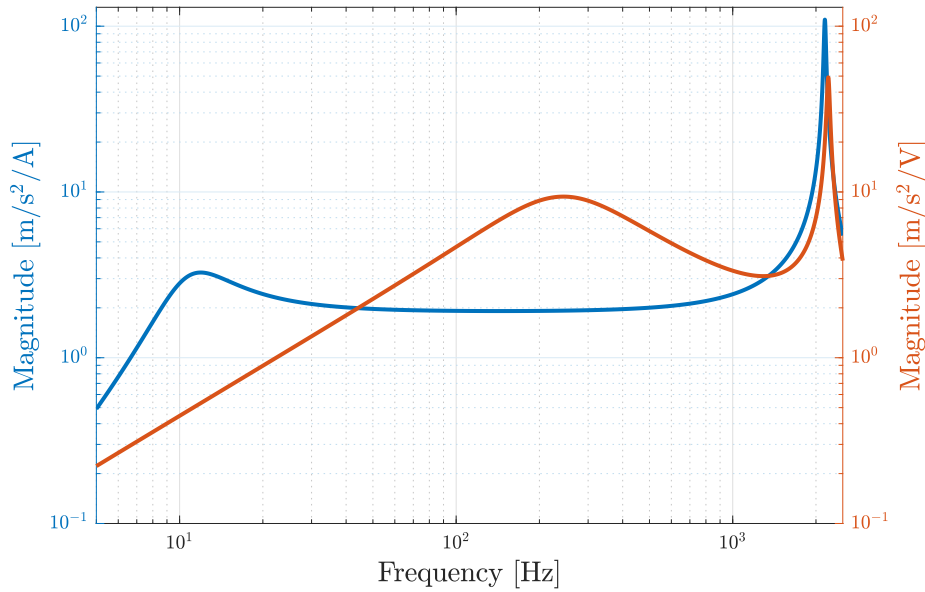


Figure 2.7: Table acceleration-over-current (blue) and over-voltage (orange) FRFs.

There is a second peak at higher frequency which corresponds to the coil mode. This mode is the most dangerous. Indeed, as it is observed in Figure 2.7, the reaction of the system is much higher than for the first mode. It is not advised to use the shaker at the corresponding frequency because it could break the coil and it would of course cost a lot of money. At first, the repair of a coil is very expensive. Moreover, the repairing takes time and during this time, the shaker is unusable. In V2i company, the customers who order some tests pay per hour so an unusable shaker wastes a lot of money.

One can notice that the isolation mount mode is not visible in Figure 2.7. It is because on an electrodynamic shaker, the natural frequency of the body is positioned below the excitation frequencies.

It can be seen in Figure 2.7 that compared to the acceleration-over-current FRF, the coil mode identified with the acceleration-over-voltage FRF has a smaller amplitude.

This is due to the electromagnetic damping applied by the cross-coupling between the electrical and the mechanical parts of the shaker (by the coefficients K_v and K_f) [2].

It can be assumed that at the peak relative to the suspension mode, the coil and the table move rigidly together, move in phase. However, at the high frequency peak, they move out of phase. The moving elements are then in resonance.

It is important to note that an electrodynamic shaker has some limitations in terms of performances. The causes of these limitations are frequency dependent as it is explained in reference [2]. Indeed, at low frequency, the limiting factor is the designed stroke of the table. It is what restricts the displacement of the table. In the middle frequency range, there is a table velocity limit. It is due to the maximum voltage output of the power amplifier and to the back electromotive force that the shaker is able to generate. The table operation is therefore limited by the maximum RMS current that the coil of the shaker can tolerate. At high frequency, the table operation is limited by force and finally by voltage.

In V2i company, the limitations of the shakers are gathered in a *Specification sheet*. This can be found in the Appendix A in Figure A.1. It allows to decide if the customer's requirements are feasible. One can note that without a virtual shaker testing, this is the only way to determine in advance if a test is realistic or not. But the database that supports this specification sheet are not exhaustive, so some phenomena could be overlooked.

2.4 Parameter identification methods

It is now understood how an electrodynamic shaker works and how a virtual shaker testing is built. With the aim of achieving the first block of a VST (cf. Figure 2.3), the generic model of a shaker has been defined in Section 2.3. The next step is then to determine the lumped parameters of this model: the masses, stiffness and damping coefficients defined in the previous sections. In this section, the different methods of identification investigated are presented.

For shakers having a force below 50 N, it is common to realise *nail tests*. In [3], the model of the electrodynamic shaker is only constituted by two degrees of freedom: the vertical displacement of the table and the vertical displacement of the coil. The idea of this test is then to block the vertical displacement of the shaker table with a finger nail and then release it abruptly. The output voltage at the terminals of the coil is measured and the frequency and time responses are monitored. This test is realised with no load

on the shaker, and with a small mass whose weight is accurately known. The natural frequencies of the system are then identified. Their numerical expressions involving the mechanical parameters being known, these frequencies are easily computed numerically.

A similar method to determine the mechanical parameters of the shaker is the *blocking structure* [1]. It is only possible to use it for small shakers that are only modelled by two degrees of freedom. This method consists in blocking alternatively one of them to end up with a one degree of freedom system and let it oscillate to study it. The system is then mounted on a larger shaker and is excited by a sine sweep signal. The system response being registered, the parameters of the shaker are then identified by comparison with the response of a single degree of freedom system using a least-squares estimation.

Another idea is to determine the mechanical parameters of the shaker by experimental modal analysis. In [9], impacts are performed on the table and the body with an impulse hammer while the table acceleration response is recorded. The modal parameters are then determined with a modal identification method. The response functions are then synthesised. However, this method is not ideal for highly damped structures. If the table flexure is largely attenuated, resonance peaks do not appear in every FRF. For example, if the impact is performed on the table, the table mode (or suspension mode) clearly appears in the FRF while the body mode is not observed. In the contrary, if the impact is done on the shaker body, the suspension mode is not observed in its FRF while the isolation mode is. It can make it difficult to identify properly the modal parameters.

These three first methods are only well suited for small shakers. Another one that can be applied on larger shaker will be investigated more deeply in the following chapters of this work. As in the first presented method, two tests have to be performed: an unloaded test and one with a mass added on the table. For these two tests, the acceleration of the table as well as the current flowing through the coil of the shaker must be recorded to obtain the frequency response function of the acceleration over current [15]. Starting from the equations of the mechanical model, after some calculations, its numerical expression is obtained. The values of the natural frequencies being determined experimentally, all the mechanical parameters may be identified.

It has to be noted that for these four presented methods, only the mechanical parameters are determined. In fact, in each of these sources, the electrical parameters such as the resistance and the inductance of the coil have simply been measured with a LCR-meter. However, in these articles, there is no experimental verification of what these LCR-meters exactly measure. And they do not take into account the frequency dependency of the

resistance and the inductance. Moreover, the aim of this work is to determine all the numerical parameters automatically, the mechanical ones as well as the electrical ones.

In [10], the electrical parameters of the shaker have been determined thanks to the expression of the frequency response function of the voltage at the terminals of the coil over the current flowing through it. This function is measured experimentally and the parameters of the numerical expression are determined by solving a least-squares problem between the two functions.

Chapter 3

Shaker modelling

In this chapter, a methodology is established to implement a virtual shaker system for any electrodynamic shaker. Test campaigns are performed on two different shakers so that the methodology is used and its performance is assessed.

3.1 Methodology

The electromechanical model of the shaker has been theoretically defined in the previous chapter. The equations of the model of the electrodynamic shaker written in Equation 2.5 are now implemented in the *Simulink* software package. It is a MATLAB extension that provides a block diagram environment which allows to design systems and to simulate their operation. This software has been chosen because it is an open software by opposition to other softwares where the codes cannot be modified. In *Simulink*, every parameter can be changed, the time resolution can be chosen and if a control module is added, it can be edited. The electromechanical model implemented in this software is shown in Figure 3.1.

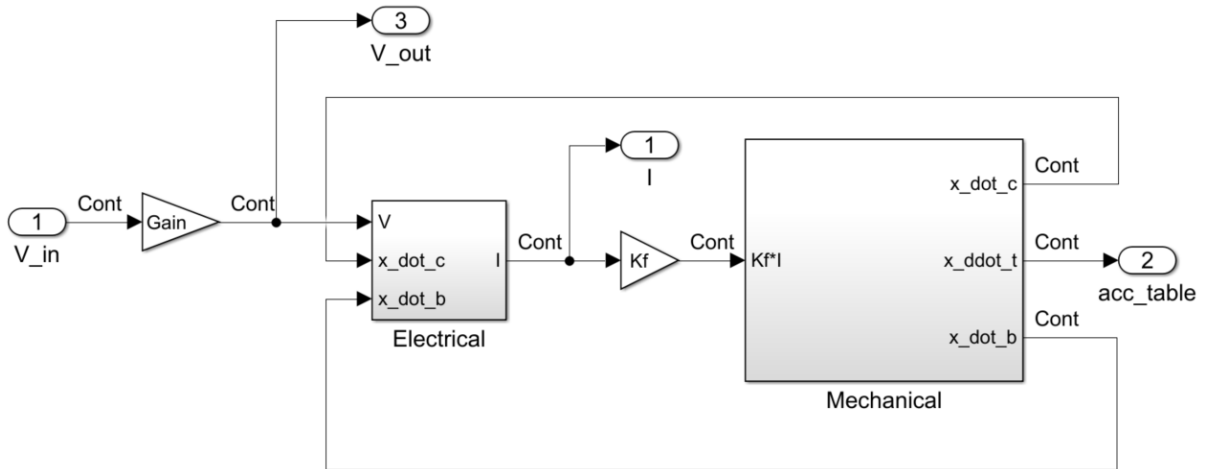


Figure 3.1: Electro-mechanical model of a shaker implemented in *Simulink*.

In order to simulate the dynamics of the shaker, the parameters of the numerical model appearing in these equations must be identified. A method has to be developed to estimate them so that the virtual shaker model can be used. In this section, a method to optimise the mechanical parameters is explained in a first time. An analytical expression is thus found for the m_c and m_t masses, for the c_c and c_s damping coefficients, for the k_c and k_s stiffness coefficients and for the K_v coupling parameter. After that, the R and L electrical parameters optimisation is developed.

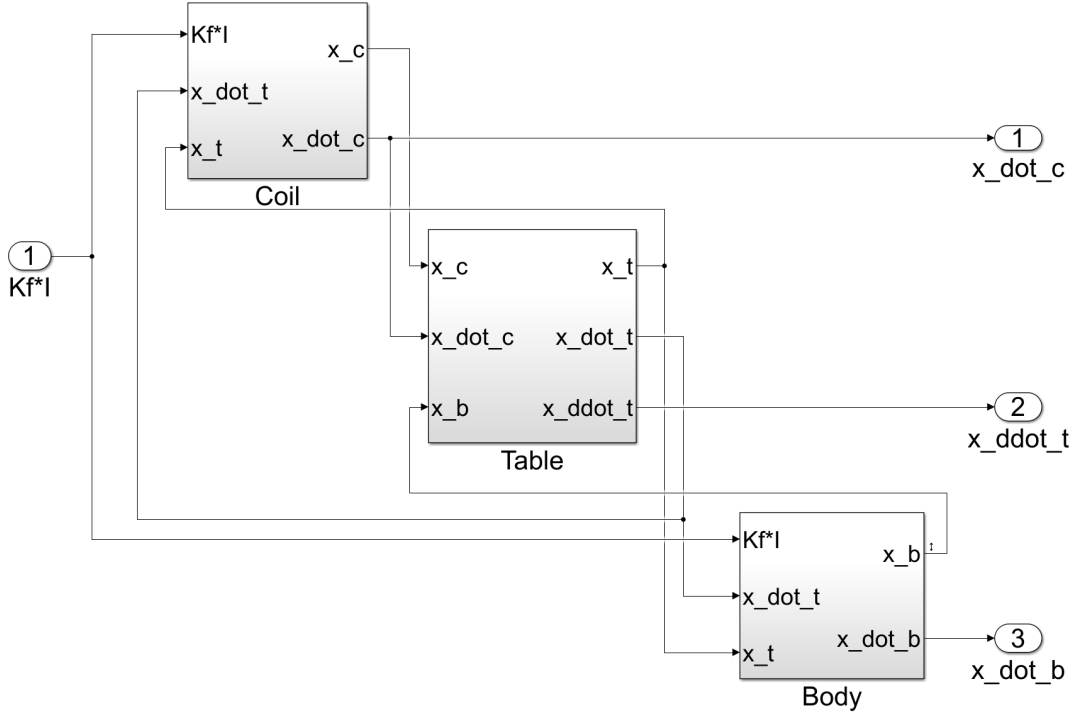
3.1.1 Mechanical parameters

To identify the mechanical parameters of the numerical model, the analytical expression of the acceleration-over-current FRF is used as it is explained in [15]. The latter can be experimentally measured and its numerical expression is easily obtained. Therefore, the two frequency response functions may be compared in order to determine the parameters.

In a first time, it is assumed that when a mass-load is added on the table of the shaker, it is rigidly attached to it. Therefore, instead of using a superelement, the load m_l is modelled by being added to the mass of the table. In this case, m_t can be replaced by $m_t + m_l$ in the model. This also makes the assumption that the mass acts like a point. This is not the case anymore with a superelement.

Moreover, the exciter base can be assumed to be rigidly attached to the floor [16]. Indeed, the shaker is fixed to the ground, which is supposed to be infinitely rigid. The mode of the shaker body, in other words the isolation mount mode, is thus located at a frequency below the frequencies that are analysed. Therefore, the parameters related to the shaker body (m_b , k_b , c_b) are estimated possible values and are defined so that the body mode is out of the frequency range of interest, meaning below the [5 Hz - 2 000 Hz] range. An identification method should be developed to determine these parameters if modes lower than 5 Hz had to be identified but the estimation used here is sufficient for this work.

As a reminder, the model of the shaker is implemented in *Simulink*. This mechanical part is shown in Figure 3.2 to better understand the equations that are used in this section.


 Figure 3.2: Mechanical model of a shaker implemented in *Simulink*.

The estimated parameters of the shaker body will be introduced in the *Simulink* model when the shaker dynamics will be simulated. However, to simplify the equations for the parameter identification process, the model shown in Figure 3.3 is used. Indeed, since the body mode is below the frequency range of interest, the mechanical system can be modelled by two degrees of freedom: the table (with its suspension stiffness k_s and damping c_s) and the coil (with its suspension stiffness k_c and damping c_c).

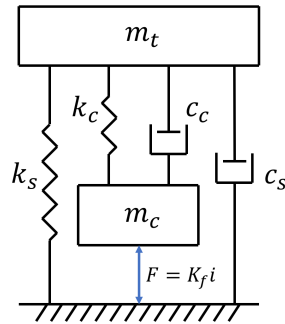


Figure 3.3: Simplified mechanical model [2].

Based on this 2-DoF model, the electromagnetic force applied on the coil may be expressed through Equation 3.1:

$$F = K_f i = m_c \ddot{x}_c + c_c (\dot{x}_c - \dot{x}_t) + k_c (x_c - x_t). \quad (3.1)$$

Similarly, the dynamics of the table may be given by Equation 3.2:

$$(m_l + m_t)\ddot{x}_t + c_s\dot{x}_t + k_s x_t = c_c(\dot{x}_c - \dot{x}_t) + k_c(x_c - x_t), \quad (3.2)$$

where m_l is the mass of the load being tested on the table of the shaker.

By using the Laplace transform and by eliminating x_c from these two last equations, the expression of the current flowing through the coil is obtained as a function of the table displacement:

$$I = \frac{m_c(m_l + m_t)s^4 + (m_c c_s + c_c M)s^3 + (m_c k_s + c_c c_s + k_c M)s^2 + (c_c k_s + k_c c_s)s + k_c k_s}{K_f(c_c s + k_c)} X_t, \quad (3.3)$$

with $M = m_c + m_t + m_l$, and where I is the Laplace transform of the current i and X_t the Laplace transform of the table displacement x_t . The acceleration-over-current FRF is then directly obtained:

$$\begin{aligned} H_{acc,i} &= \frac{s^2 X_t}{I} \\ &= \frac{K_f(c_c s + k_c)s^2}{m_c(m_l + m_t)s^4 + (m_c c_s + c_c M)s^3 + (m_c k_s + c_c c_s + k_c M)s^2 + (c_c k_s + k_c c_s)s + k_c k_s}. \end{aligned} \quad (3.4)$$

This expression can be simplified at low frequency. Indeed, at low frequency, in other words, at frequencies much smaller than the natural frequency of the coil, it can be assumed that the coil and the table move rigidly together (k_c and c_c tend to infinity). Therefore, the acceleration-over-current FRF at low frequency expresses as:

$$H_{acc,I_{LF}}(s) = \frac{K_f s^2}{(m_c + m_l + m_t)s^2 + c_s s + k_s}. \quad (3.5)$$

The resonance frequency of the electrodynamic shaker at low frequency can be expressed as follows, unloaded and with a mass-load m_l respectively:

$$f_{0_{LF}} = \frac{1}{2\pi} \sqrt{\frac{k_s}{m_t + m_c}}, \quad f_{l_{LF}} = \frac{1}{2\pi} \sqrt{\frac{k_s}{m_t + m_c + m_l}}. \quad (3.6)$$

From these two equations, the moving mass of the shaker can be evaluated:

$$\boxed{m_0 = m_t + m_c = \frac{f_{l_{LF}}^2}{f_{0_{LF}}^2 - f_{l_{LF}}^2} m_l.} \quad (3.7)$$

Then, from the expression of the resonance frequency at low frequency with no-load, the

expression of the table suspension stiffness becomes:

$$\boxed{k_s = (2\pi f_{0_{LF}})^2 m_0.} \quad (3.8)$$

Similarly, at high frequency, it means at a frequency much larger than the natural frequency of the table, the acceleration-over-current FRF can be obtained by simplifying Equation 3.4. Indeed, it may be assumed that the coil and the table move out of phase at high frequency (k_s and c_s can be set equal to 0). Therefore, the FRF becomes:

$$H_{acc, I_{HF}}(s) = \frac{K_f k_c}{m_c(m_l + m_t)s^2 + (m_l + m_t + m_c)c_c s + (m_l + m_c + m_t)k_c}. \quad (3.9)$$

The resonance frequency of the electrodynamic shaker at high frequency can be expressed as follows, unloaded and with a mass-load m_l respectively:

$$f_{0_{HF}} = \frac{1}{2\pi} \sqrt{\frac{(m_t + m_c)k_c}{m_c m_t}}, \quad f_{l_{HF}} = \frac{1}{2\pi} \sqrt{\frac{(m_l + m_t + m_c)k_c}{m_c(m_l + m_t)}}. \quad (3.10)$$

Therefore, from these two expressions, the mass of the coil may be computed:

$$\boxed{m_c = \frac{(f_{0_{HF}}^2 - f_{l_{HF}}^2)(m_l + m_0)m_0}{f_{0_{HF}}^2(m_l + m_0) - f_{l_{HF}}^2 m_0}.} \quad (3.11)$$

Since the moving mass and the mass of the coil are now known, the mass of the table is simply given by:

$$\boxed{m_t = m_0 - m_c.} \quad (3.12)$$

Moreover, the stiffness of the suspension of the coil may be expressed as:

$$\boxed{k_c = \frac{m_t m_c}{m_0} (2\pi f_{0_{HF}})^2.} \quad (3.13)$$

The remaining mechanical parameters to identify are the current/force coefficient K_f and the damping c_s and c_c .

At first, the current/force coefficient may be approximated by using the expression of the magnitude of the FRF in Equation 3.5 with no load at a frequency equal to ten times the resonance frequency $f_{0_{LF}}$ so that the shaker operates out of the influence of the two modes as it can be seen on the example in Figure 3.4.

At this frequency, the terms involving k_s and c_s are negligible and then, by isolating

the parameter K_f , it comes:

$$K_f = m_0 |H_{acc,i}(2\pi \times 10 f_{0_{LF}}, m_l = 0)|. \quad (3.14)$$

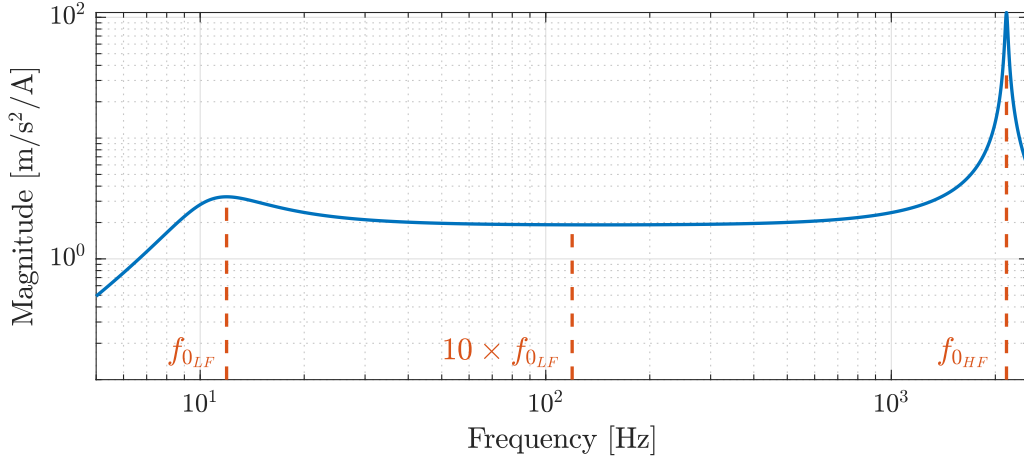


Figure 3.4: Acceleration-over-current FRF and highlight of natural frequencies.

Similarly, the damping coefficient of the table suspension may be found thanks to the magnitude of the FRF with no load at the low frequency peak of resonance ($f = f_{0_{LF}}$):

$$c_s = \frac{2\pi \times f_{0_{LF}} K_f}{|H_{acc,i}(2\pi \times f_{0_{LF}}, m_l = 0)|}. \quad (3.15)$$

Finally, the damping coefficient of the suspension of the coil is obtained thanks to the magnitude of the FRF with no load at the high frequency peak of resonance ($f = f_{0_{HF}}$):

$$c_c = \frac{K_f k_c}{2\pi f_{0_{HF}} m_0 |H_{acc,i}(2\pi \times f_{0_{HF}}, m_l = 0)|}. \quad (3.16)$$

Therefore, each mechanical parameter of the shaker model is now defined by an analytical expression.

3.1.2 Electrical parameters

Now that it is known how to compute the mechanical parameters, the electrical parameters must be identified. The resistance R and the inductance L of the shaker could be measured with an LCR-meter but it is not reliable since it does not account for the frequency dependency of the resistance value. Indeed, the resistance of the shaker depends on the frequency because of the skin effect [17]. However, the LCR-meter available at V2i company works offline, by sending a 10-kHz frequency signal [18]. This frequency

is much higher than the operating frequency range of an electrodynamic shaker so the values at the frequencies of interests cannot be measured. An automatic method to compute resistance value and inductance value is therefore needed.

As for the mechanical part of the model, the implementation in *Simulink* of the electrical part can be observed in Figure 3.5 to better understand the following computations. This is the implementation of the Equation 2.4.

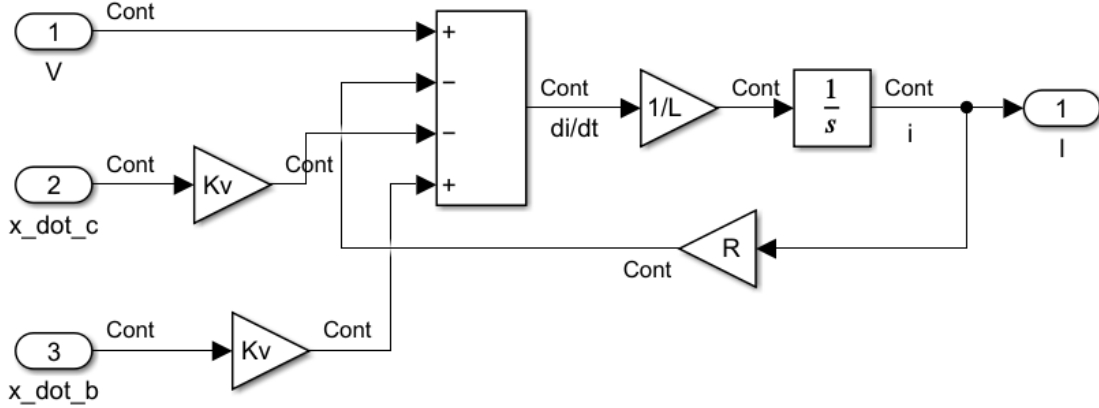


Figure 3.5: Electrical model of a shaker implemented in *Simulink*.

By using the Laplace transform in Equation 2.4, and by isolating the term V/I , the expression of the voltage-over-current FRF is obtained in Equation 3.17:

$$H_{V,I} = \frac{V}{I} = j2\pi fL + R + \frac{K_v}{2\pi f} \frac{\ddot{X}_c}{I}. \quad (3.17)$$

However, as said previously, it can be assumed that the table and the coil move in phase at low frequency. Therefore, $\frac{\ddot{X}_c}{I}$ is equal to $\frac{\ddot{X}_t}{I}$ for which the analytical expression is already known (cf. Equation 3.5) and for which all parameters are already identified.

Moreover, it can be seen in Equation 3.17 that the inductance L has a low influence at low frequency. Therefore, only the resistance R is identified by using the experimental voltage-over-current FRF around the first peak of resonance. To do so, the MATLAB function *lsqcurvefit* is used. The latter finds the parameters that allow to fit the numerical curve on the experimental one in the least squares sense.

To determine the last electrical parameter, the inductance L , an iterative method is used. A first guest is set: a value assessed in other works for a similar shaker is used ([9] and [4]). Thereafter, the electromechanical model implemented in *Simulink* is used to simulate the tension-over-current FRF. After that, an objective function is defined as

the difference between the experimental FRF and the numerical one. This is computed for many values of the inductance L and the objective function is plotted as a function of the inductance. The most suitable inductance is then the L parameter for which the objective function is minimum.

3.1.3 Experimental measurements

To identify these parameters, measurements are realised to obtain the experimental acceleration-over-current and voltage-over-current FRFs. Therefore, the current, the voltage, and the table acceleration must be measured during a sine sweep test on the shaker to identify. Since these FRFs are needed for an empty test and for a loaded test, the measurements are done twice: one with nothing on the shaker table and one with an additional known mass. In this work, it is chosen to take a mass of about 5% of the shaker mass. For the loaded test, this load is screwed onto the shaker table.

To realise a test on the shaker, several tools are needed. The first one is the acquisition software to define the input signal and to post-treat the measurements. Transducers are also needed to measure the acceleration, the current and the voltage. These are connected to an acquisition system and an amplifier is needed to strengthen the input current signal.

Since the lumped parameter model only considers the vertical translation DoFs, it is required to measure the vertical acceleration of the shaker table. To do so, a *PCB* or a *Dytran* accelerometer is glued at the centre of the table. Thereafter, some amplifiers give the amplified current as an output so this signal can directly be used for the identification. However, it is not always the case so another possibility is to use a current-clamp. It is placed around the wires feeding the coil and is connected to the acquisition system. Finally, the voltage signal is needed. As for the current, some amplifiers have a voltage output that directly gives the amplified output. Nevertheless, if the output voltage is too high to be measured, only the input voltage of the amplifier may be obtained. In this case, to get the amplified signal, it only needs to be multiplied by the amplifier gain.

Finally, to obtain the needed FRFs for the identification, the Fast Fourier Transform (FFT) of each time signal (acceleration, voltage and current) is computed. The FRFs are then computed by dividing the acceleration FFT by the current FFT and by dividing the voltage FFT by the current FFT. Therefore, the acceleration-over-current and voltage-over-current FRFs are obtained for the empty and the loaded tests. The natural frequencies are then identified and the mechanical parameters are computed. After that, thanks to the measurements of the current and of the voltage, the experimental voltage-

over-current FRF is computed. The electrical parameters are finally computed. These instructions are summarised in Figure 3.6.

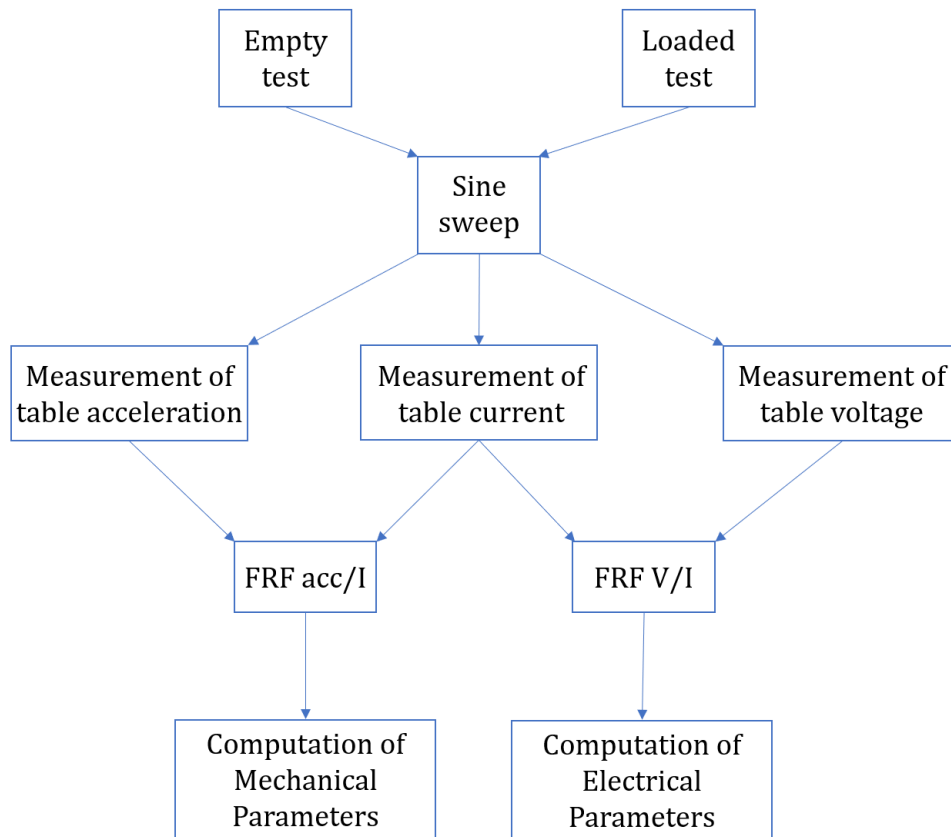


Figure 3.6: Identification process of the model parameters.

3.1.4 Introduction of the parameters in the numerical model

The parameter values are now introduced in the numerical model. The shape of the input signal, i.e., the voltage signal, is given to the *Simulink* program so that the outputs of interest can be simulated: the voltage at the terminals of the coil, the current flowing through the shaker as well as the acceleration of the table of the shaker may be predicted. This constitutes the main block of the virtual shaker testing, the electrodynamic shaker is numerically modelled. Dangerous phenomena could be detected thanks to these simulations.

However, before trusting the obtained results, the identification method has to be validated. To do so, the simulated transfer functions can be computed and can be compared with the experimental ones.

3.2 Validation of the shaker model

In order to validate the method developed, experimental tests are performed then compared to the simulated results obtained with the electromechanical shaker model. The aim of this work is to optimise a virtual shaker testing but, for V2I company, the main interest of this internship is the model of a large 120-kN shaker installed in their lab. However, this shaker is scarcely available. Testing campaigns for clients are obviously prioritised and therefore, the shaker was not often available for this work. The identification method has thus to be established before the large shaker could be accessed. Therefore, the process was first studied on a smaller 100-lbf shaker that is always at hand.

The small shaker is easy to manipulate and has more or less the same dynamics as the 120-kN shaker. Indeed, their peaks of resonance appear in the same frequency range. The identification method first applied on the 100-lbf shaker (i.e., 445 N) is then extended to the larger shaker.

3.2.1 Preliminary tests: 100-lbf shaker

In a first time, the VTS VG-100 shaker is used. It is shown in Figure 3.8. This electrodynamic shaker is guided vertically so transverse effects are avoided and the acceleration along the vertical axis can be measured properly. The aim of this section is then to determine the parameters of the numerical model accurately.

As it has been explained in Section 3.1, the lumped parameters are determined by calibrating numerical FRFs on experimental ones. The first step in the identification process is therefore to obtain experimentally different frequency response functions: the acceleration-over-current FRF and the voltage-over-current FRF of the shaker.

To evaluate these FRFs, open loop sine sweep tests are conducted: a sine signal of constant voltage amplitude is imposed at coil terminals and its frequency varies linearly between 5 Hz and 3 000 Hz. The acquisition is made by using *The Lab* acquisition system (cf. Figure 3.7), and the *The V2i Acquisitor* software, developed by the company.



Figure 3.7: *The Lab* acquisition system.

The considered acquisition parameters are gathered in Table 3.1.

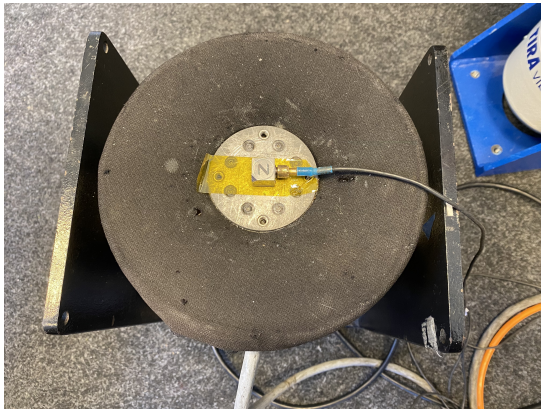
Parameters	Value
Input type	Sine sweep
Input voltage	0.2 V
Sweep velocity	30 Hz/s
Acquisition time	100 s
Ramp duration	0.2 s
Bandwidth	20 000 Hz
Sample frequency	51 200 Hz

Table 3.1: Acquisition parameters of the tests performed on the VTS VG-100 shaker.

One can note that the 20 000 Hz bandwidth is really high compared to the maximum 3 000 Hz sine sweep frequency. This is due to the fact that, by default in the *V2i Acquisitor*, the sample frequency is fixed to 51 200 Hz. And in order to respect the Nyquist-Shannon sampling theorem, the bandwidth is limited to the sampling frequency divided by 2.56 [19], which gives 20 000 Hz. This value is kept for this test to ensure having a good time resolution if the time signals should be analysed. The Nyquist-Shannon sampling theorem is therefore largely satisfied.

The aim of the amplifier is to amplify the current signal in order to get the defined voltage signal. The amplitude of this signal is multiplied by the value of the gain. However, the voltage signal does not need to be amplified in this case so the gain is set such that the input voltage is equal to the output. This output voltage is then applied to the shaker. The value of the amplitude of the signal has thus been determined such that the shaker does not undergo too large accelerations.

As it is required by the method presented in Section 3.1 and as it can be seen in Figure 3.8, the vibration test is done twice: with no mass and with a load of 409 g.



(a) Unloaded test.



(b) Test with a mass of 409 g.

Figure 3.8: Sine sweep test in open loop on the VTS VG-100 shaker.

Since the acceleration-over-current and voltage-over-current FRFs are needed for the parameter identification, several measurements must be recorded. First, the acquisition system records the current entering in the shaker thanks to the current output of the amplifier. Moreover, the voltage signal before and after being multiplied by the amplifier are measured. The acceleration of the table has to be measured too. Therefore, for the unloaded test, an accelerometer is placed on the table of the shaker (Figure 3.8a), and for the loaded test, an accelerometer is placed on the top of the mass (Figure 3.8b). In order to understand how the coil moves with respect to the table, an accelerometer is placed nearest to the coil. The coil is not directly accessible so it is placed below the table as it can be observed in Figure 3.9.



Figure 3.9: Accelerometer placed near the coil of the VTS VG-100 shaker.

The experimental acceleration-over-current FRFs are then plotted for the empty test and the test with the 409 g mass in Figure. 3.10.

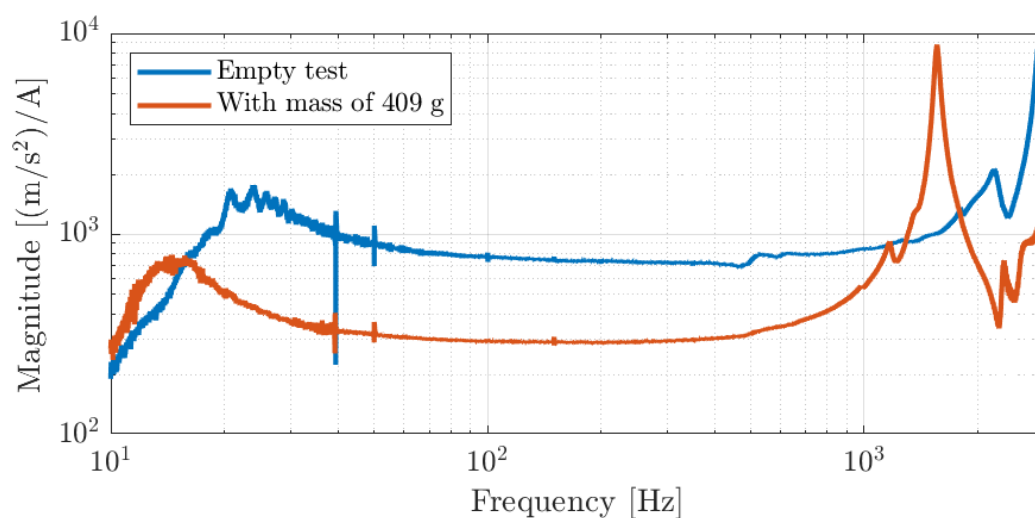


Figure 3.10: Experimental acceleration-over-current frequency response functions. Measurements done on the VG-100 shaker with a sine sweep in the [5 Hz - 3 000 Hz] frequency range.

To identify the natural frequencies of the shaker, the Least-Squares Complex Exponential method (LSCE) is used [20]. They are gathered in Table 3.2. As expected, the addition of a mass on the table decreases the natural frequencies since they are inversely proportional to the square root of the loaded mass (cf. Equation 3.6 and 3.10).

	Low frequency [Hz]	High frequency [Hz]
Empty test	23.8	2 910.2
Test with mass (409 g)	14.63	1 563.01

Table 3.2: Resonance frequencies of the VG-100 shaker for two tests: empty test and test with a mass of 409 g.

Thanks to these values, the mechanical parameters of the numerical shaker model are evaluated with the method described in Section 3.1.1. These are presented in Table 3.3.

Parameters	Value
Table suspension stiffness k_s	5 332 N/m
Coil bounding stiffness k_c	12.8×10^6 N/m
Table suspension damping coefficient c_s	14.68 N.s/m
Coil damping coefficient c_c	58.93 N.s/m
Table mass m_s	48.6 g
Coil mass m_c	189.3 g
Current-force coefficient K_f	173.9 N/A

Table 3.3: Mechanical parameters of the VTS VG-100 shaker.

As said in Section 3.1.2, the electrical parameters are computed based on the voltage-over-current measured FRFs. Thanks to these data, the electrical parameters are computed and are shown in Table 3.4.

Parameters	Value
Resistance R	20.8Ω
Inductance L	$2.4 \mu\text{H}$

Table 3.4: Electrical parameters of the VTS VG-100 shaker.

Now that all the parameters of the numerical model are known, they are introduced in the model. *Simulink* returns then the accelerations, the voltage and the current as a function of time and the FRFs of interest may be reconstructed. To compare the simulated and experimental curves, the acceleration-over current FRFs are superposed in Figure 3.11 and the acceleration-over-voltage, in Figure.3.12. Two modes are identified for each test since there are two resonance peaks in the [5 Hz - 3 000 Hz] frequency range.

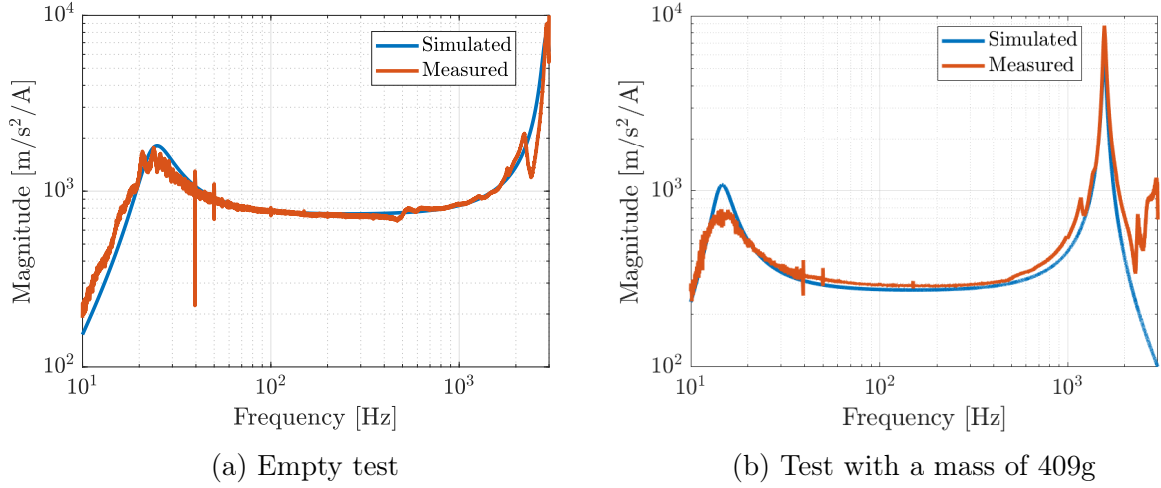


Figure 3.11: Comparison of the simulated and experimental acceleration-over-current FRFs for a sine sweep in the [5 Hz - 3 000 Hz] frequency range on the 100-lbf shaker.

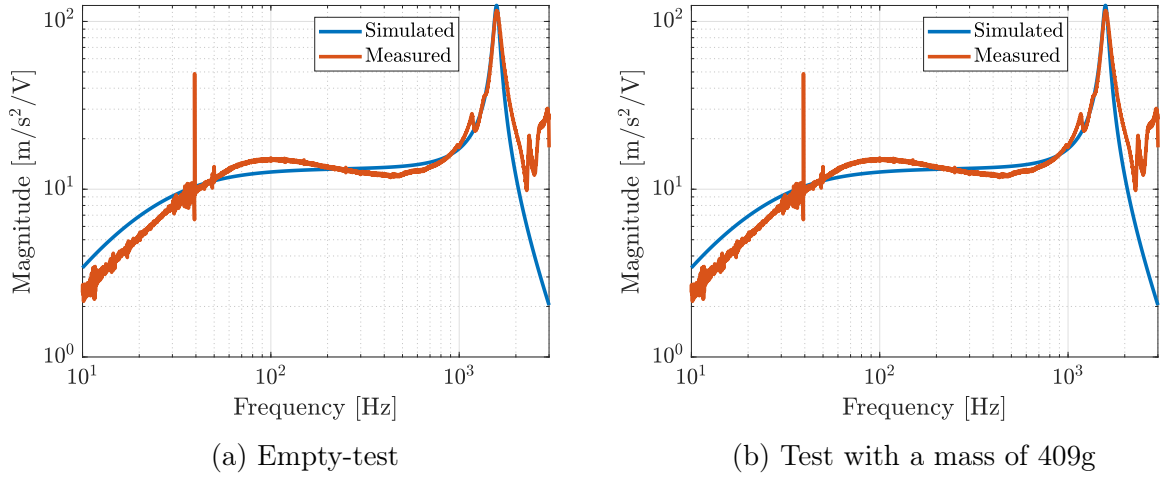


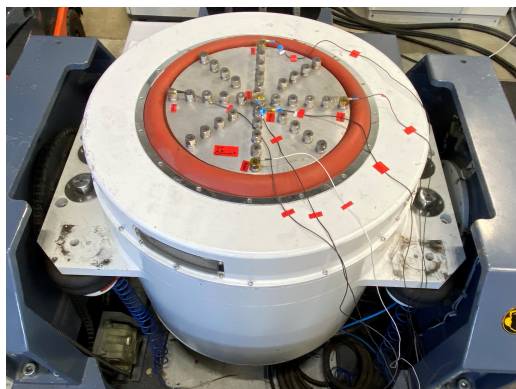
Figure 3.12: Comparison of the simulated and experimental acceleration-over-voltage FRFs for a sine sweep in the [5 Hz - 3 000 Hz] frequency range on the 100-lbf shaker.

To conclude, it can be said that the method developed in Section 3.1 allows to represent the dynamics of the shaker to introduce in the VST. This method developed to identify the numerical parameters is thus validated. In the following, the same methodology is applied on a larger shaker, certainly more complex.

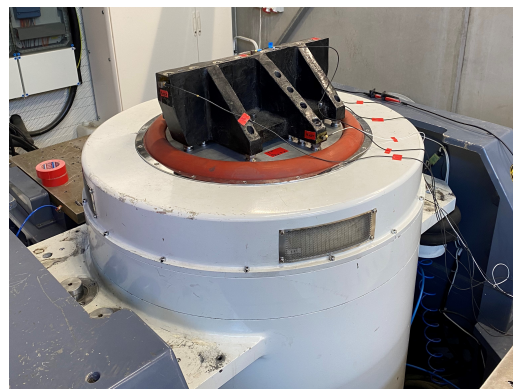
3.2.2 More advanced tests: 120-kN shaker

Now, this method is applied to the larger shaker which has a more complex structure: the DonLing shaker with a 120-kN force. As for the VG-100 shaker, the parameters of the numerical model are identified, then the model is used to simulate the shaker dynamics. Thereafter, the simulated results are compared to the experimental ones.

As described in Section 3.1, two tests have to be conducted: an unloaded test and one with a mass. The chosen load has a mass of 33.1 kg. This mass is picked because of its high stiffness and there is more or less the same proportion between the tested mass and the shaker mass than for the preliminary test on the 100-lbf shaker. Indeed, the 33-kg mass is about 5% of the shaker mass. Several accelerometers are placed on the shaker table (cf. Figure 3.13a) and on the mass (cf. Figure 3.13b) for the loaded test. The sensors are placed in a cross pattern to be able to catch torsion or tilting modes. Since the parameters of the shaker are identified by measuring the vertical acceleration of the table, it is implicitly considered that the table is infinitely rigid. The aim of measuring the acceleration off-centre is to assess the validity of this assumption. If the acceleration is not the same everywhere, it is not verified.



(a) Unloaded test.



(b) Test with a mass of 33 kg.

Figure 3.13: Sine sweep test in open loop on the 120-kN DongLing shaker.

In order to use the method presented in Section 3.1, it is again needed to register the current that feeds the coil of the shaker and the voltage imposed at its terminals in addition to the acceleration at the centre of the table. The amplifier used with this kind of shaker does not have any current output or voltage output. Therefore, to record the current, a current-clamp is placed on the wires feeding the coil as shown in Figure 3.14.

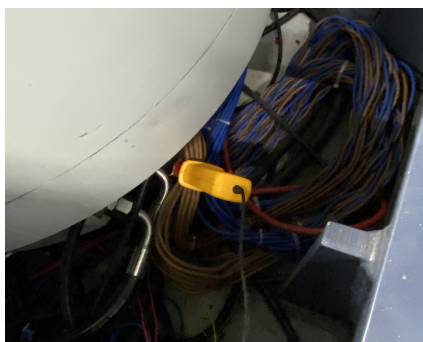


Figure 3.14: Measurement of the current signal with a current-clamp.

The voltage directly applied at the terminals of the coil being not available, only the non-amplified voltage is recorded. This voltage is directly known since this signal is imposed. However, in the method of identification developed in Section 3.1, it is the voltage after amplification that appears in the equations. This voltage is denoted V_{out} and the drive signal (unamplified voltage) is denoted V_{in} . These two voltages are linked by the gain. Therefore, the output voltage V_{out} is replaced by the following expression in the equations of the identification method:

$$V_{out} = \text{gain} \times V_{in}. \quad (3.18)$$

This gain is introduced in the model as it is shown in Figure 3.1 between V_{in} and V_{out} .

When a test is launched on the shaker, an amplifier parameter between 0 and 100% must be chosen. It needs to be identified and it adds an unknown parameter in the identification process. It is determined in the same manner as the resistance parameter: with a curve fitting function of MATLAB.

To obtain experimental acceleration-over-current and voltage-over-current FRFs for the parameter identification, the test campaign is realised in open loop, with no control on the acceleration at a given point of the table for example. However, open loop tests may be dangerous since there is no security on the maximum acceleration that the shaker will undergo. There is a list of shaker limitations that have to not be exceeded. These are shown in the Appendix A and concern the acceleration of the table, its stroke, the load, the torque, the force, etc. Therefore, a first set of preliminary tests are realised in order to determine the not-to-exceed maximum voltage.

As a result, this maximum voltage depends on the value of the amplifier constant. Therefore, for each amplifier value, a maximum allowable voltage amplitude has to be defined. To do so, a first controlled-acceleration test is realised in closed loop. An acceleration of 1 g is imposed at the centre of the table. The voltage-over-acceleration FRF is then obtained and is shown in Figure 3.15. The value at the peak of coil resonance gives the voltage value that will produce an acceleration of 1 g at the centre of the table in open loop test. This voltage value is first used as the voltage amplitude in the open loop test.

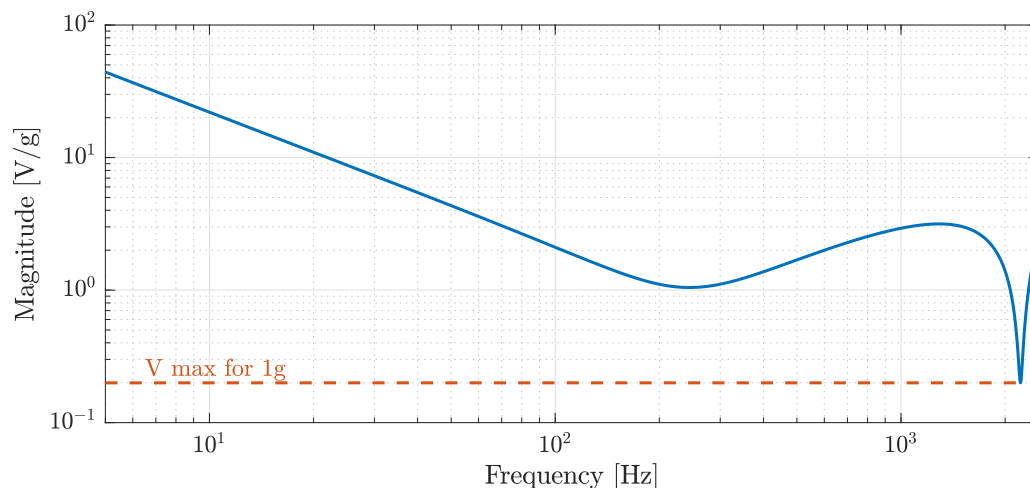


Figure 3.15: Frequency response function of voltage at the terminals of the coil over the acceleration at the centre of the coil of the shaker of a closed loop test.

The open loop tests can be performed safely in this way. The acquisition is made using the *Siemens LMS testLab* software. The *V2i Acquisitor* is not used anymore because no control system is implemented in this software. The considered acquisition parameters are gathered in Table 3.5. The frequency of the signal varies between 5 Hz and 2 500 Hz in a logarithmic way. A logarithmic sweep frequency variation is chosen only because for such tests with a sufficient resolution, a linear sweep would have need a too long time. The availability of this shaker being very limited for tests, a logarithmic sine sweep is preferred.

Parameters	Value
Input type	Sine sweep
Input voltage	between 0.008 V and 0.15 V
Sweep velocity	1 oct/min
Bandwidth	20 000 Hz
Frequency sample	51 200 Hz
Acquisition time	548 s

Table 3.5: Acquisition parameters of the tests on the 120-kN DongLing shaker.

It is important to note that the amplifier could act non-linearly. It is therefore needed to verify before analysing the results that the acceleration increases linearly when the gain is raised. To verify this, the acceleration-over-voltage FRF is measured for different amplifier values. The linearity of the amplifier is then verified by looking at the FRFs evaluated at 100 Hz for the different amplifier constant.

In a first time, the results of the empty-test are used. The values measured on the FRFs at 100 Hz (cf. Figure 3.16a) have been reported in Figure 3.16b which plots these

values as a function of the amplifier parameter. It can be seen on this graph that the line is straight. This means that the amplifier acts linearly.

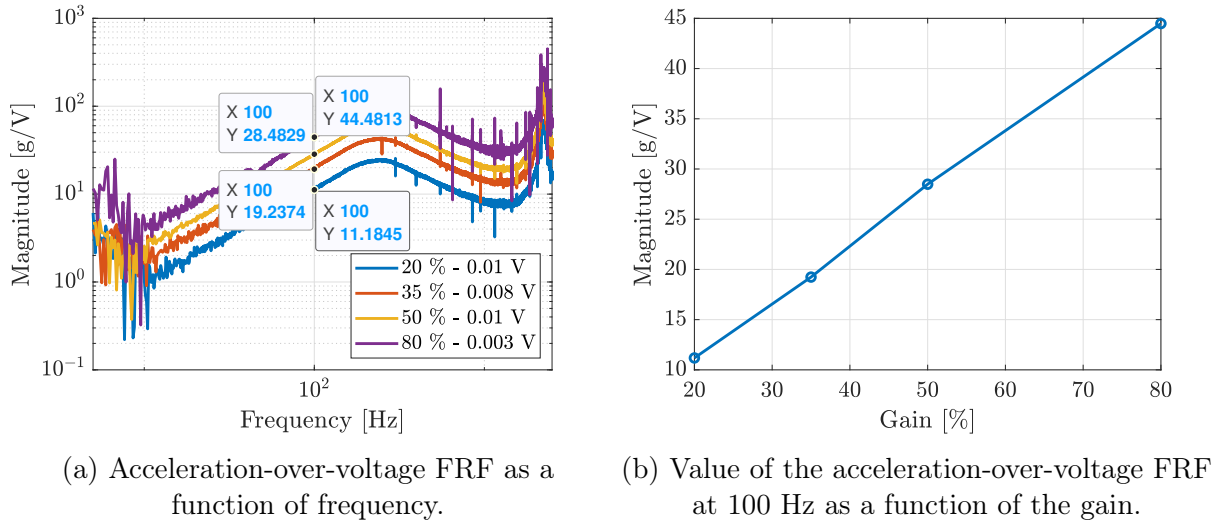


Figure 3.16: Study of the linearity of the amplifier. Measurements done on the 120-kN shaker with no load.

The same study is realised with the 33-kg mass-load. It can be observed in Figure 3.17 that the same conclusions are made as for the empty test.

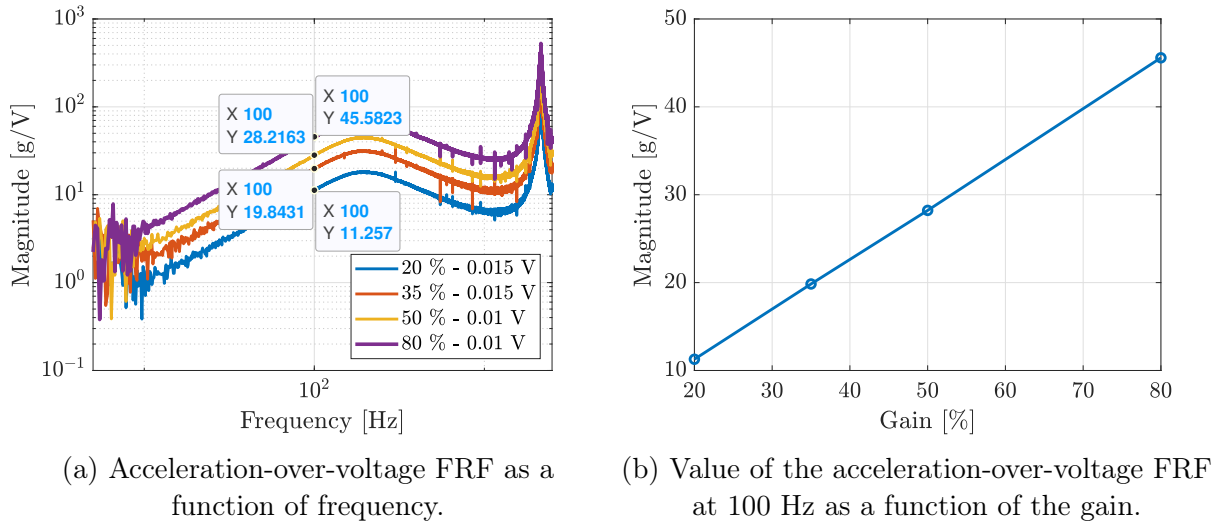


Figure 3.17: Study of the linearity of the amplifier. Measurements done on the 120-kN shaker with the mass of 33 kg.

It is also important to check that the amplifier does not distort the signal. To do so, the time-frequency plot of the current signal is plotted. This graph is called the waterfall plot and is shown in Figure 3.18. To draw it for the current signal, a Fast Fourier Transform is applied on the time-signal of the current then the frequencies and amplitudes of its component simplex waves are separated. They are finally displayed with

a level of amplitude (cold colour for low amplitude and warm colour for high amplitude) for different values of frequency with respect to time. This allows then to identify the dominant harmonics. It can be seen in Figure 3.18 that there is one dominant harmonic. A second harmonic, less obvious, is detected. However, it is negligible in comparison with the first harmonic. Therefore, it can be considered that the amplifier acts linearly and does not distort the signal.

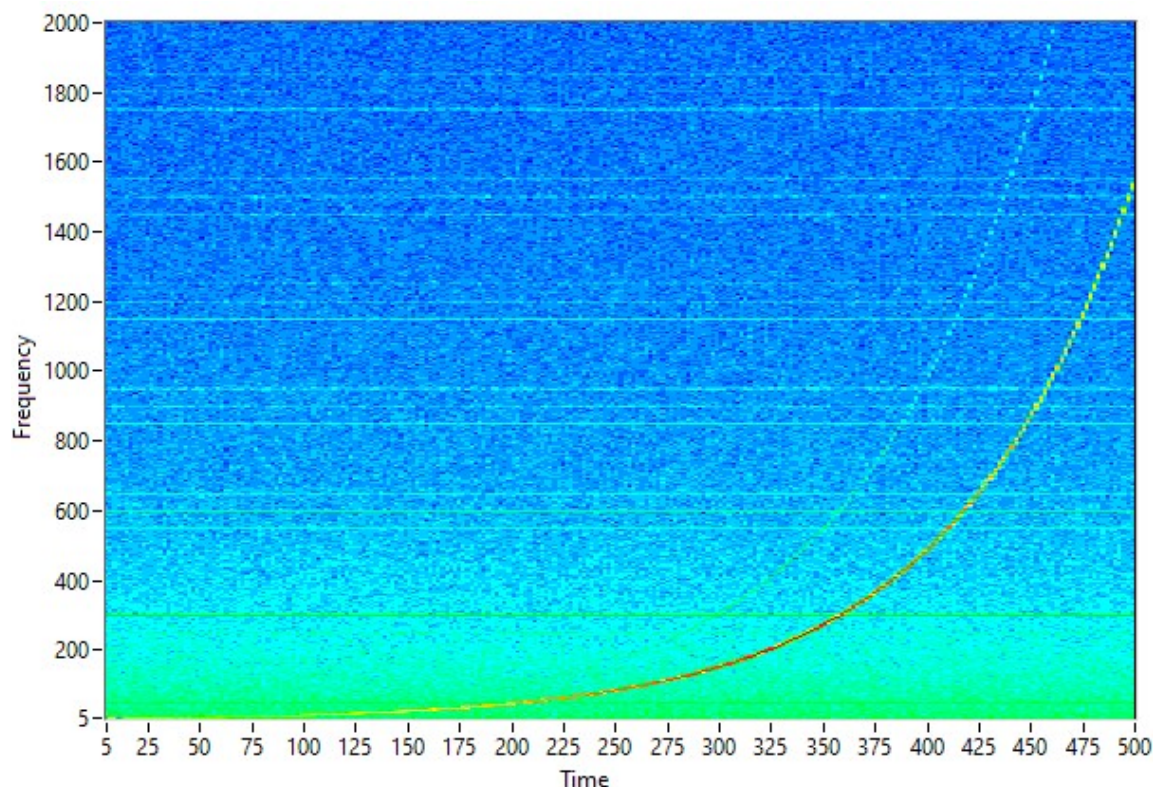


Figure 3.18: Waterfall plot of the current in the coil of the 120-kN shaker.

It can be seen in Figure 3.16 and 3.17 that these measurements are very noisy. It is because the level of the drive signal is too low and so the measured signal is too weak with respect to the noise. It results in noisy measurements, what makes more difficult the identification. However, one can see in Figure 3.15 that the peak of anti-resonance appears at high frequencies. It means thus that the limit defined by the closed loop test is necessary at high frequency but not at low frequency. Therefore, the drive signal can have a larger amplitude at low frequency and a lower one at high frequency. The input voltage is then defined at 0.15 V up to 100 Hz and after that frequency, is set at 0.5 V.

All the measurements needed for the identification process are achieved. The methodology explained in Section 3.1 can now be applied on these data. The parameters of the model can then be determined and the FRFs may be simulated.

The first step of the process is to determine the experimental resonance frequencies of the shaker. In that perspective, the acceleration-over-current FRFs are plotted in Figure 3.19.

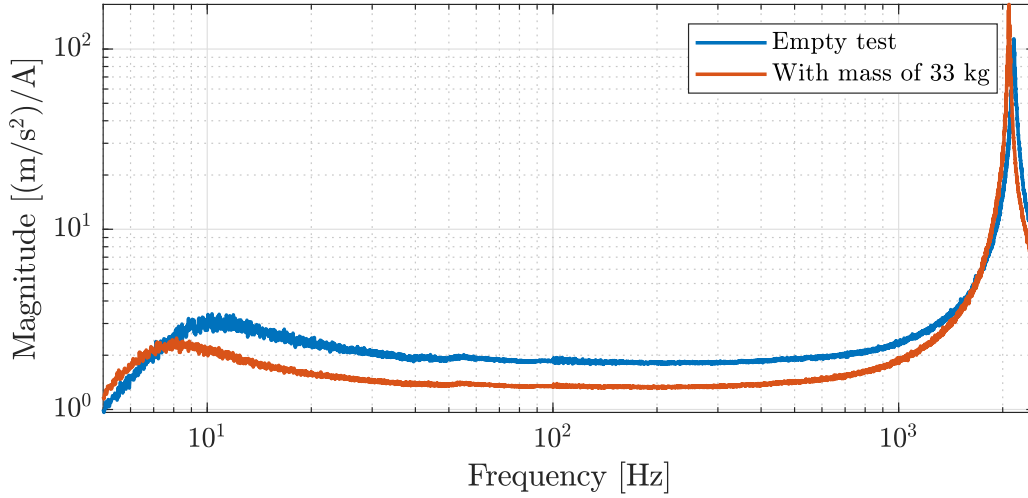


Figure 3.19: Experimental acceleration-over-current frequency response functions. Measurements done on the 120-kN DongLing shaker with a sine sweep in the [5 Hz - 2 500 Hz] frequency range.

The resonance frequencies are then identified and their values are gathered in Table 3.6.

	Low frequency [Hz]	High frequency [Hz]
Empty test	10.73	2 154.3
Test with mass (33 kg)	8.24	2 085.5

Table 3.6: Resonance frequencies of the 120-kN DongLing shaker for two tests: empty test and test with a mass of 33 kg.

Thanks to these values, the mechanical parameters of the shaker are evaluated with the method described in Section 3.1.1. These are presented in Table 3.7.

Parameter	Value
Table suspension stiffness k_s	328 920 N/m
Coil bounding stiffness k_c	1952×10^6 N/m
Table suspension damping coefficient c_s	2 965.7 N.s/m
Coil damping coefficient c_c	2 397.9 N.s/m
Table mass m_s	59 kg
Coil mass m_c	13 kg
Current-force coefficient K_f	136.46 N/A

Table 3.7: Mechanical parameters of the 120-kN shaker.

After that, the electrical parameters are computed based on the voltage-over-current measured FRFs. These are plotted in Figure 3.20.

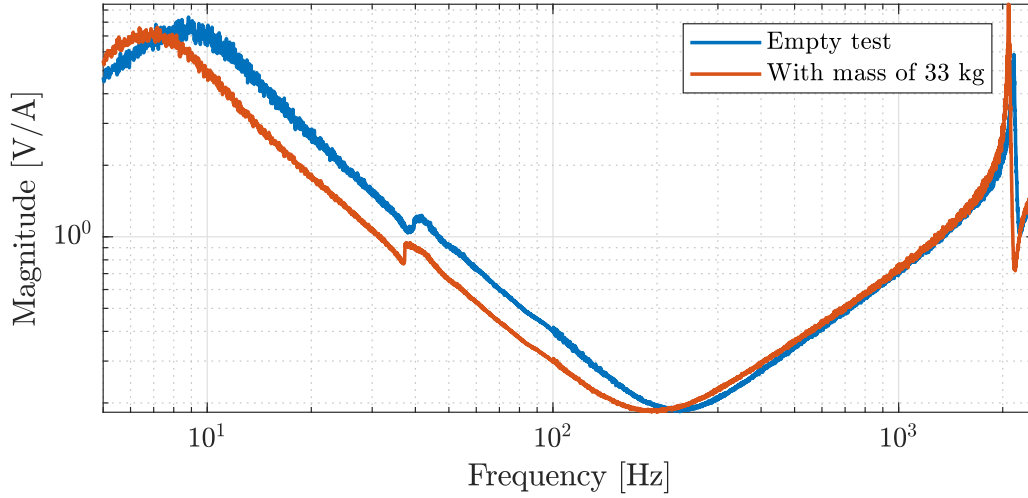


Figure 3.20: Experimental voltage-over-current frequency response function. Measurements done on the 120-kN DongLing shaker with a sine sweep the [5 Hz - 2 500 Hz] frequency range.

Thanks to these data, the electrical parameters are computed and are shown in Table 3.8.

Parameter	Value
Resistance R	$0.2003 \, \Omega$
Inductance L	$10.68 \, \mu\text{H}$
Voltage-velocity coefficient K_v	$136.46 \, \text{V}/(\text{m/s})$
Gain g	23.9

Table 3.8: Electrical parameters of the 120-kN DongLing shaker.

It can be noticed that the value of the resistance is quite small. This result was expected because the resistance increases with the frequency as a consequence of the skin effect [17]. However, as it has been said previously, the resistance value is identified thanks to the voltage-over-current at low frequency. This is why this value is so small.

All the mechanical and electrical parameters being known, the FRFs may be synthesised. They can be compared to the experimental ones in order to validate the model. The different curves are so superposed in Figure 3.21 for the acceleration-over-current FRFs and in Figure 3.22 for the acceleration-over-voltage FRFs.

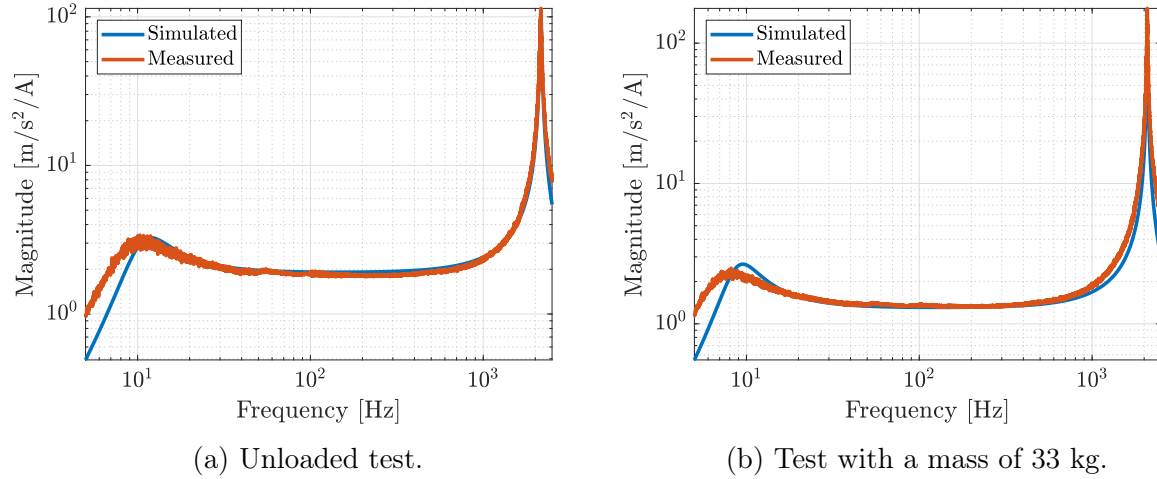


Figure 3.21: Comparison of the simulated and experimental acceleration-over-current frequency response functions. Measurements done on the 120-kN DongLing shaker with a sine sweep [5 Hz - 2 500 Hz].

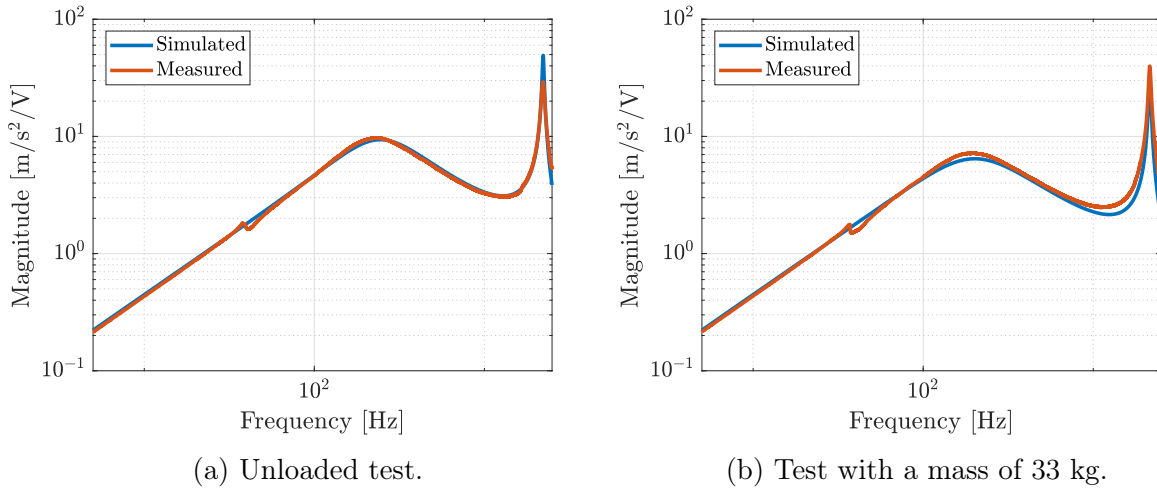


Figure 3.22: Comparison of the simulated and experimental acceleration-over-voltage frequency response functions. Measurements done on the 120-kN DongLing shaker with a sine sweep [5 Hz - 2 500 Hz].

It can be seen that these curves are well superposed. The shaker model allows then to correctly represent the dynamics of the shaker.

Analysis of the results

It is important for the user of the virtual shaker testing to know the range of frequency in which it is the most reliable and where it is less. The most important curve and the most used in the industry is the acceleration-over-voltage FRF so the error between the simulated and the experimental curves is computed. For each curve, the frequency range has been divided in three different zones and the error has been computed for each of

them. The normalised root mean square deviation (NRMSD) has been used:

$$RMSD = \sqrt{\frac{\sum_{t=1}^T (\hat{y}_t - y_t)^2}{T}}, \quad (3.19)$$

$$NRMSD = \frac{RMSD}{\bar{y}}, \quad (3.20)$$

where T is the number of considered points, \hat{y}_t the simulated point, y_t the experimental point and \bar{y} the arithmetic average of the considered experimental points.

The results of these computations may be visualised in Figure 3.23. It can be observed that the simulation is well approximated at low frequency since the error is below 3% but is not so good at high frequency since the error rises up to 30%. This can be explained by the fact that the amplitudes of the peaks at high frequency are much larger than the ones at low frequency. So, it is expected that the error is larger at high frequencies. However, it is unusual to vibrate at frequencies higher than 2 000 Hz. Only the accuracy at lower frequencies matters. Moreover, what is important to identify is not so much the peaks amplitude but rather the frequency at which they appear and these are correctly identified.

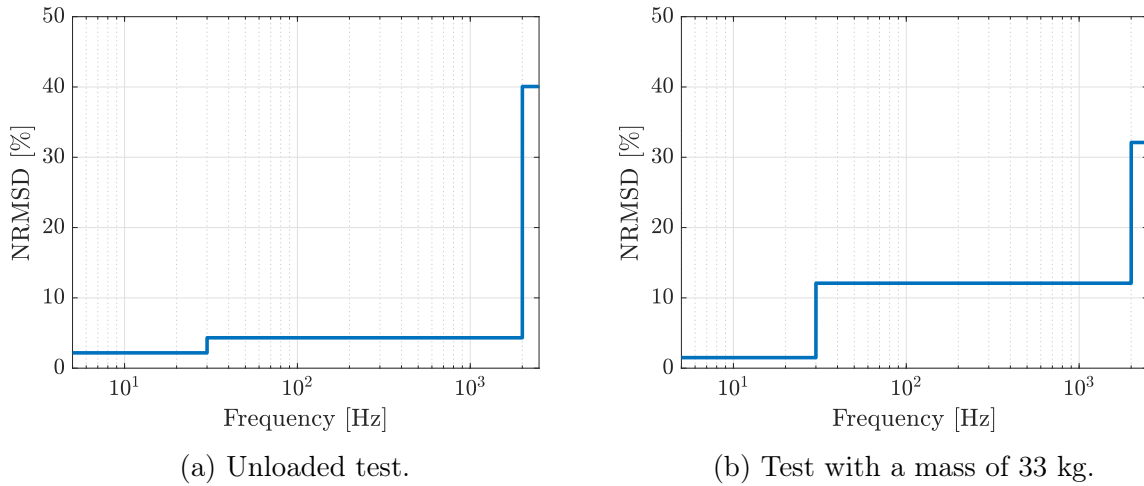


Figure 3.23: Normalised root-mean-square deviation between the simulated and experimental acceleration-over-voltage frequency response functions. Measurements done on the 120-kN DongLing shaker with a sine sweep in the [5 Hz - 2 500 Hz] frequency range.

Dynamics of the shaker

At this time, results of the test campaigns have been analysed only in the frequency domain. It is really interesting to analyse them in the time domain in order to understand the dynamics of the shaker. Indeed, the modes of the shaker can be visualised and the

possible transverse motions may be observed.

For the identification process, only the accelerometer at the centre of the shaker table is used. But in fact, as it is shown in Figure 3.13a, six accelerometers are fixed. Their space distribution and their name can be observed in Figure 3.24. The acceleration they have measured can now be analysed by looking at the time signals.

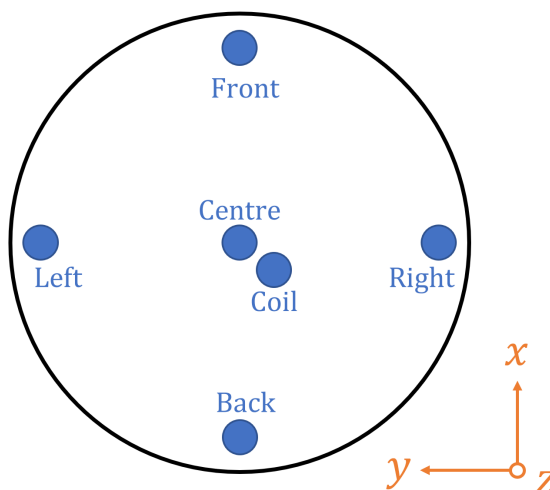


Figure 3.24: Location pattern and nomination of the accelerometers.

In this chapter, the focus will be on the results in the time domain deformed shapes. The time signals will be analysed and they will allow to visualise the operational deforms. The identified modes in the frequency domain in the previous sections may then be better understood.

Now, the measured acceleration signals may be analysed in the time domain. To do so, a link must be established between the time and the frequency domains. It can be remembered that the test campaign had been made with a logarithmic sine sweep excitation and that, as said in Table 3.5, the acquisition took 548 s. In this time, the frequency evolves from 5 Hz to 2 500 Hz. To draw a comparison between the two domains, it is then interesting to know the sweep frequency at each time of the acquisition. This can be known by looking at Figure 3.25.

In Figure 3.26, the accelerations along z -axis of all of the six sensors are superposed. One can directly notice that a first peak is identified at the 535th second. This corresponds to the sweep frequency of 2 150 Hz, which is the coil mode that had been determined in Table 3.6.

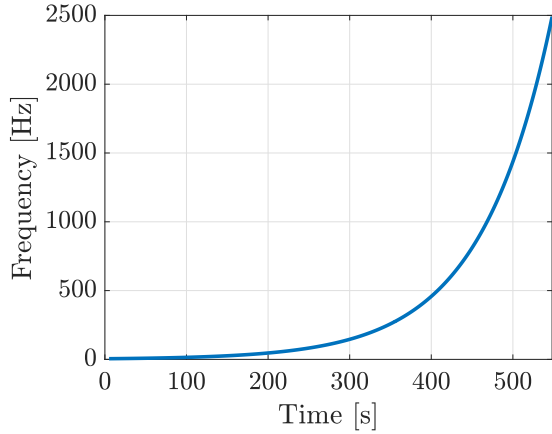


Figure 3.25: Evolution of the sweep frequency with respect to the acquisition time.

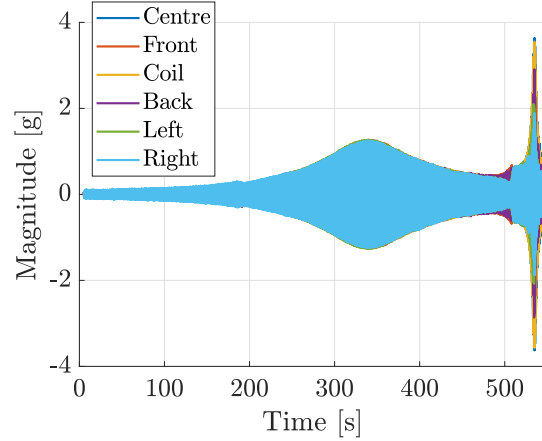
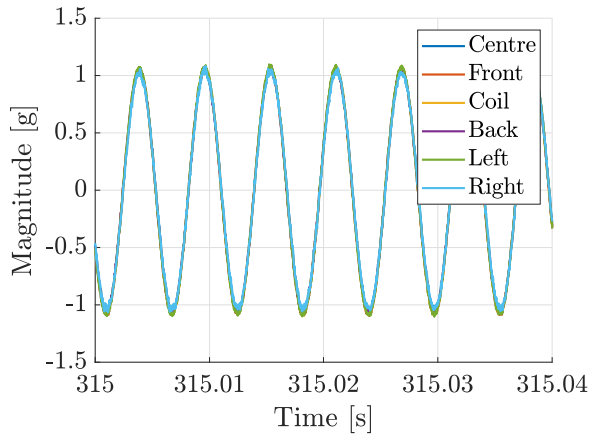
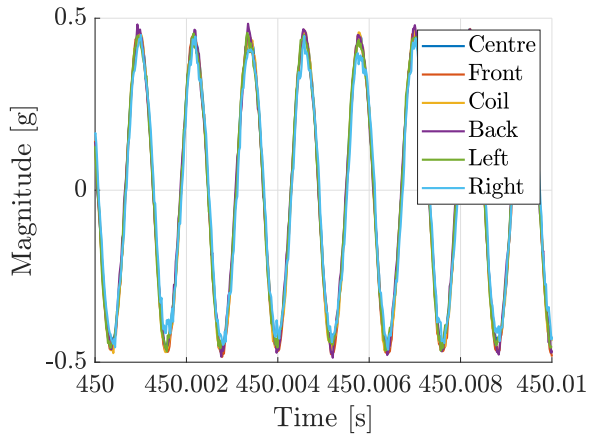


Figure 3.26: Acceleration along the vertical axis for the six accelerometers on the table of the shaker.

At first, the acceleration of these accelerometers can be observed in regions outside the peak region. For example, the acceleration around 315 s and 450 s may be observed respectively in Figure 3.27a and 3.27b. It can be seen that all the accelerometers move in phase with more or less the same amplitude of acceleration. It means so that outside the peak region, the table acts as a rigid body.



(a) Zoom around 315 s.



(b) Zoom around 450 s.

Figure 3.27: Acceleration along the vertical axis for the six accelerometers on the table of the shaker.

However, in the peak region, it is not the case. In fact, it can be seen in Figure 3.26 that the accelerometer placed at the centre is the one that withstand the highest vertical acceleration. This can be observed by animating the deformation related to this peak: the maximum amplitude of the accelerometer at the centre of the table are used as well as all the nearest maxima of the other accelerometers and their phase shifts with respect to the maximum of the centre accelerometer. The mode is then animated by plotting

this for each accelerometer. The amplitude of acceleration is given at any time by the equation 3.21:

$$a(t) = A \sin(2\pi f(t + \Delta t)). \quad (3.21)$$

The shape of this mode may be observed in Figure 3.28. It can be seen that, indeed, the accelerometer at the centre of the table is displaced more than the others along the vertical axis. However, there is also a torsion motion. Indeed, the accelerometers placed out of the centre have an acceleration along x and y axes.

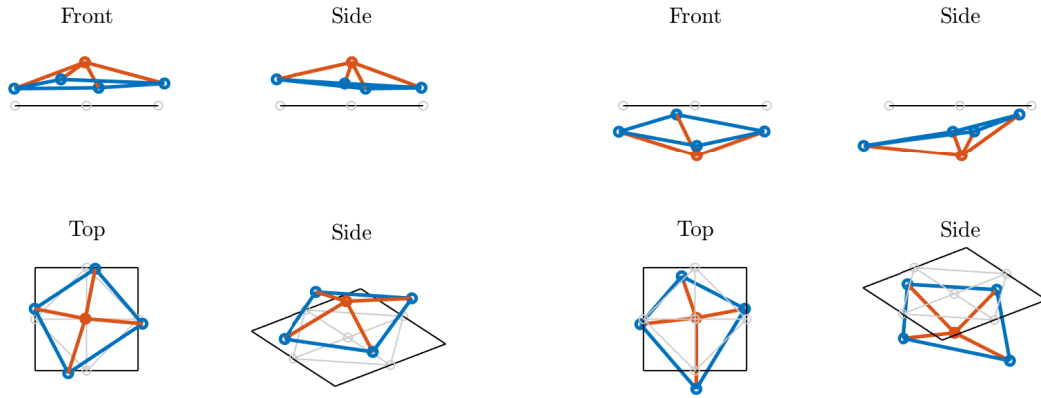


Figure 3.28: Animation of the mode at 2 145 Hz - coil mode

It can be noticed that the table of the shaker is rather largely deformed while it had been assumed infinitely stiff. Indeed, the identification of the modes have been done only with the acceleration measured at the centre of the table, as if it was the same all over the table. It clearly appears here that it is not true. This is a limitation of the model. Moreover, a torsion of the table is observed and this is not neither considered in the model. Adding other degrees of freedom in the model could be a way of improving the model.

However, in Figure 3.29 showing the acceleration along the three directions measured by the accelerometer at the centre of the table, it can be seen that the transverse accelerations are much smaller than the acceleration along the vertical z -axis. The mode shown here above at 535 s is clearly identified in the Z -direction but is much less important in the transverse directions.

The acceleration on one side of the table (at the accelerometer called *Front* in Figure 3.24) is observed in Figure 3.30 and another peak appears at 510 s. This time corresponds to a frequency of 1611 Hz. This peak was not identified in the FRFs presented in Section 3.2.2 (cf. Figure 3.19) since they were plotted with the vertical acceleration at

the centre of the table.

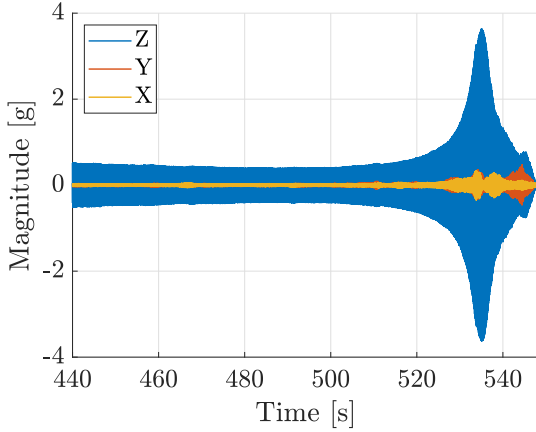


Figure 3.29: Acceleration in the three directions at the centre of the shaker table.

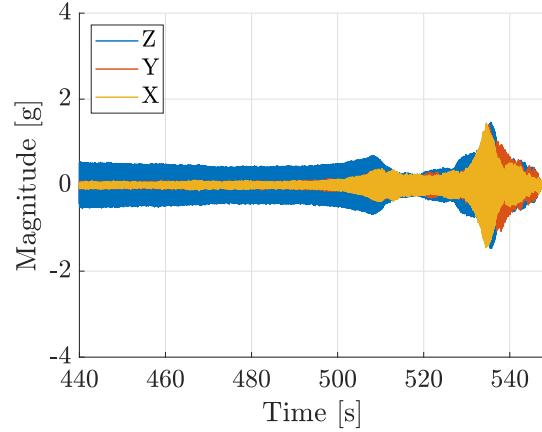


Figure 3.30: Acceleration in the three directions at the front of the shaker table.

As it has been done for the mode identified at 2 145 Hz, the mode at 1 611 Hz may be visualised in Figure 3.31. This time, the accelerometers out of the centre undergo higher vibrations than the centre of the table. It is called butterfly mode because of its shape.

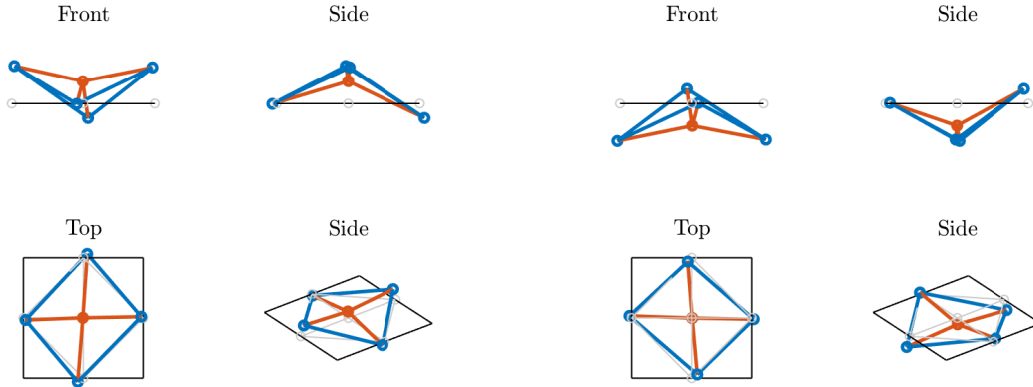


Figure 3.31: Animation of the mode at 1 611 Hz - butterfly mode

Another interesting result may be analysed. One can have noted that a phenomenon appears on the measured acceleration-over-voltage (cf. Figure 3.22) and voltage-over-current FRFs (cf. Figure 3.20) at 39 Hz and does not appear in the simulated results. The time signal of the current and of the voltage may be observed respectively in Figures 3.32 and 3.33.

The amplitude of the voltage is constant as expected. However, the time signal of the current has a distortion around 191 s which corresponds to the 39 Hz frequency. The same bump can be observed in the time signal of the accelerations in Figure 3.26 in the vicinity

of 191 s too. This phenomenon cannot be observed on the acceleration-over-current FRF since it appears on both signals; they compensate each other.

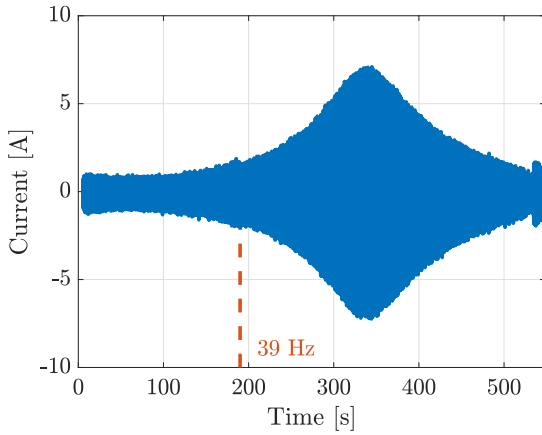


Figure 3.32: Time signal of the current flowing through the coil for the empty test.

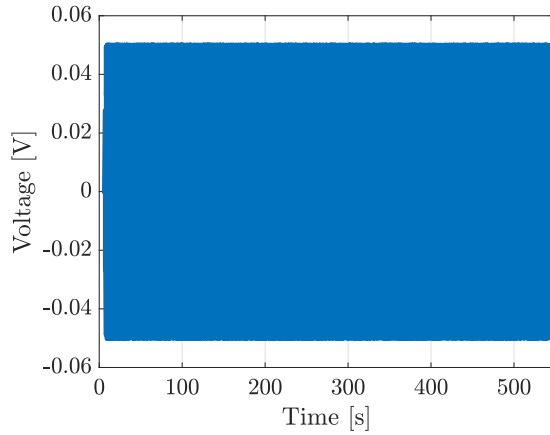


Figure 3.33: Time signal of the voltage at the terminals of the coil for the empty test.

It must be reminded that the measured voltage is the non-amplified signal. The amplifier has not been yet applied. Therefore, it means that this phenomenon is due to the amplifier and that it is from electrical nature. Unfortunately, no information about the electrical circuit of this amplifier is provided by the DongLing shaker supplier.

3.3 Conclusion

Thanks to these two experimental test campaigns, it can be concluded that the model of the shaker, constituting the first block of the virtual shaker testing, allows to simulate the reality in an accurate manner. However, these are not perfect and could be improved by adding, for example, more degrees of freedom in the model. This has been investigated in [6] and it has appeared to be quite complex for the parameter identification.

The shaker is now correctly modelled but the goal of the virtual shaker testing is to simulate the behaviour of more complex structures. For both realised test campaigns, simple masses were considered for the parameter identification process. Their own dynamics were not taken into account, they were considered as rigid bodies. To analyse the interaction between the shaker and a specimen, it is needed to couple the model of the device under test with the model of the electrodynamic shaker to truly represent the interaction between the structure being tested and the exciter.

Chapter 4

Coupling of a specimen to the shaker

At this time, the model of the electrodynamic shaker is validated. However, the aim of a virtual shaker testing is to simulate a complete shaker test. It is therefore needed to know how to couple the model of the specimen to be tested to the shaker model. In this chapter, the methodology to follow is first explained. After that, this method is applied to two different case studies and the models are validated by comparing them with experimental measurements.

4.1 Methodology

In this work, two different methods to couple a dynamic model of a specimen to the lumped parameter model of the electrodynamic shaker are considered: by using a numerical reduced model of the specimen or by using an experimental model.

4.1.1 Numerical model of a specimen coupled to the shaker

The idea of this first method is to couple a numerical model of the structure to the model of the shaker. The process to follow is described in Figure 4.1. The first objective, before coupling it to the shaker model is to have a reliable model of the specimen. The Computer-Aided Design (CAD) model is first built or directly used from the supplier if provided. The natural frequencies and mode shapes of the structure are then identified. In parallel, an experimental modal analysis is performed in order to update and validate the numerical model. The mode shapes are therefore obtained experimentally. The numerical model being much larger than the experimental one, a model reduction is needed. The numerical modal parameters and mode shapes may then be compared to the experimental ones. If there is a satisfying correlation between both approaches, the model is validated and may be coupled to the model of the shaker. If it is not, the specimen

model must be updated by modifying its CAD model. To do so, for example, more details must be added to the model, the boundary conditions of the specimen coupled to the shaker may be represented differently, etc. Each of these steps of the coupling between the specimen and the shaker are more completely described in the following sections.

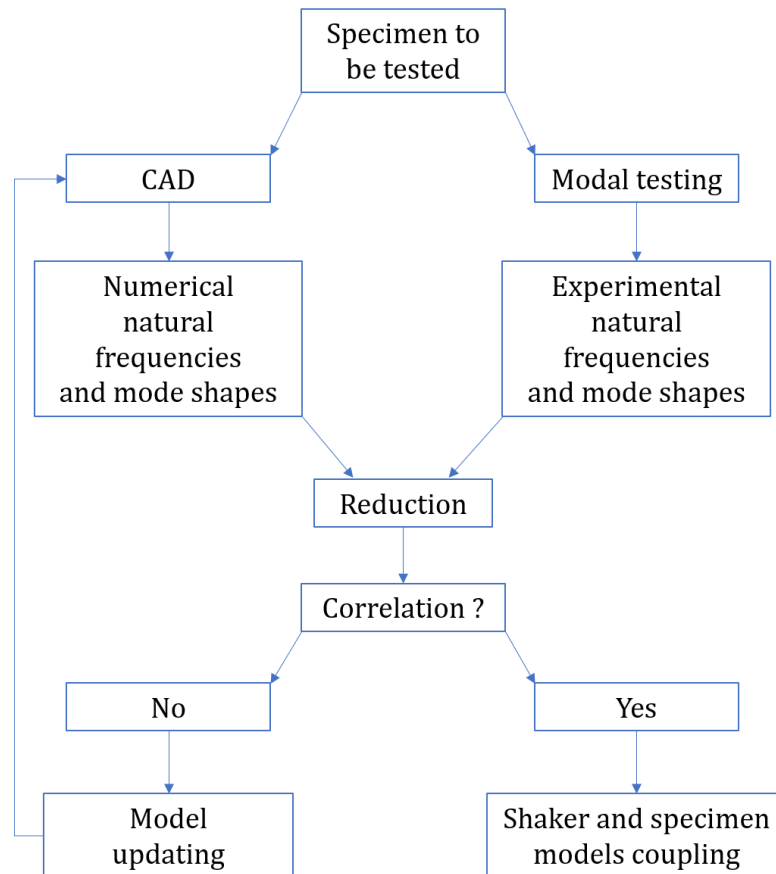


Figure 4.1: Model updating process.

Numerical model of the specimen

The first requirement to prepare the coupling of a specimen and the shaker model is to develop an accurate and good numerical model of the considered specimen. The CAD model of the device can be used if it is made available by its supplier company or it has to be built otherwise. The first objective of this procedure is to observe the dynamic behaviour of the structure on its own before coupling it to the shaker. Therefore, the numerical model of the structure must be meshed so that its natural frequencies may be computed. After that, the mode shapes of the device are analysed.

During the model update process, the model is improved by progressively increasing its complexity. The first version of the model is indeed quite simple. The boundary conditions of the problem are estimated by clamping the bottom of the specimen, at

the location where the experimental specimen is fixed on the shaker. The meshing of the specimen CAD model is then optimised in this configuration: a convergence study is done.

As said previously, to validate the model of the specimen, the numerical natural frequencies and mode shapes are compared with the ones obtained experimentally. In this work, for the large considered structures such as the expander, the best way to perform the impact testing is to fix the specimen on the shaker. To compare numerical and experimental results, the model has to account for this. The boundary conditions of the model must mimic the behaviour of the shaker. Therefore, when the meshing is validated by the convergence study, the boundary conditions of the specimen model are enhanced.

To do so, the shaker is considered in the model by introducing stiffness elements. Rather than clamping the bottom of the specimen, its lower face is now rigidly linked to a point representing the table of the shaker. In order to model the suspensions of the table, a stiffness element is placed between the table point and a clamped point representing the body of the shaker. Its stiffness value k_s is already known from the identified shaker parameters presented in Chapter 3. To account for the coil behaviour, a second stiffness element is introduced in the model. Once again, this stiffness value is already known. These two elements are shown in Figure 4.2.

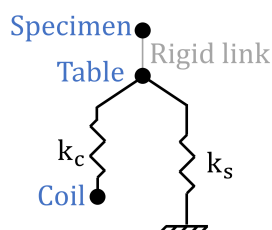


Figure 4.2: Scheme of the boundary conditions of the specimen fixed on the shaker.

Thanks to the improved finite element model, the natural frequencies and the modes of the specimen are computed. One can note that lots of modes may be computed by the numerical model, it is therefore needed to select a finite set of modes. To choose them, the concept of effective mass is used. The effective mass defines the "significance" of a vibration mode. It helps to see which modes and which parameters govern the dynamic phenomena [21]. Modes with high effective mass are likely to be easily excited by base excitation, and thus the shaker may transmit them energy [22]. These are the modes of interest. Therefore, only the modes having a certain effective mass are analysed. The natural frequencies of the specimen and its mode shapes are finally estimated and must be compared to experimental data.

Experimental modal analysis

To be able to validate the specimen model, an experimental modal analysis is performed: an impact testing is carried out on the specimen. In this way, the numerical and experimental mode shapes and natural frequencies can be compared. This test consists in hitting the structure with an impact hammer to excite it while measuring the force of the impact. Accelerometers are placed on the device and record the corresponding acceleration at several locations.

Thanks to an acquisition system, the frequency response functions of the acceleration over the force are obtained. Thanks to these, the natural frequencies and the modes of the structure are identified but this will be detailed later. The focus can first be made on the acquisition. Different parameters must be specified in the acquisition software. The frequency bandwidth of interest W and the number of spectral lines n are first required to determine the frequency resolution. Indeed, the frequency step is defined as:

$$\Delta f = \frac{W}{n}. \quad (4.1)$$

The acquisition time is then computed as:

$$T = \frac{1}{\Delta f}. \quad (4.2)$$

Finally, the last parameter to define in the acquisition software is the sampling frequency. This must be sufficiently high to have a sufficient resolution of measured signal. Moreover, in order to avoid aliasing phenomena, the sampling frequency f_s is taken 2.56 times larger than the bandwidth as it is explained in [19]. Indeed, the Nyquist-Shannon sampling theorem states that the bandwidth W of the sampled signal must be smaller than half of the sampling frequency so that the sampled signal has the same spectrum as the analog signal. As a consequence, in practice, the sampling frequency is usually set to be 2.56 times larger than the bandwidth.

The time response measured by accelerometers is observed on a finite length of time. A problem of leakage could therefore introduce amplitude and frequency errors so windowing is needed in order to minimise this problem. Indeed, an exponential window is needed to ensure that the acceleration response decays to zero before the ending time of the measurement [23]. The effect of such a window is shown in Figure 4.3.

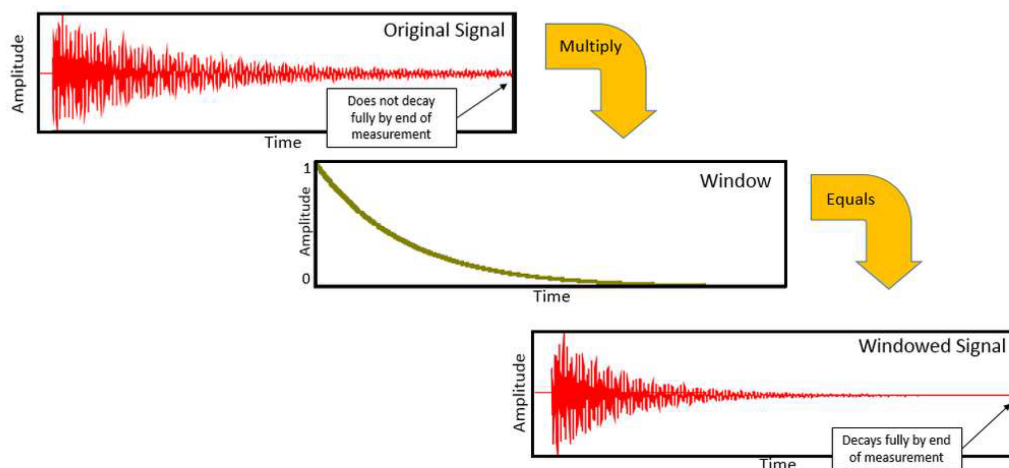


Figure 4.3: Effect of an exponential window on the accelerometer signal [23].

Moreover, a rectangle window is used for the excitation. Indeed, since it is an impact excitation, it is wanted to remove the noise around the force peak that the hammer could measure. Additionally, in order to minimise spurious random noise from the signals, three impacts for each test are performed at the same location and the results are averaged. It allows to reduce the noise of the signals.

An important decision to be made is the location of the impact points and of the sensors. Since the mode shapes are first estimated by the numerical model, it is known where the structure deforms the most. Therefore, the accelerometers are placed there to catch the different modes as accurately as possible. If it is expected that modes will react in the three directions, triaxial accelerometers are used to record the accelerations over the three directions of space. Moreover, it is recommended to excite the structure in the three directions.

The FRFs of the impact force over the measured acceleration are registered by the acquisition system. The natural frequencies of the structure can then be extracted from this set of FRFs. To do so, the Multiple Input Least-Squares Complex Exponential, or polyreference LSCE (p-LSCE) method is used. This specific method is chosen because the author has developed the simple LSCE method in a previous scholar work [24]. Its implementation is thus modified to be adapted to multiple inputs. After modification, it allows to estimate the poles (frequencies and damping ratios) of the structure. It is a time domain method since it uses the impulse response function (IRF). Therefore, the inverse fast Fourier transform is first applied on the FRFs to enter in the time domain.

The p-LSCE can be briefly explained but all the mathematical details can be found in the Appendix B. Only the main equations, essential for understanding, are given here.

In [25], it is shown that the poles of the structure are identified by computing the roots \mathbf{Z}^k of the polynomial Equation 4.3:

$$(\alpha_0 + \alpha_1 \mathbf{Z} + \alpha_1 \mathbf{Z}^2 + \dots + \alpha_q \mathbf{Z}^q) \mathbf{L} = \mathbf{0}, \quad (4.3)$$

where \mathbf{L} is a matrix of modal participation factors and \mathbf{Z}_k are equal to $e^{\lambda_k \Delta t}$, with λ_k , the poles, and Δt , the time resolution. α are assessed coefficients based of the IRFs expression as explained in Appendix B. Moreover, to avoid the solution $\alpha = 0$, the constraint $\alpha_q = \mathbf{I}$ is imposed.

The roots of the polynomials are thus computed. These roots are known to have the form $\mathbf{Z}_k = e^{\lambda_k \Delta t}$, so the complex eigenvalues λ_k are found (with $k = 1, 2, \dots, q$ and q is the system order).

Since the poles have the form:

$$\lambda_k = \omega_k \left(-\zeta_k + i \sqrt{1 - \zeta_k^2} \right), \quad (4.4)$$

the values of the natural frequency ω_k and the damping ratio ζ_k , are assessed as follows:

$$\begin{cases} \omega_k = |\lambda_k|, \\ \zeta_k = -\frac{\text{Real}\{\lambda_k\}}{\omega_k}. \end{cases} \quad (4.5)$$

The modal parameters can then be computed for a specific order q of the system.

By selecting a q -order system, an assumption is made on the number of modes in the frequency range of interest [20]. It is thus an important choice to make. To avoid this issue, the multi-input LSCE method explained here above is solved for increasing model orders q . All the solutions are then plotted on a same figure (the natural frequencies on the abscissa and the model order on the ordinate); this yields the stabilisation diagram.

To distinguish the physical modes from the spurious modes, the stability of the poles is checked. The modal parameters at the order p are compared with the modal parameters obtained at the previous order $p - 1$. The frequency and damping stability are assessed if the following conditions are respectively verified [26]:

$$\frac{\omega_k(p) - \omega_k(q - 1)}{\omega_k(p - 1)} \leq \delta_{\omega_k} = 1\%, \quad (4.6)$$

$$\frac{\zeta_k(p) - \zeta_k(q - 1)}{\zeta_k(p - 1)} \leq \delta_{\zeta_k} = 5\%. \quad (4.7)$$

However, it will be shown later with a case study that these stabilisation diagrams are not always clear and it is sometimes difficult to see the poles that are stabilised. To "clean" these diagrams, an alternative p-LSCE method is implemented.

In fact, another criterion can be used to distinguish spurious modes from physical modes. By looking at Equation 4.5, it can be seen that the sign of the damping ratios is the opposite sign of the real part of the pole. It means so that if a pole has a positive real part, it would lead to a non-physical solution since a negative damping ratio has no sense.

In [27] and [28], it is shown that, if the constraint $\alpha_q = \mathbf{I}$ defined here above is replaced by $\alpha_0 = \mathbf{I}$, it sets the real part of the spurious poles to be positive values. Modifying this constraint is equivalent to flip the time vector. In Figure 4.4, the imaginary part of the poles are plotted with respect to their real part for both versions of the p-LSCE (the classical and alternative p-LSCE methods). As a matter of fact, with the alternative method, the spurious poles are sent to the non-physical region. It will be shown later with a practical case that the stabilisation diagram is much clearer with the alternative method.

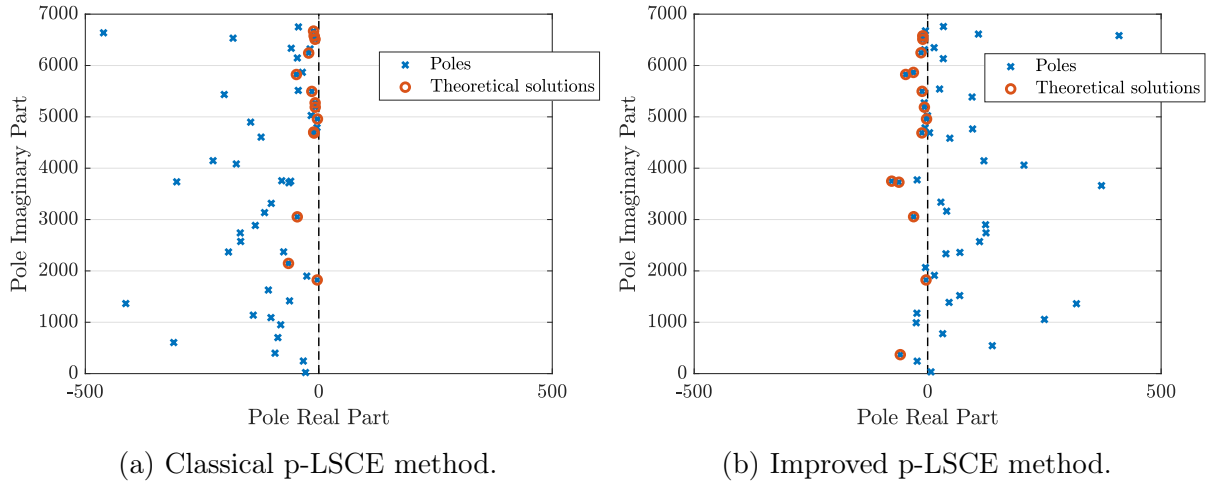


Figure 4.4: Poles diagram.

Thanks to this method it is then possible to determine the poles that are stabilised. However, to validate its implementation, the results obtained with the p-LSCE are compared to the PolyMax method directly usable in LMS software. As opposed to the p-LSCE, it is used in the frequency domain [29]. It is also called the polyreference least-squares complex frequency-domain exponential method. It makes use of multiple-input-multiple-output FRFs so it also allows to consider all the accelerometers and all the impacts.

Now that the natural frequencies are known, the mode shapes have to be analysed. To extract them from the impact testing measurements, the Least-Squares Frequency Domain method (LSFD) is used. In combination with the LSCE method, it allows to compute the mode shape vectors based on the measured FRFs and on the identified poles. The next section explains how to compare the numerical modes with the experimental ones.

Comparison between numerical and experimental results

During the Experimental Modal Analysis (EMA), the acceleration is recorded only at some specific points. There is thus a spatial truncation: there are much less experimentally measured degrees of freedom than the number of degrees of freedom in the numerical model. Therefore, a model reduction is needed to finally compare the experimental and numerical mode shapes.

To compare these modes, the Modal Assurance Criterion (MAC) is used. This criterion is an indicator that evaluates the spatial correlation between mode shapes [30]. It allows to pair experimental modes with analytical ones. It must be paid attention to the fact that it only compares mode shapes, it does not consider the natural frequencies so, when the modes are coupled, it is important to compare their frequencies. This MAC indicator is bound between 0 and 1. If it is close to 1, it means that the modes are consistent. If it is close to 0, it means that the modes are not at all correlated. In this work, it is considered that only the modes having a MAC higher than 0.8 are correlated.

The MAC coefficients are computed as follows:

$$\text{MAC}(\boldsymbol{\psi}_{(i)}^{\text{exp}}, \boldsymbol{\psi}_{(j)}^{\text{num}}) = \left(\frac{\boldsymbol{\psi}_{(i)}^{\text{exp}T} \boldsymbol{\psi}_{(j)}^{\text{num}}}{\|\boldsymbol{\psi}_{(i)}^{\text{exp}}\| \|\boldsymbol{\psi}_{(j)}^{\text{num}}\|} \right)^2, \quad (4.8)$$

where $\boldsymbol{\psi}_{(i)}^{\text{exp}}$ are the eigenvectors obtained experimentally and $\boldsymbol{\psi}_{(j)}^{\text{num}}$ are the analytical eigenvectors extracted from the numerical model. The index i varies between 1 and the number of experimental modes, and j between 1 and the number of the numerical modes.

If the correlation criterion is not acceptable, it is needed to modify the numerical model. The non-sufficient correlation may come from the CAD model. To improve the correlation, small details must be added to it. Moreover, the boundary conditions are sometimes not representative enough and need to be modified. When the MAC and the error on the frequencies finally show a good correlation between experimental and numerical modes, the model of the structure is validated and may be coupled to the model of the shaker.

Coupling of shaker and specimen models

The final goal of this section is to introduce the numerical model of the specimen in the virtual shaker testing. The model of the studied structure being validated, it must be coupled to the model of the shaker. To do so, a superelement is created thanks to the Craig-Bampton method implemented in the *Samcef* software.

The Craig-Bampton method is a reduced-order model method, it allows to reduce the dimension of the problem [31]. Moreover, the size of the numerical model is usually too large to be used entirely in the virtual shaker testing. Indeed, in the *Simulink* model, the acceleration, the voltage and the current are computed for each time step. If the acceleration of each point of the Finite Element Model (FEM) had to be computed in the time domain, it would be too much time consuming. It is why it is essential to reduce the numerical model, to compute the problem only at some points.

This Craig-Bampton method is a substructuring technique. The different parts of the model that must be assembled are reduced on common interfaces [32]. According to this method, the dynamic behaviour of the substructure may be fully described by:

- the static modes: a unit displacement is imposed on the degrees of freedom of the interface. These DoFs are the boundary degrees.
- the internal vibration modes: the boundary degrees of freedom are clamped.

This is illustrated by Figure 4.5.

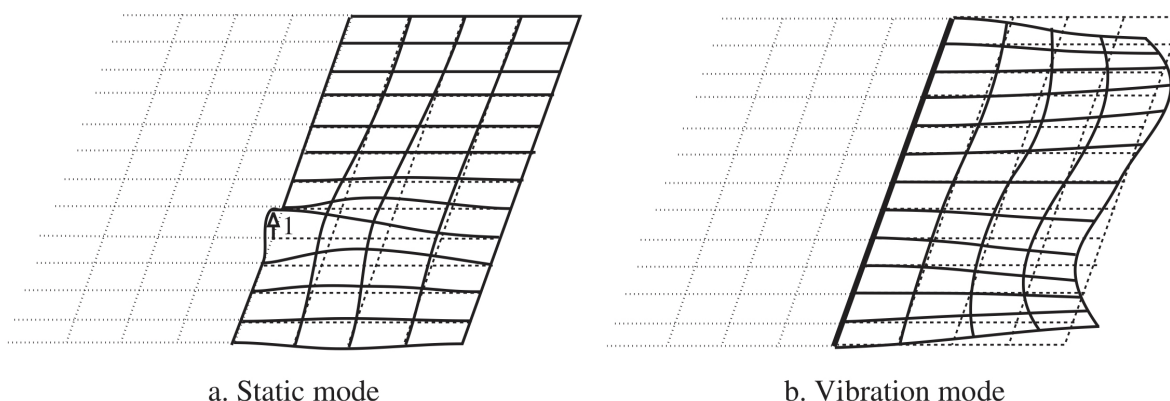


Figure 4.5: Static modes and internal vibration modes of a substructure [32].

Therefore, only some degrees of freedom are studied. The model of the subsystem is thus reduced and the degrees of freedom are separated into two parts:

- \mathbf{x}_B , the boundary degrees of freedom;

- \mathbf{x}_I , the subsystem internal degrees of freedom.

The subsystem contribution to the complete system is written as follows:

$$\begin{bmatrix} \mathbf{M}_{BB} & \mathbf{M}_{BI} \\ \mathbf{M}_{IB} & \mathbf{M}_{II} \end{bmatrix} \begin{pmatrix} \ddot{\mathbf{x}}_B \\ \ddot{\mathbf{x}}_I \end{pmatrix} + \begin{bmatrix} \mathbf{C}_{BB} & 0 \\ 0 & \mathbf{C}_{II} \end{bmatrix} \begin{pmatrix} \dot{\mathbf{x}}_B \\ \dot{\mathbf{x}}_I \end{pmatrix} + \begin{bmatrix} \mathbf{K}_{BB} & 0 \\ 0 & \mathbf{K}_{II} \end{bmatrix} \begin{pmatrix} \mathbf{x}_B \\ \mathbf{x}_I \end{pmatrix} = \begin{pmatrix} \mathbf{p}_B \\ 0 \end{pmatrix}. \quad (4.9)$$

From the second line of Equation 4.9, the acceleration of the internal degrees of freedom may be obtained:

$$\ddot{\mathbf{x}}_I = -\mathbf{M}_{II}^{-1} \mathbf{M}_{IB} \ddot{\mathbf{x}}_B - \mathbf{M}_{II}^{-1} \mathbf{C}_{II} \dot{\mathbf{x}}_I - \mathbf{M}_{II}^{-1} \mathbf{K}_{II} \mathbf{x}_I. \quad (4.10)$$

To introduce the mechanical system of the substructure in the model, it must be transformed into a state-space representation. The later is defined by:

$$\dot{\mathbf{q}} = \mathbf{A}\mathbf{q} + \mathbf{B}\mathbf{u}, \quad (4.11)$$

$$\mathbf{y} = \mathbf{C}\mathbf{q} + \mathbf{D}\mathbf{u}. \quad (4.12)$$

This transformation is realised thanks to the state variable \mathbf{q} defined by:

$$\mathbf{q} = \begin{pmatrix} \mathbf{x}_I \\ \dot{\mathbf{x}}_I \end{pmatrix}. \quad (4.13)$$

The first equation of the state-space representation (cf. Equation 4.11) is obtained by using the identity equation and Equation 4.10:

$$\underbrace{\begin{pmatrix} \dot{\mathbf{x}}_I \\ \ddot{\mathbf{x}}_I \end{pmatrix}}_{\dot{\mathbf{q}}} = \underbrace{\begin{bmatrix} 0 & \mathbf{I} \\ -\mathbf{M}_{II}^{-1} \mathbf{K}_{II} & -\mathbf{M}_{II}^{-1} \mathbf{C}_{II} \end{bmatrix}}_{\mathbf{A}} \underbrace{\begin{pmatrix} \mathbf{x}_I \\ \dot{\mathbf{x}}_I \end{pmatrix}}_{\mathbf{q}} + \underbrace{\begin{bmatrix} 0 \\ -\mathbf{M}_{II}^{-1} \mathbf{M}_{IB} \end{bmatrix}}_{\mathbf{B}} \underbrace{\ddot{\mathbf{x}}_B}_{\mathbf{u}}. \quad (4.14)$$

The second equation of the state-space representation (cf. Equation 4.12) gives the output values. When the aim of the virtual shaker testing is to simulate the dynamics of the shaker with a structure represented by a superelement, it may be useful to know the acceleration at some specific points of the non-reduced structure. Therefore, the two outputs of interest are the reaction forces of the specimen on the shaker and the acceleration of a selection of points: the points of the interface and other chosen points. The aim is here to choose the acceleration as output at the points where the the accelerations have been measured during the impact testing. In that way, the numerical and experimental results may be compared.

The reaction force is expressed as:

$$\mathbf{R} = \mathbf{M}_{BI} \ddot{\mathbf{x}}_I, \quad (4.15)$$

and the acceleration of the nodes of interest is expressed as:

$$\ddot{\mathbf{q}}_{\alpha\beta} = \boldsymbol{\phi}_I \ddot{\mathbf{x}}_I + \boldsymbol{\phi}_B \ddot{\mathbf{x}}_B, \quad (4.16)$$

where $\boldsymbol{\phi} = [\boldsymbol{\phi}_I, \boldsymbol{\phi}_B]$ is the transformation matrix between selected degrees of freedom and state-space degrees of freedom. This matrix is computed by *Samcef*.

The expression of $\ddot{\mathbf{x}}_I$ is given by the second line of Equation 4.14. It can therefore be plugged into Equations 4.15 and 4.16 and it gives the output equations of the state-space representation. This system of equations is shown in Equation 4.17.

$$\underbrace{\begin{pmatrix} \mathbf{R} \\ \ddot{\mathbf{q}}_{\alpha\beta} \end{pmatrix}}_{\mathbf{y}} = \underbrace{\begin{bmatrix} -\mathbf{M}_{BI}\mathbf{M}_{II}^{-1}\mathbf{K}_{II} & -\mathbf{M}_{BI}\mathbf{M}_{II}^{-1}\mathbf{C}_{II} \\ \mathbf{M}_{II}^{-1}\boldsymbol{\phi}_I\mathbf{K}_{II} & \mathbf{M}_{II}^{-1}\boldsymbol{\phi}_I\mathbf{C}_{II} \end{bmatrix}}_{\mathbf{C}} \underbrace{\begin{pmatrix} \mathbf{x}_I \\ \dot{\mathbf{x}}_I \end{pmatrix}}_{\mathbf{q}} + \underbrace{\begin{bmatrix} -\mathbf{M}_{BI}\mathbf{M}_{II}^{-1}\mathbf{M}_{BI} \\ -\mathbf{M}_{II}^{-1}\boldsymbol{\phi}_I\mathbf{M}_{BI} + \boldsymbol{\phi}_B \end{bmatrix}}_{\mathbf{D}} \underbrace{\ddot{\mathbf{x}}_B}_{\mathbf{u}} \quad (4.17)$$

Now that the expression of the four state-space matrices \mathbf{A} , \mathbf{B} , \mathbf{C} , \mathbf{D} are known, they might be introduced in the VST model of the shaker. Their introduction in the *Simulink* model is illustrated in Figure 4.6 where the subsystem block is highlighted in green. This added block takes the state-space matrices as input and returns the specimen reaction force and the accelerations of the stored degrees-of-freedom as outputs.

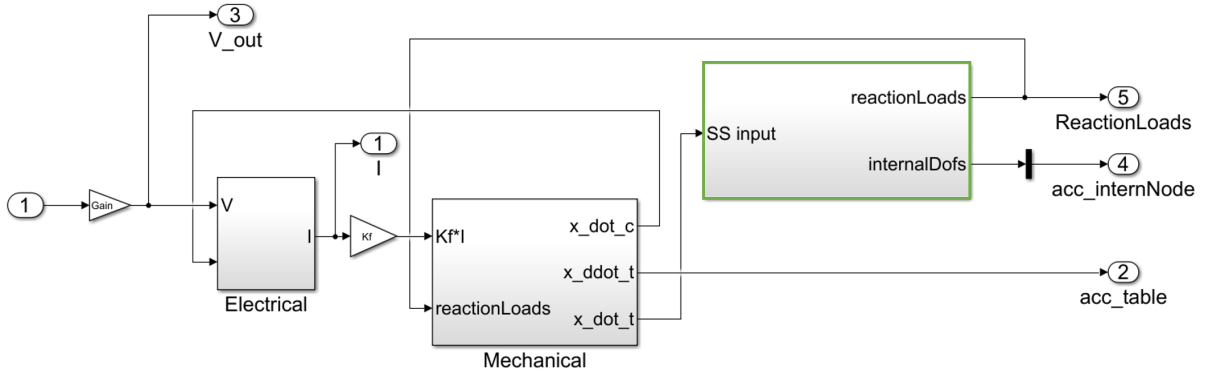


Figure 4.6: Introduction of the superelement (green box) in the *Simulink* model.

To summarise, it can be explained how the superelement is built and introduced in the *Simulink* shaker model. This is shown in Figure 4.7. First, in the *Siemens NX* numerical model of the specimen, the node of the interface is retained. Then, the nodes at which it is wanted to get the acceleration are selected. After that, the superelement is computed with *Samcef*. Thanks to a MATLAB routine provided by *Samcef*, the matrices \mathbf{A} , \mathbf{B} , \mathbf{C} , and \mathbf{D} are computed. In a MATLAB code, the parameters of the shaker are defined, these matrices are loaded, and the *Simulink* model is called. Thanks to this

model, the acceleration at the selected nodes and the reaction force at the interface are finally computed.

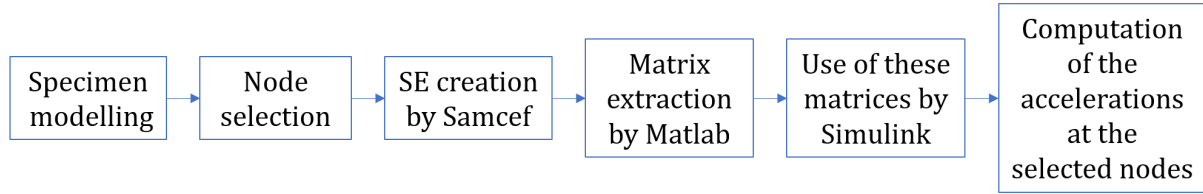


Figure 4.7: Numerical coupling process of a specimen model to the shaker model.

Some vibration campaigns may be then simulated and the behaviour of the device coupled to the shaker may be predicted by analysing the results. The acceleration-over-current and acceleration-over-voltage FRFs are constructed so that the resonance frequencies are estimated. To validate these simulations, they must be compared to experimental results. Therefore, a test campaign is performed with the shaker and the Device Under Test (DUT) fixed on it. A sine sweep excitation is used as it was done in Chapter 3 for the validation of the identification method. The measured frequency response functions can be then compared to the simulated ones. If they are well superposed, the model is finally validated.

4.1.2 Experimental model of specimen coupled to the shaker

The second way to couple the model of the specimen to the model of the shaker is to use an experimental model of this specimen. To do so, the Frequency-Based Substructuring (FBS) method is used.

With this method, components characterised by experimental analysis can be coupled with components modelled numerically. This approach is useful in the case where the CAD model of a specimen is not available. It allows to get a model even if the structure is complex and if it is difficult to obtain a converged numerical model. The main idea is to measure systems separately and to recombine them together afterwards. Therefore, in this work, the specimen is characterised by an experimental analysis that allows to build an experimental superelement. It is then coupled to the numerical model of the shaker.

The system is composed of two components: A the specimen and B the shaker, as illustrated in Figure 4.8. The input i applied to B goes through B , through the A - B connection c , through A and finally through the output degree of freedom m of A , the output of interest in the case of virtual shaker testing. The output m is here the acceleration at a specific point of the specimen.

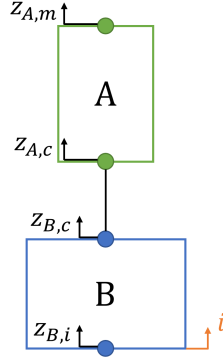


Figure 4.8: FBS principle scheme.

Considering a rigid connection, if the shaker excitation is the only force applied to the considered components, the FRF of a degree of freedom of A as a response to the excitation of the shaker B is written as in Equation 4.18:

$$H_{A,mi} = H_{A,mc} (H_{A,cc} + H_{B,cc})^{-1} H_{B,ci}, \quad (4.18)$$

where the notations correspond to:

$$\begin{aligned} H_{A,mc} &: \text{A output/connection FRF} \\ H_{A,cc} &: \text{A connection/connection FRF} \\ H_{B,ci} &: \text{B connection/input FRF} \\ H_{B,cc} &: \text{B connection/connection FRF} \end{aligned} \quad (4.19)$$

The expression of Equation 4.18 can be proved by the following developments. At first, the force equilibrium writes:

$$F_i H_{B,ci} + (-F_c) H_{B,cc} = F_c H_{A,cc} \quad (4.20)$$

$$\Leftrightarrow F_i H_{B,ci} = F_c (H_{B,cc} + H_{A,cc}) \quad (4.21)$$

$$\Leftrightarrow F_i \frac{H_{B,ci}}{(H_{B,cc} + H_{A,cc})} = F_c \quad (4.22)$$

where F_i is the force created by the input i , and F_c is the force of contact between specimen A and the shaker B .

By using the definition of the FRF, F_c is replaced by:

$$z_{a,m} = F_c H_{A,mc}, \quad (4.23)$$

and the equation becomes:

$$F_i \frac{H_{B,ci}}{(H_{B,cc} + H_{A,cc})} = \frac{z_m}{H_{A,mc}}, \quad (4.24)$$

and finally

$$H_{A,mi} = \frac{z_m}{F_i} = H_{A,mc} \frac{H_{B,ci}}{(H_{B,cc} + H_{A,cc})} = H_{A,mc} (H_{A,cc} + H_{B,cc})^{-1} H_{B,ci}. \quad (4.25)$$

It means that to compute the FRF $H_{A,mi}$ linking the output acceleration to the input, four FRFs must be first computed: $H_{A,cc}$, $H_{B,cc}$, $H_{B,ci}$, and $H_{A,mc}$. The combined dynamics can be predicted using these FRFs. Therefore, the FRFs of structure B (the shaker) are obtained using the numerical model of the shaker and the FRFs of structure A are obtained experimentally using a impact test of the DUT.

One can note that the degrees of freedom of the connection between A and B are not reachable when the specimen is clamped on the shaker. No impact can be done on this point. Therefore, the theory of *Virtual Point Transformation* (VPT) is used to retrieve the FRF at the precise location of the connection using multiple FRFs around the point of interest. Local rigid behaviour must be assumed in the vicinity of the virtual point and the module *pyFBS* is used.

This method uses an impact testing to create an "experimental superelement" [33]. The aim is to create a point on the interface between the specimen and the structure that is compatible between the two substructures (the shaker modelled numerically and the specimen modelled experimentally). The idea is to describe this point by six degrees of freedom: the translations along the three global axes and the rotations along these three axes. To do so, at least three triaxial accelerometers and six impacts are needed. The measured Dofs allow then to estimate the dynamics of the virtual points.

Finally, the FRF of the acceleration over the input can be computed for any point involved in the experimental analysis. The experimental superelement is built accordingly and the dynamics of the assembly shaker/specimen can be simulated. This methodology will be applied on a small structure fixed on the 100-lbf shaker.

It has to be noted that in this case, a rigid connection is considered between the specimen and the shaker. However, these two are assembled with screws. These screwed connections may create specific local behaviours that may be difficult to model.

This method allows to obtain a model without having to build a numerical model but it has some disadvantages. Indeed, with a superelement, all the degrees of freedom are accessible, the acceleration of any point of the structure can be obtained. With this method, only few acceleration points are accessible. Moreover, an experimental modal analysis is very time-consuming, even more for complex or large structure.

4.2 100-lbf shaker: beam case

In this section, two coupling methods, numerical and experimental, are applied on a studied case. A beam made of steel is tested on the 100-lbf shaker in order to validate these two methods.

4.2.1 Numerical coupling between specimen and shaker

To validate the method of numerical coupling, the CAD model of a specimen is used. In a first time, a simple mass is used only to validate the implementation of the superelement then the small beam of interest is used to validate the numerical coupling methodology.

At first, the mass used in Section 3.2.1 is modelled. Its fem is built and a superelement is created to couple it to the shaker model. This mass had already been virtually tested in the beginning of this work but only by adding its mass to the mass of the shaker table. It is now simulated by using its superelement.

The finite element model of this little mass is done in *Siemens NX* and is illustrated in Figure 4.9. Then *Samcef* is used to create the superelement in which it is possible to use Craig-Bampton's method as a reduction method. In this case only one node is retained at the centre of the base of the mass.

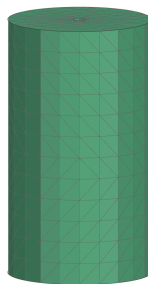


Figure 4.9: FEM of mass of 409 g.

A MATLAB routine allows to extract the mass and stiffness matrices from *Samcef* files and then builds the matrices **A**, **B**, **C**, **D** of the state-space representation (cf. Equations 4.14 and 4.17). These are introduced in *Simulink* and the dynamics of the system is simulated. The acceleration-over-current and acceleration-over-voltage FRFs are computed and they are compared to the simulated curves of Chapter 3 where the mass is just added to the mass of the table in the model. This comparison is shown in Figure 4.10. These curves are perfectly superposed. It means that the superelement method is well implemented and that the assumption of a point mass of the Chapter 3 is realistic.

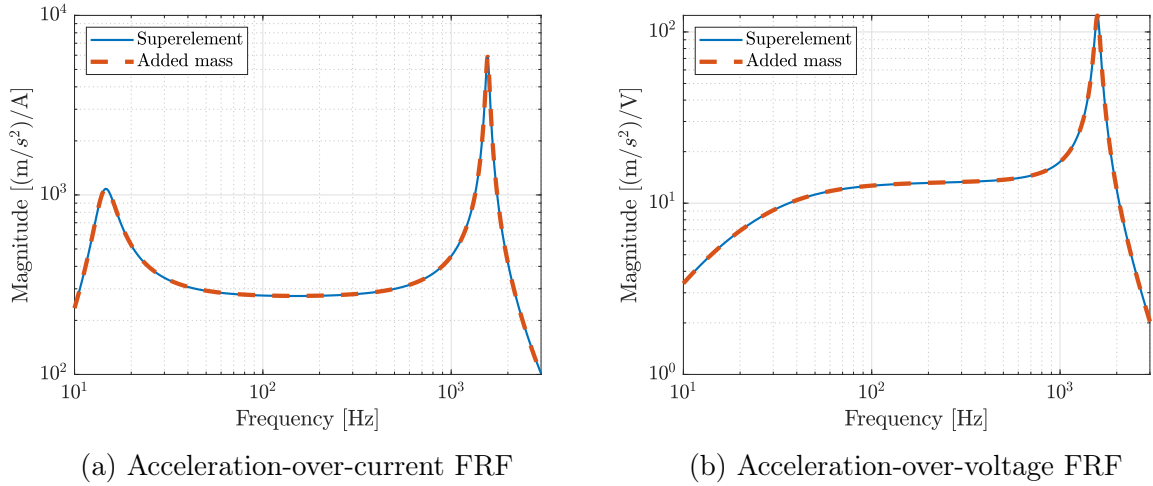


Figure 4.10: Comparison of FRFs obtained with the superelement or by adding the mass of the specimen to the mass of the table

The superelement theory can now be applied on a more complex structure. The beam presented in Figure 4.11 is fixed on the shaker. Once again, a sine sweep is realised between 5 Hz and 3 000 Hz and the same parameters as the ones listed in Table 3.1 are kept.



Figure 4.11: Sine sweep test in open loop on the VTS VG-100 shaker with a beam structure.

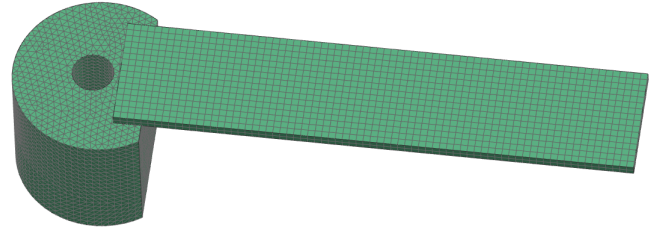


Figure 4.12: FEM of the beam structure.

Thereafter, the finite element model is realised. The CAD model of the beam is illustrated in Figure 4.12. The node at the centre of the base of the structure, where it is attached to the shaker, is the retained node of the superelement. During the model reduction, the node at the end of the beam and the node on the top of the base mass are kept so that it is possible to retrieve the acceleration at these points. The superelement is then coupled to the shaker model and the simulation of a complete test is launched within the *Simulink* environment.

As said in Section 4.1.1, the reaction force of the specimen on the shaker can be simulated. It is an output of the *Simulink* model (as it is shown in Figure 4.6). The reaction of the beam is thus plotted in Figure 4.13.

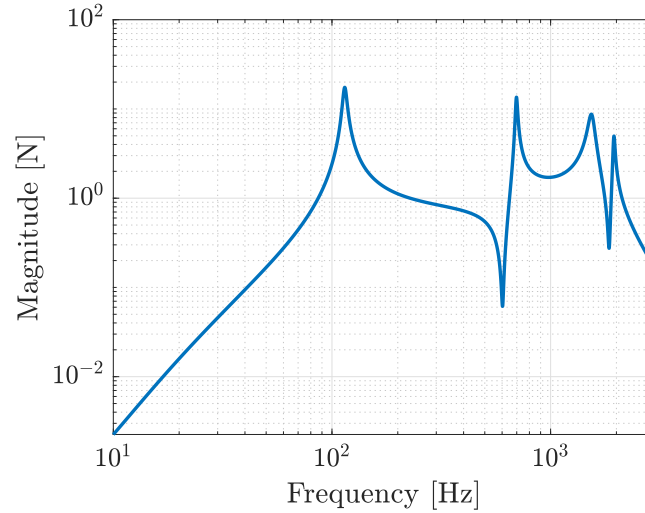
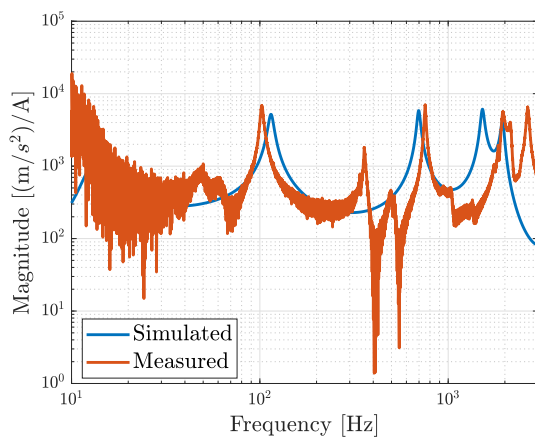


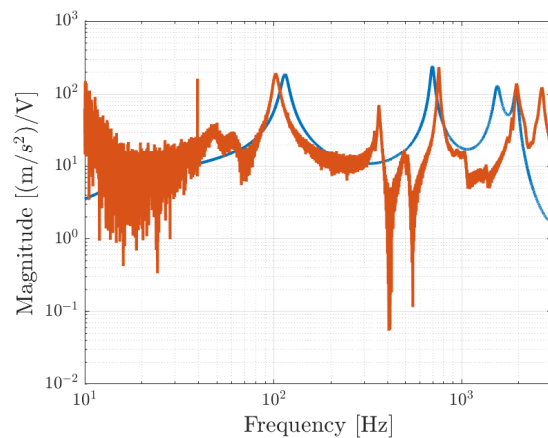
Figure 4.13: Reaction force of the beam on the shaker.

The shaker user could be interested in knowing the force applied by the specimen on the shaker depending on frequency of excitation. This graph shows the force that the shaker has to provide in order to make the specimen vibrate.

After that, the FRFs related to the point at the end of the beam are computed and are compared to the experimental results. The analytical and experimental acceleration-over-current FRFs are superposed in Figure 4.14a and the acceleration-over-voltage FRFs are superposed in Figure 4.14b.



(a) Acceleration-over-current FRF



(b) Acceleration-over-voltage FRF

Figure 4.14: Comparison of the experimental and simulated frequency response functions when a superelement is used for a beam structure.

Globally, the behaviour of the system is well estimated by the VST. However, some measured resonances are not predicted. This could come from the fact that the shaker model does not take the rotation into account since only the vertical degrees of freedom are represented in the model. Moreover, there is a small shift in frequencies at the identified peaks of resonance. This could come from the simplicity of the shaker model or from the coupling between the specimen model and the shaker model. To conclude, this coupling method gives not perfect but satisfying results.

4.2.2 Experimental coupling between specimen and shaker

In this section, the methodology explained for the experimental coupling of specimen to the model of the shaker is applied to the 100-lbf shaker. It is then compared to the numerical coupling and to the measurements performed with the sine sweep excitation explained in the previous section.

As it is explained in Section 4.1.2, four different FRFs are needed to use the FBS method: $\mathbf{H}_{B,cc}$, $\mathbf{H}_{B,ci}$, $\mathbf{H}_{A,cc}$, and $\mathbf{H}_{A,cm}$ where c is the connection between both parts, i is the input, so the current of the coil, and m is here the acceleration of the point at the beam tip. Based on these FRFs, the output-over-input FRF of interest of the specimen, $\mathbf{H}_{A,mi}$, can be computed.

In a first time, the FRFs related to the system B (the shaker), are easily synthesised. Indeed, the FRFs of structure B are obtained using the numerical model of the shaker implemented in *Simulink*. These FRFs are illustrated in Figure 4.15 and 4.16.

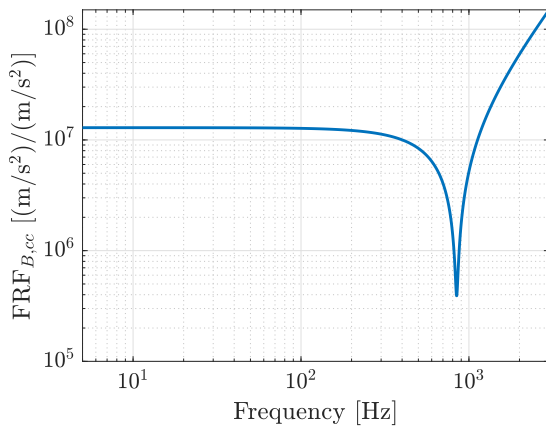


Figure 4.15: Synthesised connection-over-connection FRF of the shaker.

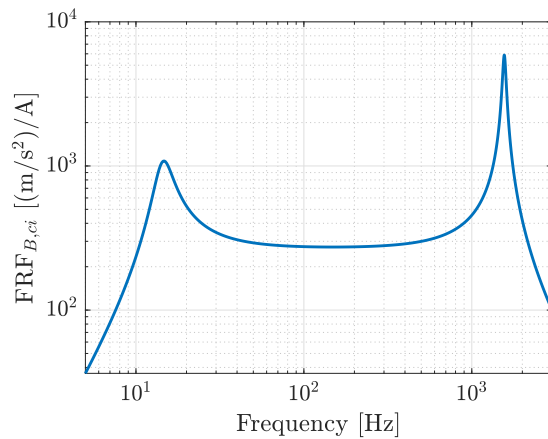


Figure 4.16: Synthesised connection-over-input FRF of the shaker.

To compute the FRFs related to the specimen A , the VPT is used. To do so, it is needed to realise an impact testing. As explained earlier, accelerometers have to be placed as close as possible to the interface. In this way, the FRFs are retrieved at the location of the connection. Four accelerometers are placed around the base of the beam, as shown in Figure 4.17. Indeed, an accelerometer is fixed at the back of the base but is not visible in this picture. Then seven impacts are performed.

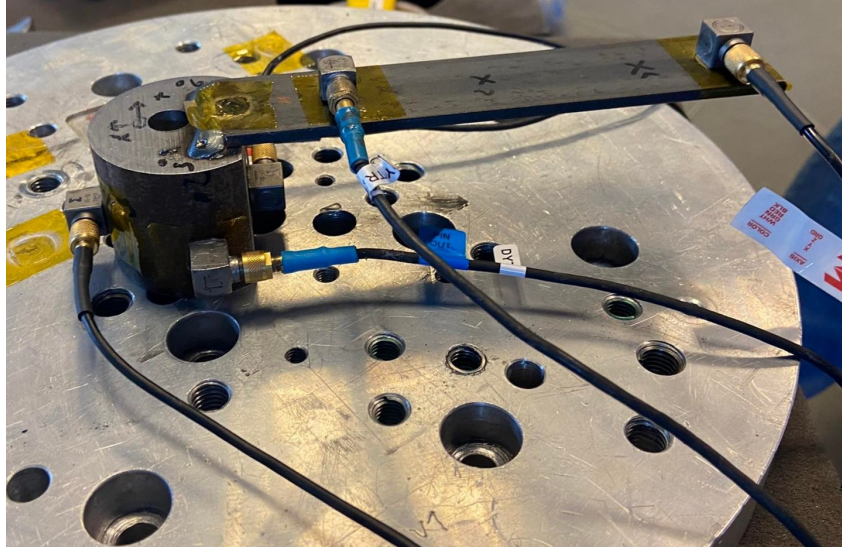


Figure 4.17: Reaction force of the beam on the shaker.

From the FRFs measured by these four accelerometers, the FRFs of the specimen A are computed. These are shown in Figure 4.18 and 4.19.

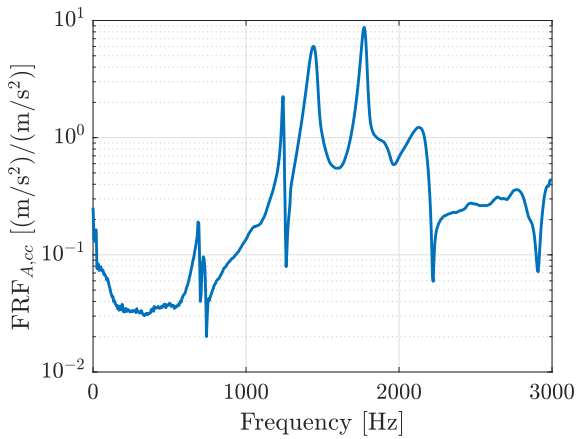


Figure 4.18: Synthesised connection-over-connection FRF of the specimen.

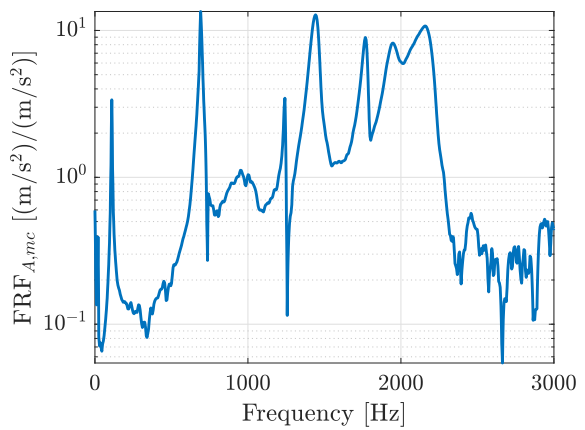


Figure 4.19: Synthesised output-over-connection FRF of the specimen.

The four needed FRFs being known, they are introduced in Equation 4.18 and the input-over-acceleration FRF $\mathbf{H}_{A,im}$ is finally synthesised. It is drawn in Figure 4.20 where

it is compared to the FRFs simulated with the numerical superelement and with the ones measured during the sine sweep.

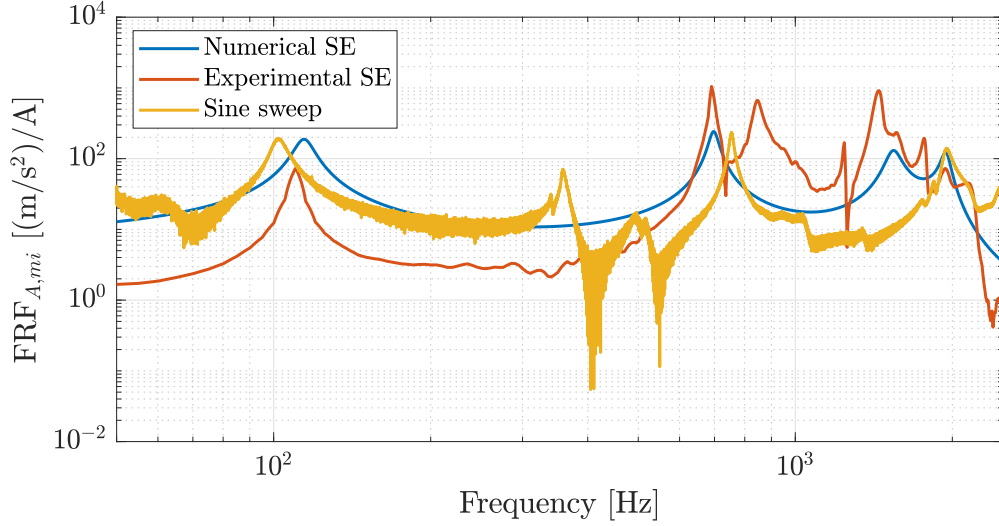


Figure 4.20: Synthesised output-over-input FRF of the specimen.

One can note that more resonance peaks are observed with the experimental superelement than with the numerical one, but this is not surprising. Indeed, with the numerical model, the studied node is perfectly centred on the beam tip. However, the accelerometer used for the experimental measurements is centred on the beam tip but is rather coarse. Its position is therefore not accurate. And since it is placed at the end of this thin beam, the transverse effects are important. Another sensor such that a laser could have been used for more precision. Nevertheless, the modes identified with both methods have more or less the same amplitudes and natural frequencies which is reassuring.

Moreover, it can be seen that the simulated curves obtained with the experimental superelement differ quite significantly from the ones measured with the sine sweep excitation. In fact it is not astonishing. Indeed, the two excitation processes are really different. One is done with hammer impacts while the other is a base-excitation done with a shaker. The structure is more damped with the base-excitation so this could explain why more peaks are identified with the experimental superelement. However, one can notice that some peaks are the same but with some errors on the natural frequencies.

To conclude, it can be said that the method is not completely validated and some research still needs to be done about this FBS method. For example, the interface and the coupling conditions could be improved.

4.3 120-kN shaker: head expander case

When large structures must be tested on an electrodynamic shaker, it is common to mount an expander on its table. The surface on which the structures to be tested may be installed is then much larger. In the case of the 120-kN DongLing shaker, it is interesting to use such a tool. However, this has a large mass. Indeed, for this specific shaker, it weighs 174 kg. It is therefore important to see if the dynamics of this expander have an influence on the dynamics of the shaker. One goal of this internship, expected by V2i, is to model this expander and its interaction with the electrodynamic shaker.

In this section, the CAD model of the expander is built. An experimental modal analysis is then performed to obtain the experimental modes. The FE model of the expander is updated until the correlation between experimental and numerical modes is satisfying. Thereafter, this model is coupled to the shaker model and the dynamics of the shaker/expander assembly is simulated. Finally, these simulations are validated thanks to an experimental test campaign.

4.3.1 Model of the head expander

The first step in this coupling process is to model the expander itself. The CAD model being not given by the shaker supplier, it must be here developed. This CAD model is shown in Figure 4.21 and is developed in *Siemens NX*. The mass that the software computes must correspond to the actual mass of the weighted expander.

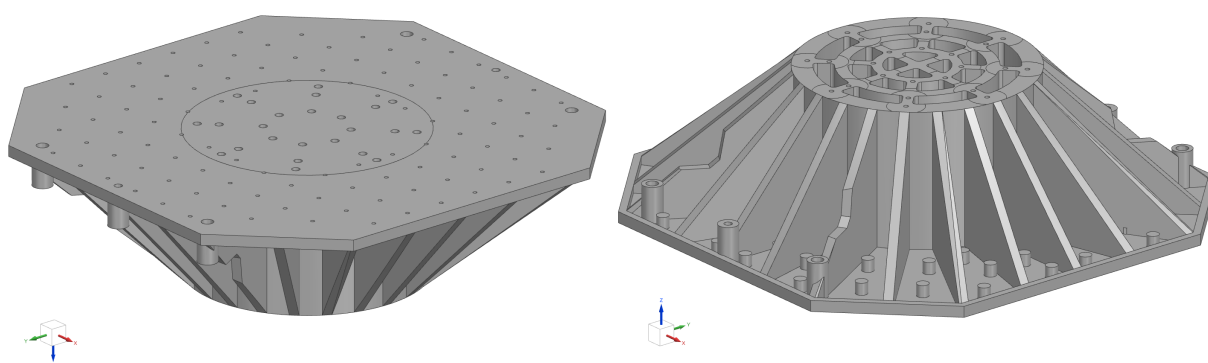


Figure 4.21: CAD of the expander.

The actual mass of the expander is 174 kg. It is made of an alloy of magnesium and aluminium which has a density of 1.74 g/cm^3 . After assignment of the material, the computed weight in *NX* is more or less the same as the measured one: 173.8 kg. However, since the head expander is a cast metal part, its geometry is not perfect. All the screw

holes do not have the same size, the solid is not perfectly symmetric, the density is not exactly known and probably not uniform. For these reasons, the CAD model cannot be perfect either.

The next step is then to mesh the solid. Tetrahedral mesh elements of degree one are chosen. It means that each element is made of four nodes. To assess the validity of the meshing, a convergence study is carried out: the five first natural frequencies of the expander are computed for different mesh sizes. The convergence of the frequencies may be observed in Figure 4.22. To realise this study, the bottom of the head expander is simply clamped.

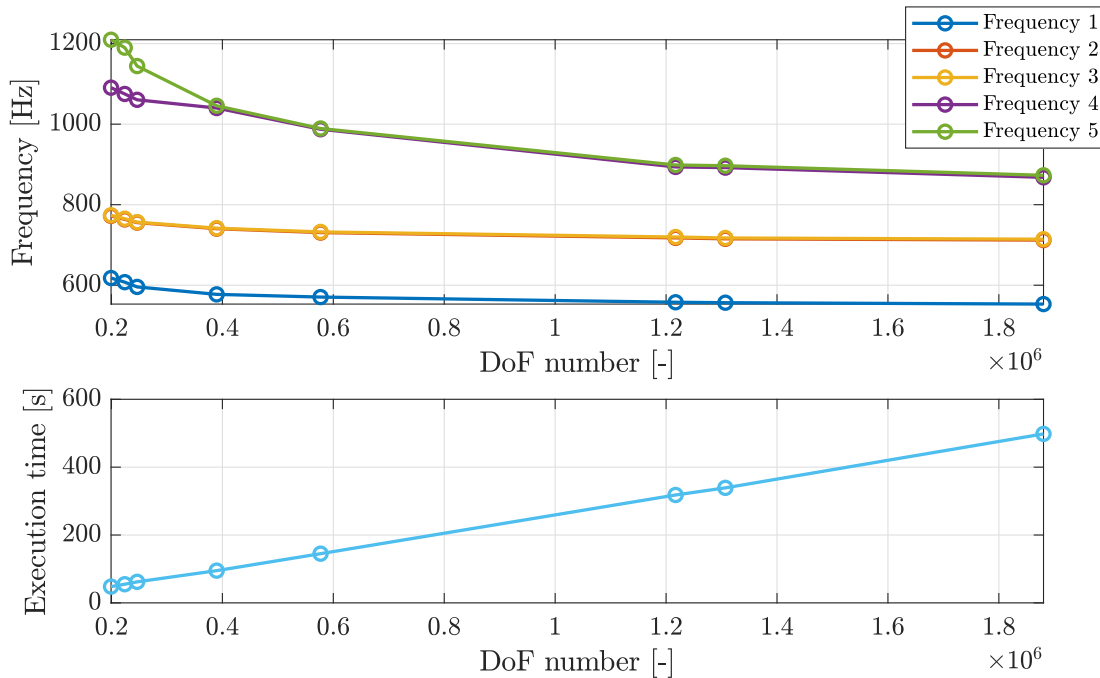


Figure 4.22: Convergence of the natural frequencies with the mesh size reduction.

The study is started with a mesh size of 50 mm (with a model made of 222 000 DoFs) and is refined down to 8 mm (1 880 000 DoFs). The mesh of 50 mm is really coarse but the smaller mesh takes a significant time to be executed (more than eight minutes). The ante-penultimate point in Figure 4.22 corresponds to a mesh size of 10 mm (1 200 000 DoFs). However, with this mesh, there is a large deformation energy around the screw holes of the expander. The mesh is still coarse around very small holes. The mesh size needs to be reduced to avoid this issue.

In order to refine the mesh where the stress is the highest without increasing too much the execution time, only a part of the expander can be refined. Indeed, there are small screw holes only at the center of the expander. Therefore, the FEM is only refined with a

mesh of 8 mm on a cylinder of 300 mm. It can be seen that at this point, the frequencies are already converged and that the computation time stays reasonable. For this specific mesh, there is 1 300 000 DoFs. Therefore, it is this meshing that will be used for the next computations.

One may notice in Figure 4.22 that the 4th and 5th frequencies are not completely converged with 1 300 000 DoFs. To get better results, the mesh should be more refined. However, the number of degrees of freedom is already really high as well as the execution time. Moreover, the three first frequencies are well converged so it is judged sufficient.

The mesh being validated, boundary conditions that would represent the reality more faithfully have to be set. Annular surfaces around each screw hole are then clamped to simulate the screwed connection between the expander and the shaker table. This is illustrated in Figure 4.23. The aim is to represent the contact surface between the table of the shaker and the bottom of the expander. To do so, it is common to project the washer face of the screw head on the interface with a cone having a half apex angle of 30° [34]. The surface of the bolt is also projected on the bottom surface of the expander. The surface of contact is finally defined by the intersection between the two projected surfaces as shown in Figure 4.24. Moreover, the surface of contact between the shaker table and the screw head is clamped too.

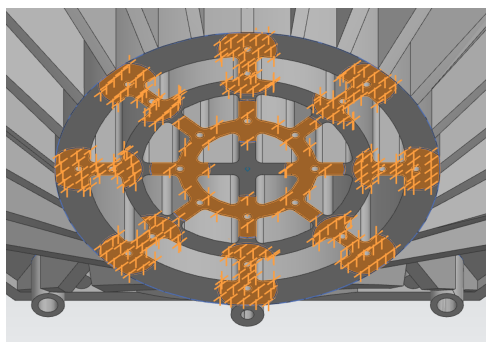


Figure 4.23: View of the interface at the bottom of the expander.

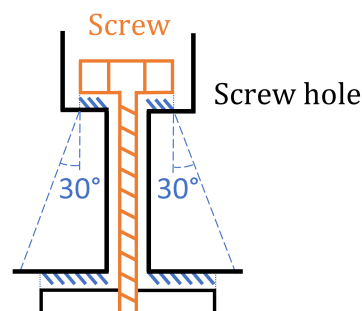


Figure 4.24: Clamping around the screw holes.

Thanks to this numerical model, the deformation of the mode shapes may be visualised in *Siemens NX*. These are used to determine the setup of the experimental tests. Indeed, they help to place the accelerometers on the table of the expander to catch as many modes as possible. Some of them may be observed in Figure 4.25. Only the global modes are displayed because these are the modes that are wanted to be represented by the model. The more localised modes are not interesting here.

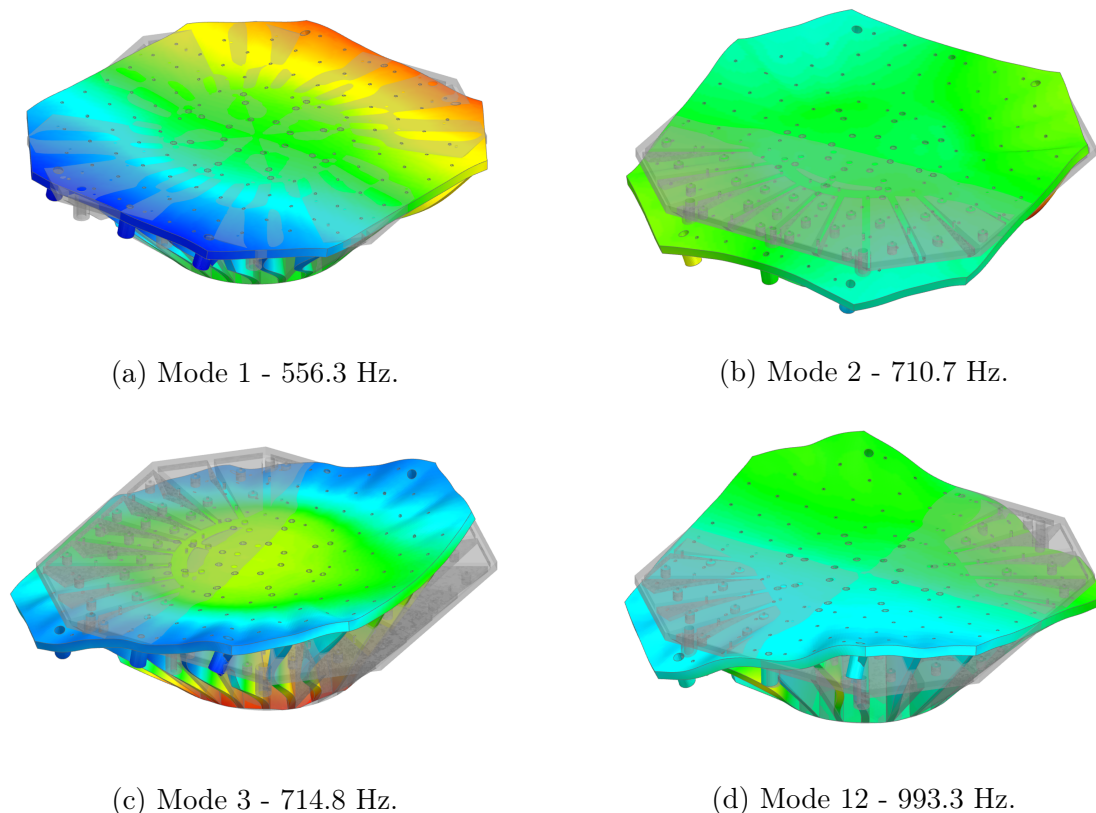


Figure 4.25: Numerical modes of the expander clamped at its base.

Thanks to these deformations it is concluded that it is necessary to measure the acceleration in the three directions since the expander deforms in the vertical direction but also in the table plane, as it is illustrated with the torsion mode in Figure 4.25a. Accelerometers must also be placed at least at each corner to catch the three other modes.

4.3.2 Experimental modal analysis: impact testing

An experimental modal analysis is performed in order to identify the experimental modes of the expander. The aim is to compare the numerical modes to them in order to validate the expander FEM.

This test campaign consists in exciting the head expander, fixed on the shaker table, in the three directions with a hammer. The hammer records the force of the impacts and the acceleration experienced by the structure is recorded through different accelerometers. The location of the accelerometers are determined with respect to the form of the modes computed by the numerical model. They are then placed in a cross pattern on the table of the shaker and one is placed at each corner. In addition, it is needed to refine this sensor grid to catch more localised modes. However, the more accelerometers there are,

the longer the test campaign takes. As the time available for testing on the shaker is very limited, it has been decided to refine only a quarter of the table. This configuration of impacts and measurement points may be observed in Figure 4.26.

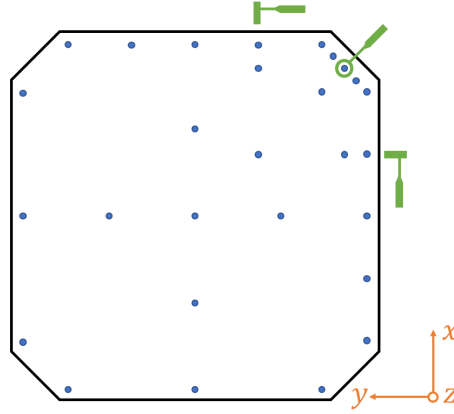


Figure 4.26: Setup of the impact testing on the expander: impact points (green) and measurement points (blue).

The acquisition is still performed thanks to *Siemens LMS testLab*. The FRFs of the acceleration over the force of the impact are provided by the software. There is thus a total of 756 acceleration-over-force measured FRFs: 28 measurement points, 3 directions measured since triaxial accelerometers are used, and 3 excitation points done to excite the three directions.

One can note that the structure is damped a lot and the force provided by the hammer is limited, so it is necessary to use very sensitive accelerometers. Therefore, accelerometers with 100 mV/g are chosen.

It is chosen to optimise the model in the [5 Hz - 1000 Hz] frequency range. However, the use of a single hammer does not allow to excite this whole frequency range. In fact, the excited frequency range depends on the stiffness of the hammer tip. The softer the tip, the more the low frequencies are excited, while the stiffer it is, the wider the excited frequency range is [20]. Therefore, two different hammers are used. One with a tip made of rubber to excite frequencies below 200 Hz and one tip made of vinyl to excite frequencies between 200 Hz and 1 000 Hz. It is illustrated in Figure 4.27 with the power spectral densities (PSD) measured during the impact testing. For the one obtained with the rubber hammer tip, the amplitude is high but only the low frequencies are excited. It is what is needed to excite the first modes. Indeed, the lower modes are global modes so they need a lot of energy to deform. In contrast, for the curve showing the PSD obtained with the vinyl tip, the amplitude is lower but it covers a much larger frequency range. In fact, modes at high frequency are often more localised modes so they need less energy

but the impact needs to be able to excite these high frequencies. This is why the stiffer tip made of vinyl is used in this case.

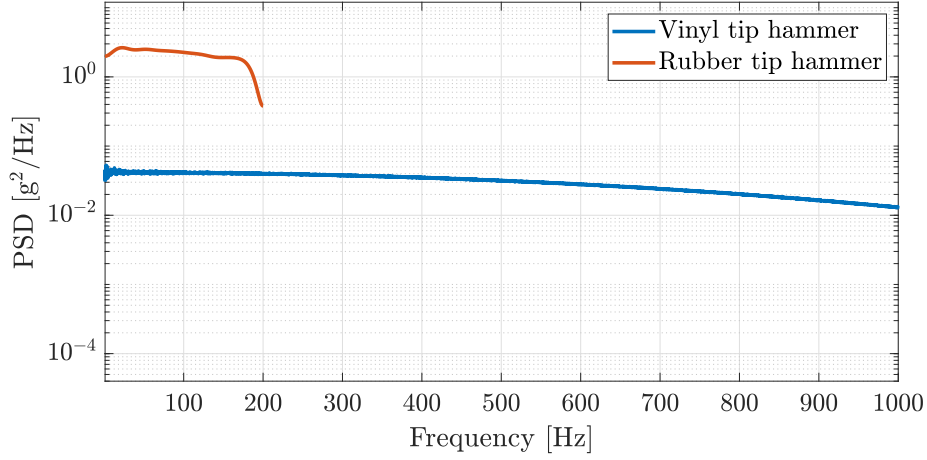


Figure 4.27: PSD from vinyl and rubber hammer impact.

The natural frequencies of the expander are then extracted thanks to the p-LSCE method: the poles are computed for different model orders and all the solutions are gathered on the stabilisation diagram. The one built with the vinyl hammer impact testing is shown in Figure 4.28.

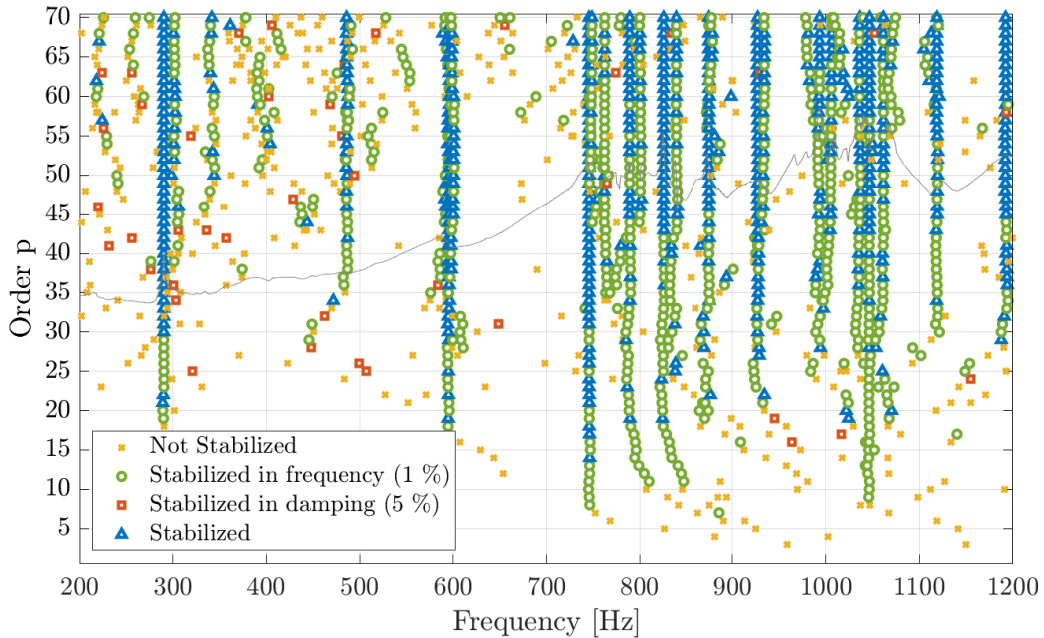


Figure 4.28: Stabilisation diagram (vinyl hammer). Classical p-LSCE method.

This diagram is drawn with the classical p-LSCE method presented in Section 4.1.1. These results are compared with the PolyMax method and the related stabilisation diagram is shown in the Appendix C, in Figure C.1. The natural frequencies are really

similar to the ones obtained with the p-LSCE method as it is observed in Table C.1.

As said earlier, if the alternative p-LSCE method is used, most of the spurious modes are removed. The stabilisation diagram shown in Figure 4.29 is indeed much clearer than with the classical p-LSCE method.

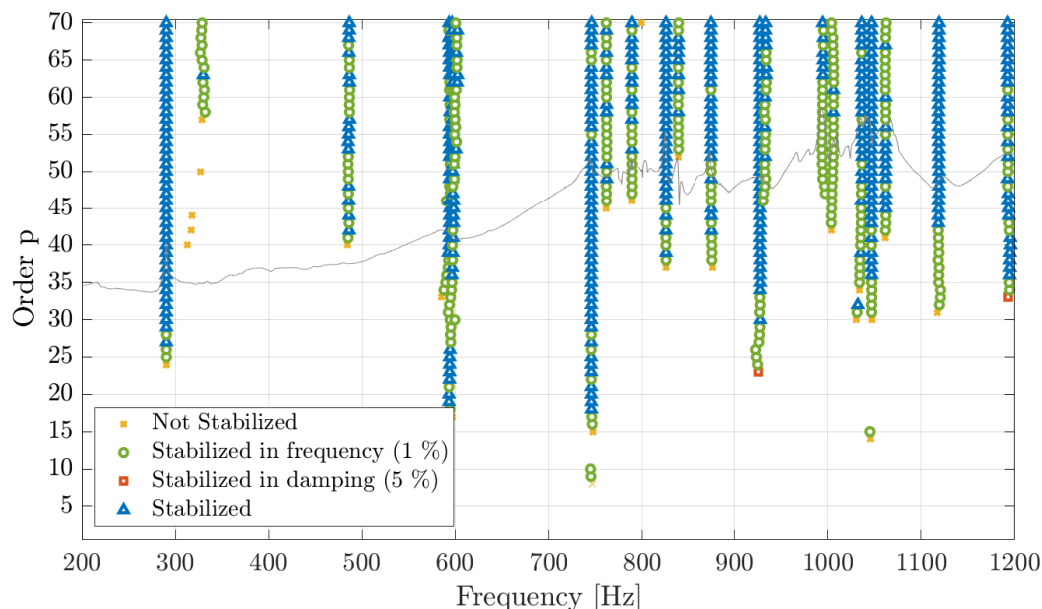


Figure 4.29: Stabilisation diagram (vinyl hammer). Alternative pLSCE method.

On this stabilisation diagram, columns of stabilised poles can be observed where poles appear at almost identical frequencies for several consecutive orders. It is chosen to consider here only the modes for which poles are stabilised over at least six consecutive orders. The higher natural frequencies of the structure are then identified. They are gathered in Table 4.1

	Frequency [Hz]	Damping coefficient [%]
Mode 1	290.23	0.19
Mode 2	598.3	2.05
Mode 3	744.4	0.26
Mode 4	825.7	0.13
Mode 5	874.9	0.21
Mode 6	927.4	0.81
Mode 7	997.1	0.23
Mode 8	1 046.8	0.16
Mode 9	1 118.47	0.81
Mode 10	1 197.1	0.55

Table 4.1: High natural frequencies of the head expander fixed on the table of the shaker obtained with the impact testing.

The same process is followed for the low frequencies, thanks to the rubber hammer impact testing. Six different modes are identified. Their frequencies and damping coefficients are gathered in Table 4.2. Unfortunately, even with a soft hammer tip, very few modes react at low frequency. The measured data are really not easy to process so the results can difficultly be trusted. One can note that the values of the damping coefficients in Table 4.2 are indeed abnormally high.

	Frequency [Hz]	Damping coefficient [%]
Mode 1	8.5	24.8
Mode 2	28.8	18.9
Mode 3	56.4	4.56
Mode 4	71.1	6.43
Mode 5	84.2	9.71
Mode 6	96.2	4.27

Table 4.2: Low natural frequencies of the head expander fixed on the table of the shaker obtained with the impact testing.

Thanks to the *LMS TestLab*, the corresponding mode shapes can be visualised. The author has chosen to focus only on easily identified modes. These will be plotted later. The retained modes at high frequency are modes 3, 4, 6, 7, and 10 (Table 4.1) and the retained modes in the low frequency set are modes 5 and 6 (Table 4.2)

The corresponding mode shapes can then be compared with the numerical ones. To do so, the Modal Assurance Criterion is used. It can be observed in Figure 4.30.

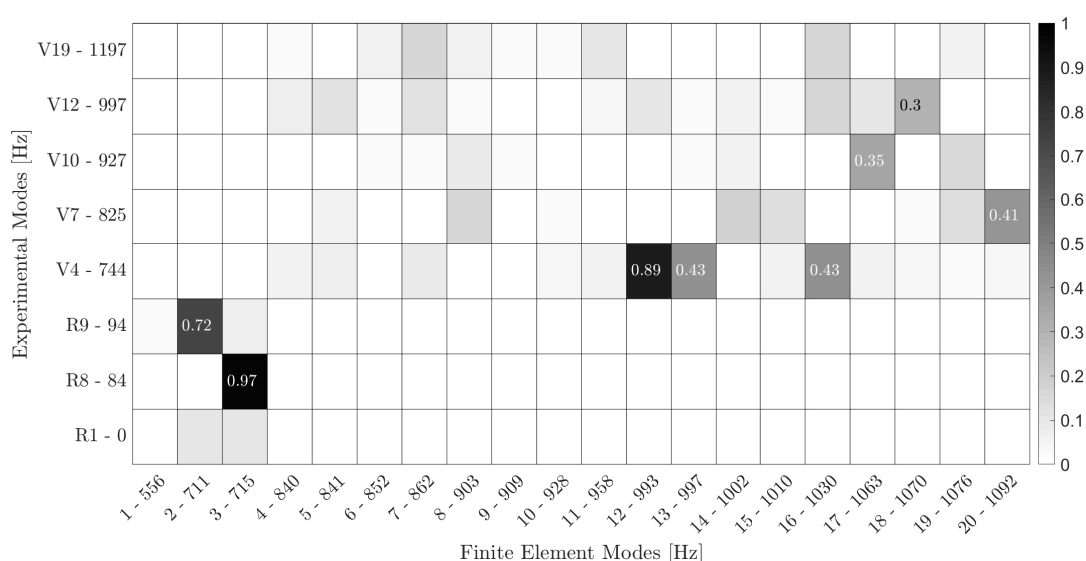


Figure 4.30: Modal assurance criterion of the modal analysis and the model of the expander when it is clamped at the screw holes.

The experimental modes obtained with the rubber hammer are denoted by a R and the ones obtained with the vinyl hammer are denoted by a V . One can see that the correlation is really poor since only two modes are above the 0.8 MAC limit.

To improve this correlation, the model needs to be updated. Indeed, these results are for the expander clamped at the estimated surfaces of contact. However, the impact testing of the expander having been done on the shaker, it is needed to imitate this situation. When the expander is fixed on the shaker, certain modes may result from the coupling between both parts. For example, tilting modes of the overall structure should appear. They can not be identified with the clamped expander.

4.3.3 Improvement of the model

At this time, the model of the expander is just clamped at the screw holes. To be closer to the reality, the shaker on which it is fixed must be modelled. To do so, the areas representing the screw holes considered as clamped previously, are now connected to a point (cf. Figure 4.31) to model the shaker table on which the expander is set.

Two kinds of connections are tried. The first one are rigid links between all the surfaces of contact previously clamped and the point representing the table. The second one is the "Mean interpolation" option in *Siemens NX*. With this type of connection, the surfaces are allowed to deform but the mean relative displacement of these surfaces is null. In fact, the reality is rather in between these two kinds of connection but is difficult to represent. However, the "Mean interpolation" option gives better results than the rigid links so it is the selected option. These results will be shown later on.

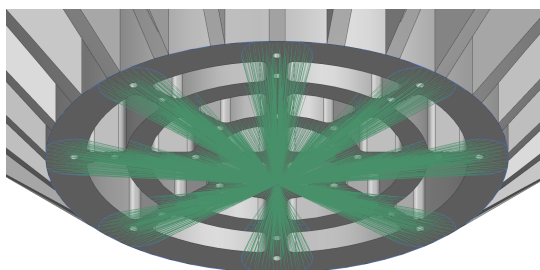


Figure 4.31: Rigid link between the expander and the shaker.

The motion of the attachment point is prevented in the horizontal plane; the displacements along x and y axes are blocked to represent the support flexures of the shaker table. The suspensions of the table connected to the shaker body are represented by a stiffness element. In addition to the stiffness acting along the z -direction, three rotational stiffnesses must be added here. They are essential to represent the overall tilting modes. The coil is represented by a point that can only move vertically as it is supposed to be

in reality. Its suspensions are also modelled by a stiffness element. This is illustrated in Figure 4.32.

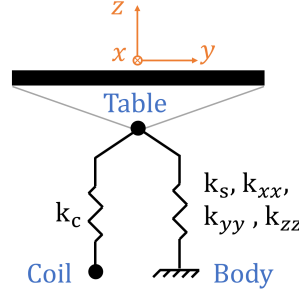


Figure 4.32: Scheme of the model of the shaker underneath the expander.

The values used in the model for the table and coil suspension stiffnesses (respectively k_s and k_c) are the ones computed in Table 3.7. However, the rotation stiffnesses, k_{xx} , k_{yy} and k_{zz} are not given by the parameter identification of Section 3.1 so they must be assessed. To do so, the formula of the natural frequencies of the torsion modes is used as shown in Equation. 4.26:

$$f = \sqrt{\frac{k_{II}}{I_{II}}} \quad (4.26)$$

$$\Leftrightarrow k_{II} = f^2 \times I_{II} \quad (4.27)$$

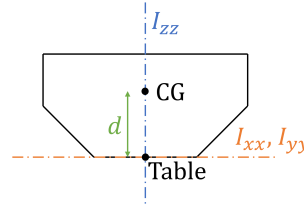


Figure 4.33: Inertia of the expander.

with $I = x, y$ or z and where I_{II} is the inertia in rotation about the point of fixation on the table. These are illustrated in Figure 4.33. The inertia about the centre of gravity (CG) is given by the CAD model in *Siemens NX*. The transport theorem is then used to compute the inertia around the point of interest.

The natural frequencies of the three modes of rotation are known experimentally. They will be displayed later but it comes that the rotation mode around y -axis, so the first tilting mode, appears at 85 Hz. The second tilting mode, around the x -axis, appears at 94 Hz. Finally, the torsion mode around z -axis appears at 1196 Hz. These computed stiffnesses are then gathered in Table 4.3:

	Stiffness [kg.m ²]
Rotation around x -axis	4.48×10^3
Rotation around y -axis	3.58×10^3
Rotation around z -axis	7.33×10^5

Table 4.3: Stiffnesses in rotation for the numerical model built in Siemens NX.

One can note that the torsional stiffness around the z -axis is much larger than in the other directions. It is due to the fact that the support flexure shown in Figure 2.2 is flexible in the vertical direction. In this way, the coil can move in the vertical direction but not so much in the plane since it is very stiff in this direction. They cannot be twisted. This explains why the first torsion mode is so high in frequency.

4.3.4 Comparison of numerical and experimental modes and frequencies after model update

After modification of the model, the mode shapes can again be compared thanks to the Modal Assurance Criterion. The MAC coefficients can be observed in Figure 4.34.

As said in Section 4.1.1, only the numerical modes having a sufficient effective mass are plotted on the MAC graph. Only the modes having an effective mass higher than 5% are studied. However, there is an exception for perfect symmetric modes for which all the effective masses are equal to 0%. Their deformations will be plotted later and it will be seen that these modes respond a lot so are still interesting. In fact, since these modes are symmetric, the contributions of the symmetric parts cancel each other and so the reaction to the shaker is null.

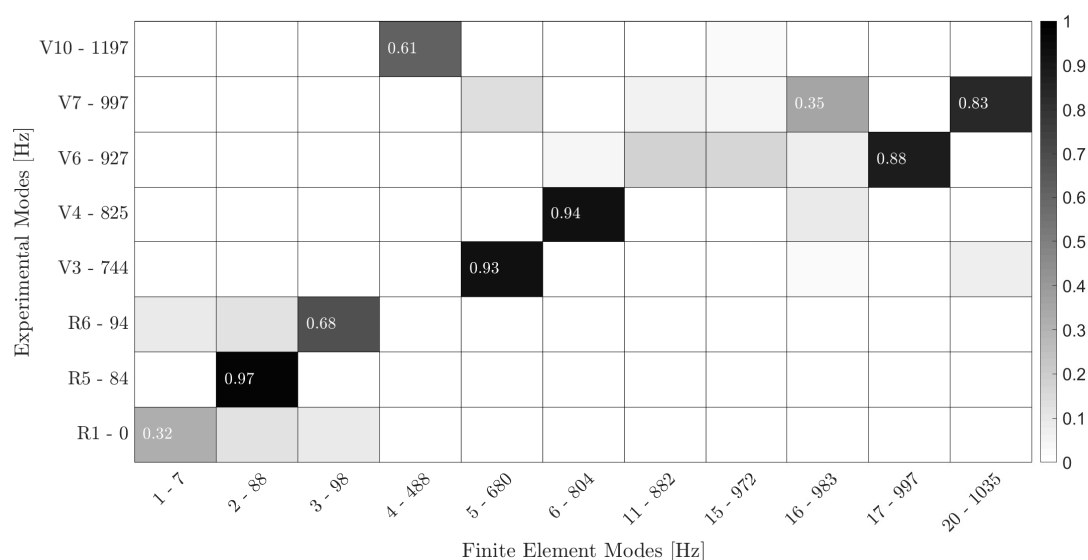


Figure 4.34: Modal assurance criterion of the modal analysis and the model of the expander when it is fixed on the shaker.

It can be seen that there is a tendency of correlated modes on the diagonal of the grid, which was wanted. The MAC coefficients are much better than in the case of a clamped expander. Five modes have a MAC coefficient above the 0.8 limit.

However, some modes of the diagonal have a MAC coefficient lower than 80%, but will be analysed anyway. Indeed, one has to note the difficulty of the structure to be modelled. The piece is not perfectly symmetric, it has a lot of defaults. For example, the stringers never have exactly the same thickness, the thickness of the table is not uniform, surfaces are not perfectly flat, etc. It is not a piece produced in series, it is a unique foundry piece sold with the shaker so it is not precisely manufactured.

The natural frequencies related to these modes are gathered in Table 4.4 and the relative error computed with respect to the experimental natural frequencies is obtained as shown in Equation 4.28:

$$\varepsilon_f = \frac{f_{\text{exp}} - f_{\text{num}}}{f_{\text{exp}}}, \quad (4.28)$$

and can be observed in the Table 4.4.

Frequency LSCE [Hz]		Frequency FEM [Hz]		Error ε_f [%]
Mode R5	84.2	Mode 2	88	-4.5
Mode R6	96.5	Mode 3	98	-1.6
Mode V3	744.4	Mode 5	680	-8.6
Mode V4	825.7	Mode 6	804	2.6
Mode V6	927.4	Mode 17	997	7.5
Mode V7	997.1	Mode 20	1 035	3.8
Mode V10	1 197	Mode 4	488	59.23

Table 4.4: Comparison of the natural frequencies of the head expander fixed on the table of the shaker obtained with the impact testing and with the FEM model.

It is observed that there are still some important errors on the natural frequencies. This probably results from the simplicity of the shaker model. Indeed, the table of the shaker is assumed to be rigid in the model. To get better results, it would have been needed to realise a CAD model of the table then to couple it to the coil of the shaker. However, the coil of this shaker is not easily accessible and it is impossible to perform measurements on it. Therefore, this was not realistic in the scope of this work.

To better understand these results, the identified modes can be analysed. From the modal analysis, several modes are exploitable. They can be visualised and compared to the numerical mode shapes in the following figures.

The two first modes are captured with the rubber tip hammer. The first mode is a tilting mode around the y -axis (Figure 4.35). The second mode is more or less the same but about the x -axis (Figure 4.36).

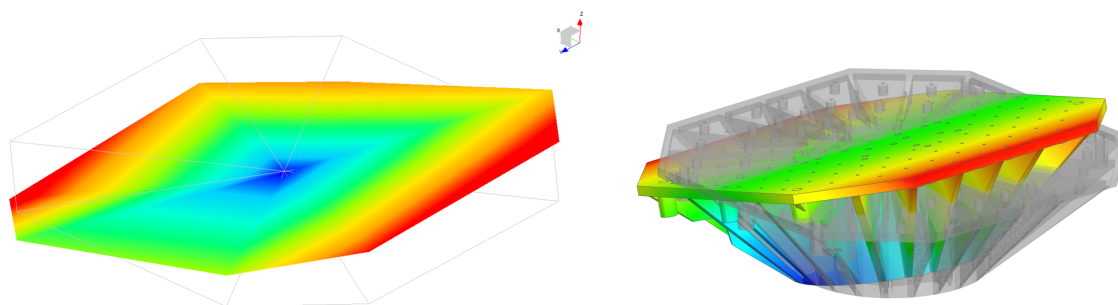


Figure 4.35: Experimental mode at 84 Hz (left), numerical mode at 88 Hz (right).

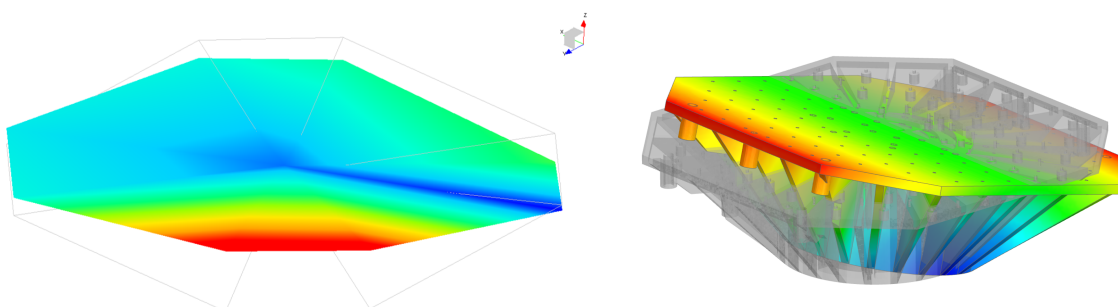


Figure 4.36: Experimental mode at 94 Hz (left), numerical mode at 98 Hz (right).

The following modes are caught with the vinyl tip hammer since they appear at higher frequencies. The third mode is already more complex. It is chosen to call it the first butterfly mode because of its shape (Figure 4.37): two corners have positive vertical deflection while the two other corners have a negative vertical deflection. The fourth mode is the second butterfly mode: two opposite sides have positive vertical deflection while the two others have negative vertical deflection (Figure 4.38). These two modes are each symmetric, which means that their effective masses are equal to zero.

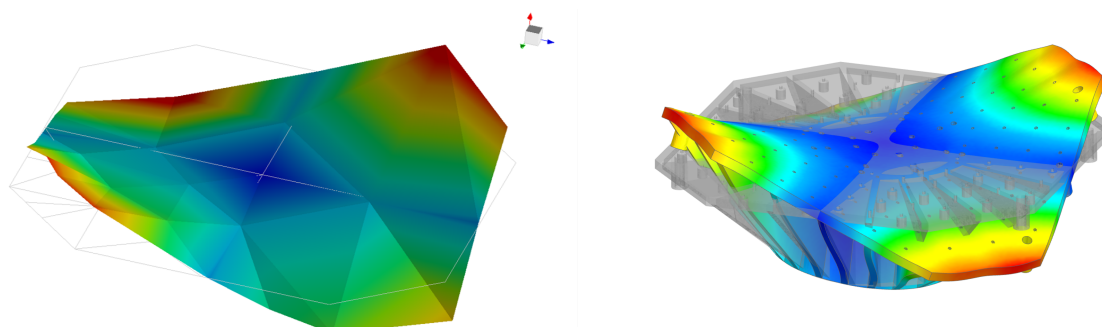


Figure 4.37: Experimental mode at 744 Hz (left), numerical mode at 680 Hz (right).

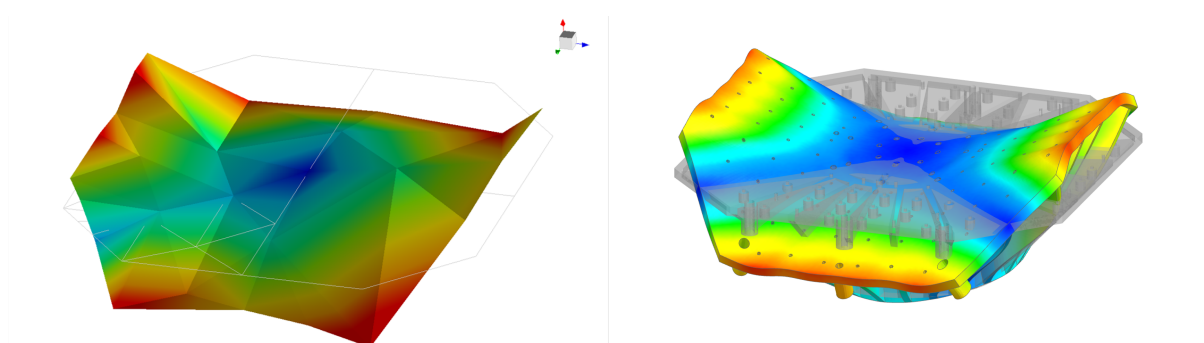


Figure 4.38: Experimental mode at 825 Hz (left), numerical mode at 804 Hz (right).

The fifth and sixth modes are more localised modes; the corners of the expander are mainly deformed as well as the stringers below the table of the expander (Figures 4.39 and 4.40).

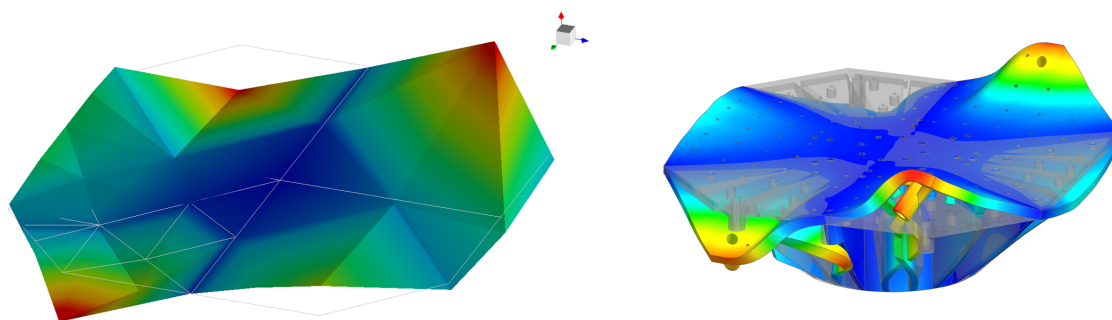


Figure 4.39: Experimental mode at 927 Hz (left), numerical mode at 997 Hz (right).

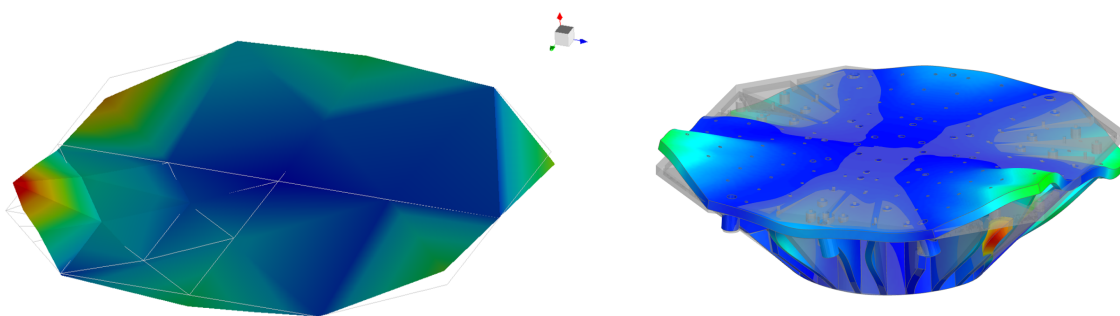


Figure 4.40: Experimental mode at 997 Hz (left), numerical mode at 1 035 Hz (right).

The last experimental mode is a torsion mode and is observed in Figure 4.41. It is identified at 1 197 Hz while the numerical torsion mode already appears at 488 Hz. This large difference could already be noticed with the corresponding large error computed in Table 4.4.

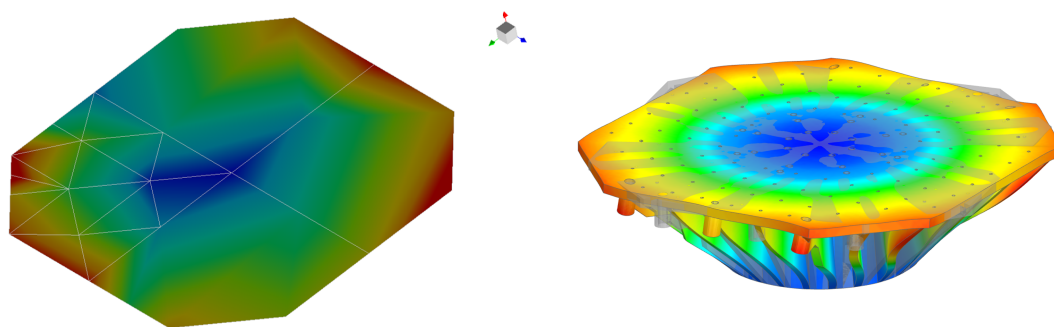


Figure 4.41: Experimental mode at 1997 Hz (left), numerical mode at 488 Hz (right).

4.3.5 Validation of the model

The ultimate goal of this chapter is to show the final results of the virtual shaker testing. To do so, the numerical superelement of the shaker is introduced in *Simulink* in order to couple it to the shaker model. As it has been done to validate the shaker model, the *Simulink* simulations results obtained with *Simulink* are compared with a test campaign.

The idea of this test campaign is to obtain measured FRFs to compare them to the simulated ones. The current, the acceleration and the voltage are recorded so that the acceleration-over-current and acceleration-over-voltage FRFs are plotted. To do so, a sine sweep excitation is therefore applied to the expander. The latter is screwed on the table of the shaker. An accelerometer is placed on the table of the shaker, below the expander, to understand its behaviour when such a mass is fixed on it. Three accelerometers are placed on top of the table: one at the centre, one at the right of the expander table and one at its front. One accelerometer is placed on one side of the table as it is shown in Figure 4.42.

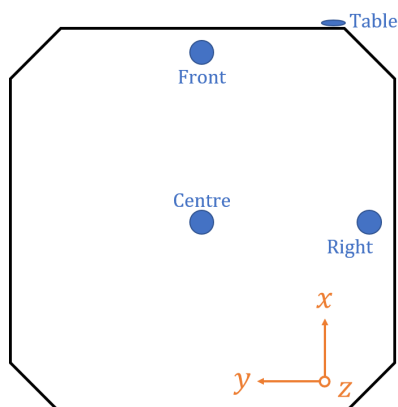


Figure 4.42: Location pattern of the accelerometers (blue dots) on the expander.

The sine frequency is, this time, only varied between 5 Hz and 1 000 Hz. The input signal is defined in the same way as for the first test campaign done in Chapter 3: a

preliminary first closed loop system allows to define the limit of the maximum input voltage. However, in order to avoid measuring noisy signals at low frequency, once again, the drive signal is defined larger than the limit at low frequency and is progressively decreased so that the limit is respected at high frequencies. The drive signal has therefore the shape illustrated in Figure 4.43.

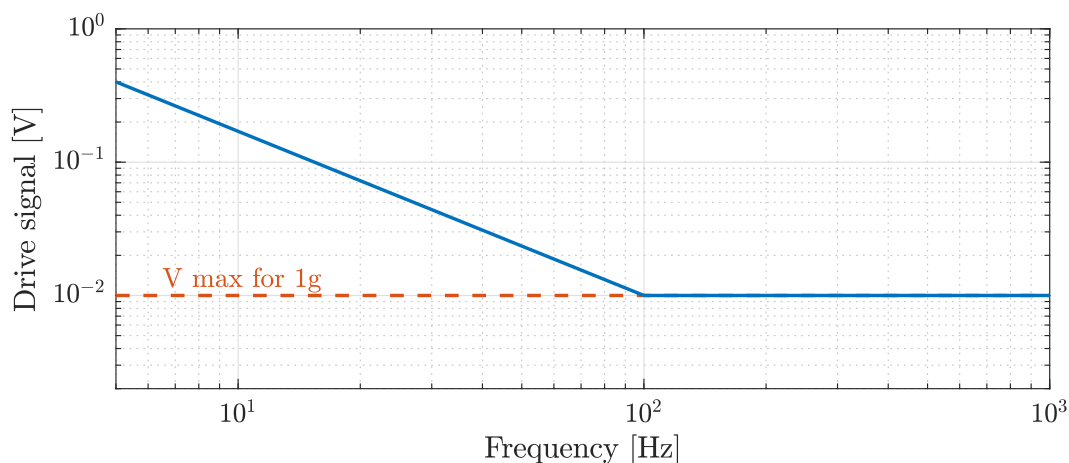


Figure 4.43: Shape of the driving signal.

The acquisition is still performed through *LMS*. The considered acquisition parameters are shown in Table 4.5. The measured FRFs are finally obtained.

Parameters	Value
Input type	Sine sweep
Input voltage	0.01 V
Bandwidth	10 000 Hz
Frequency sample	25 600 Hz

Table 4.5: Acquisition parameters for a test on the 120-kN shaker with the expander.

To obtain the simulated curves, the superelement is done in *Siemens NX*. The point that models the table of the shaker as it was illustrated in Figure 4.32 is now the retained node of the superelement. Only the vertical translation DoF is retained and the five other DoFs are blocked. Four nodes are included in the superelement: the same as the accelerometer locations shown in Figure 4.42. In this perspective, the acceleration measured at these points may be synthesised with the virtual shaker testing.

The mode shapes, their natural frequencies and the superelement matrices of Equation 4.14 and 4.17 are computed with Samcef. The latter are introduced in the *Simulink* model. The superelement of the expander is thus coupled to the numerical model of the shaker. The measured and simulated FRFs are finally compared. The acceleration-over-

current FRFs (resp. acceleration-over-voltage FRFs) related to the accelerometer at the right side of the expander table are shown in Figure 4.44a (resp. in Figure 4.44b).

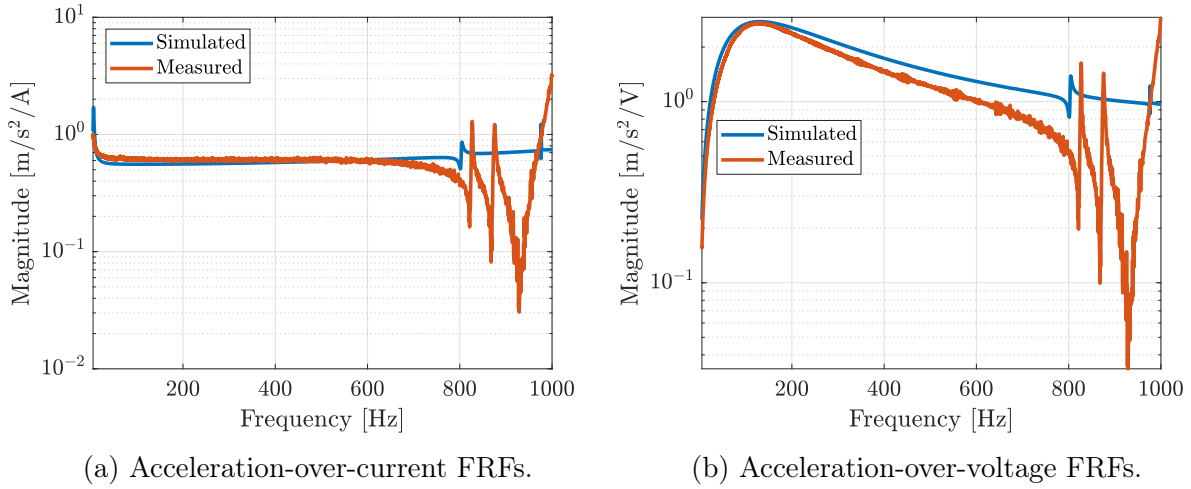


Figure 4.44: Expander fixed on the shaker, acceleration measured on the centre of the expander table: comparison between measured and simulated FRFs.

It can be seen that the curves do not exactly match but these results are not surprising. Indeed, in the model, the node related to the *Centre* accelerometer is exactly located at the centre the structure. However, in reality, the accelerometer is not exactly fixed at the centre of the table. Moreover, the expander is not perfectly symmetric and there is probably a small eccentricity off the axis of the shaker. This explains why such peaks appear in the measured curves while the simulated curves are so unresponsive.

The acceleration-over-current (resp. acceleration-over-voltage) FRFs related to the *Right* accelerometer are shown in Figure 4.45a (resp. Figure 4.45b).

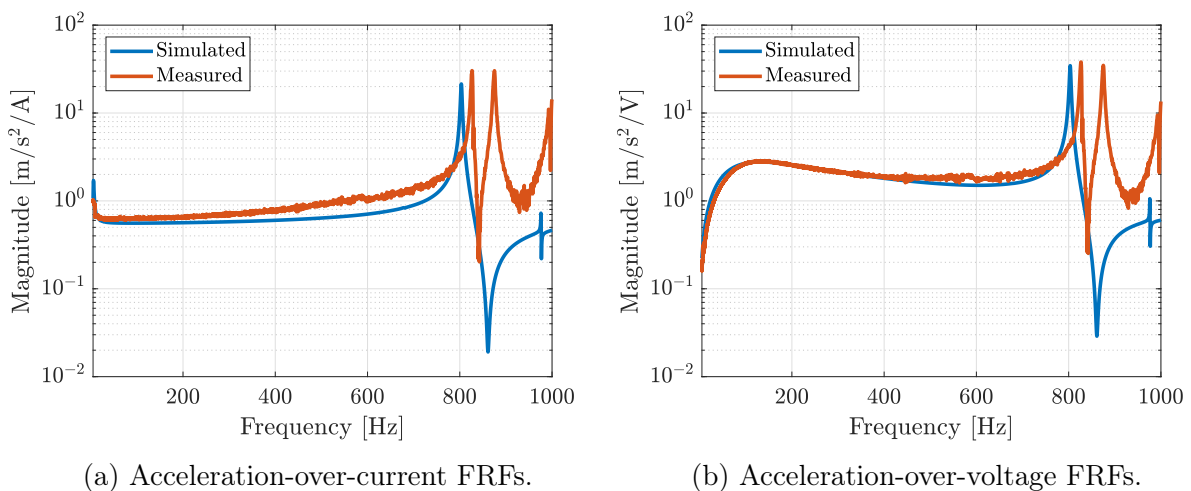


Figure 4.45: Expander fixed on the shaker, acceleration measured on an extremity of the expander table: comparison between measured and simulated FRFs.

One can note that the curves are not superposed as expected. This can be explained by the simplicity of the model while the studied system is very complex. To obtain better results, as said previously, the table of the shaker should be modelled more accurately by a CAD model and coupled to the rest of the shaker with a superelement. This could be done in future works.

Nevertheless, these figures show interesting results. Indeed, even if the peaks of resonance are not perfectly identified, it indicates that the expander/shaker assembly reacts in a specific range of frequency. The virtual shaker testing allows then to predict that some resonance phenomena are expected above 600 Hz. Moreover, the amplitude of the peaks is well represented.

4.3.6 Addition of the load support guidance

Since the expander is a heavy mass added on the shaker, some guides are needed to limit the torque applied on the armature, i.e., on the coil and the shaker table. Load support guidance allows payload to be safely mounted on the shaker, and reduces the risk of damage on the shaker suspension system even if the centre of mass is not aligned with the shaker axis. This support is made of four linear ball bearings. Two of them can be observed in Figure 4.46: these are the cylindrical pieces of metal. They prevent cross-axial motion or rotation of the upper surface of the expander, and they ensure that the movement is as purely vertical as possible. The load supports are also made of two load isolation supports that are inflatable suspensions that limit the weight that the expander applies onto the shaker coil. One of them is shown in the Figure 4.46, it is the cushion-shaped part located between the linear bearings.



Figure 4.46: Load support guidance of the expander on the 120-kN shaker.

In fact, in this DongLing shaker, the coil motion is only constrained in its bottom by some racks but it is less constrained in its upper part. Indeed, the top of the coil is only guided by the support flexure (cf. Figure 2.2). As a matter of fact, if the specimen is slightly off-centre, which is always the case in the real life, the shaker does not vibrate along its vertical axis only but also in the other directions. As a consequence, no specimen can be tested on the expander without the load support guidance.

Test campaign on the shaker

This load support has to be modelled to be part of the virtual shaker testing. However, it is very difficult to build a finite element model for these complex systems. Therefore, experimental tests need to be carried out to understand the role they play in the structure. In order to integrate them efficiently in the global shaker model, they have to be modelled in the simplest way as possible. To know the influence that the expander load support has on the system, the same sine sweep excitation as without the load support is applied again on the expander. The acceleration-over-current and acceleration-over-voltage FRFs with the load support can then be computed and compared to the no load support case. To do so, accelerometers are placed as shown in Figure 4.47 and, as previously, the voltage and the current are recorded during the sine sweep excitation.

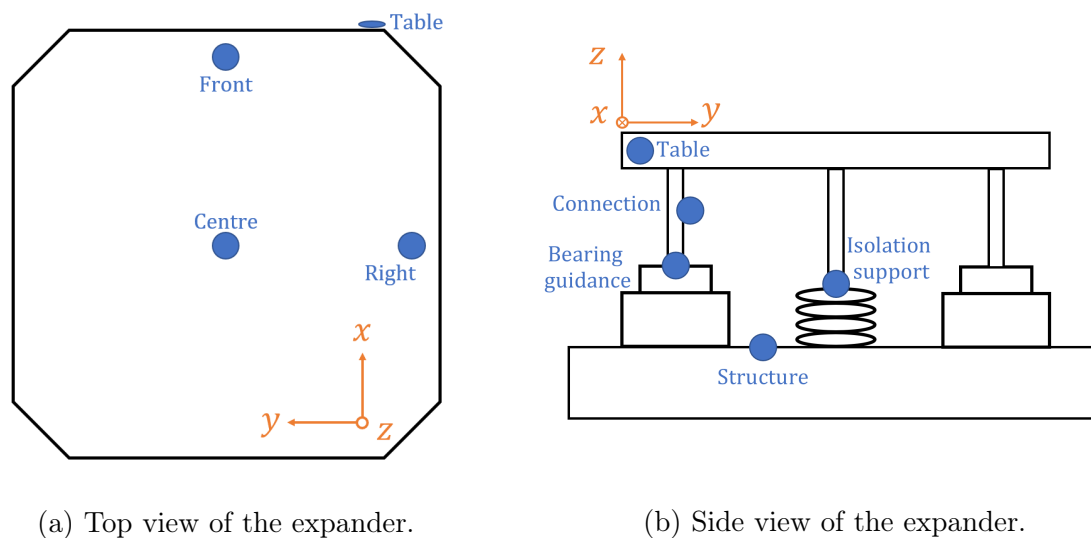


Figure 4.47: Location pattern of the accelerometers (blue dots) on the expander and its load support guidance.

The same acquisition parameters as without the support guidance are kept. These have been summarised in Table 4.5. To compare the behaviour of the expander with and without these supports, their respective FRFs are superposed. The acceleration-over-current and acceleration-over-voltage FRFs are respectively shown in Figure 4.48 and

4.49. The acceleration measurement used to plot these is the vertical acceleration at the centre of the table of the expander.

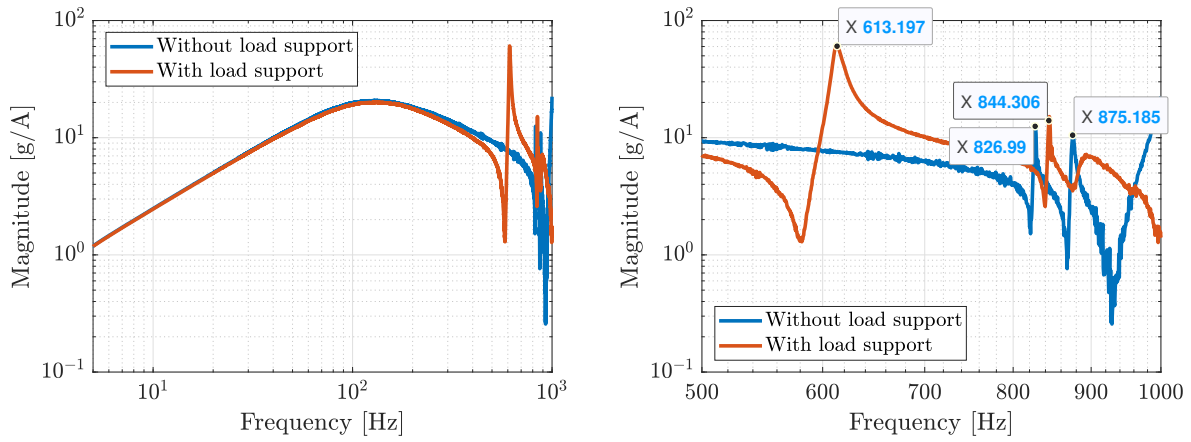


Figure 4.48: Comparison of the acceleration-over-current frequency response functions with and without load support guidance. Measurements done on the 120-kN DongLing shaker with a sine sweep in the [5 Hz - 1 000 Hz] frequency range.

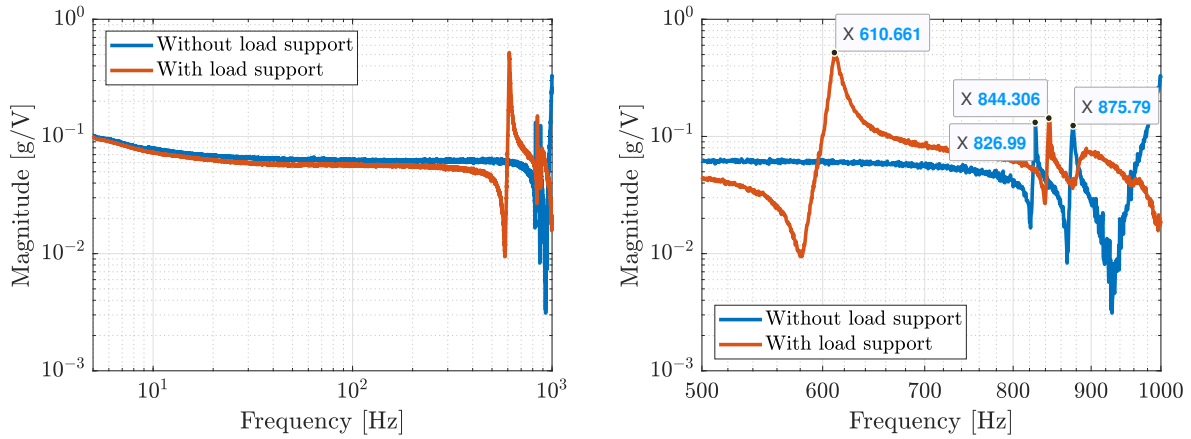


Figure 4.49: Comparison of the acceleration-over-voltage frequency response functions with and without load support guidance. Measurements done on the 120-kN DongLing shaker with a sine sweep [5 Hz - 1 000 Hz] frequency range.

It can be observed in these two cases that, when the load support guidance is present, the peaks of resonance appear at different frequencies, there are additional peaks.

To understand if these supports stiffen the structure or if they just guide the motion and act as sliders, the acceleration signal of the accelerometers placed on these supports is analysed. The sensors of interest are those named *Connection* and *Isolation support* in Figure 4.47b. It can be seen in Figure 4.50 that different peaks of resonance appear.

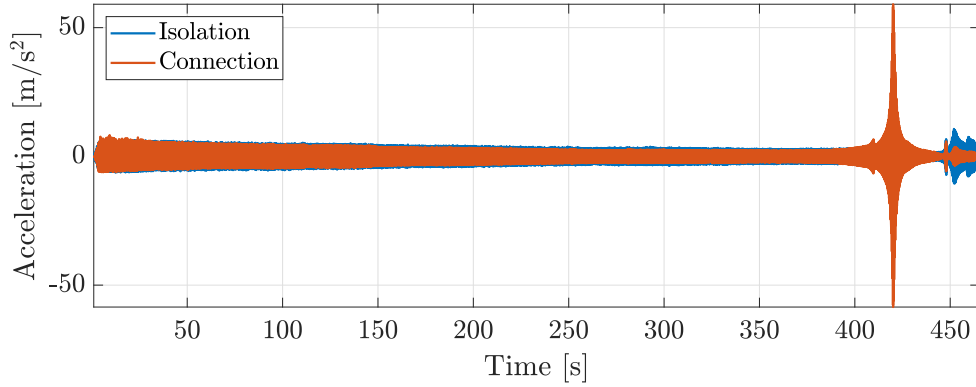


Figure 4.50: Acceleration evolution of the load support.

To understand the behaviour of the load support, it is common to draw the stiffness diagrams [35]. It plots the acceleration $\ddot{x}(t)$ as a function of the displacement $x(t)$. To obtain the displacement from the acceleration measured during the experimental test, signals are simply integrated over time.

These accelerations can be analysed at two different times: when the response is stationary and when the largest peak appears so around 420 s. In the stationary region, it is chosen to look at the response at 300 s because the transient responses is over and there is no peak there. These two extreme configurations are both shown for each of the two studied accelerometers. The two plots related to the *Isolation support* accelerometer are shown in Figure 4.51a while the ones related to the *Connection* accelerometer are shown in Figure 4.51b.

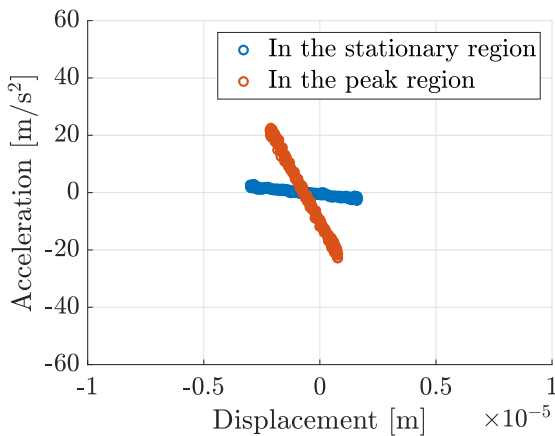
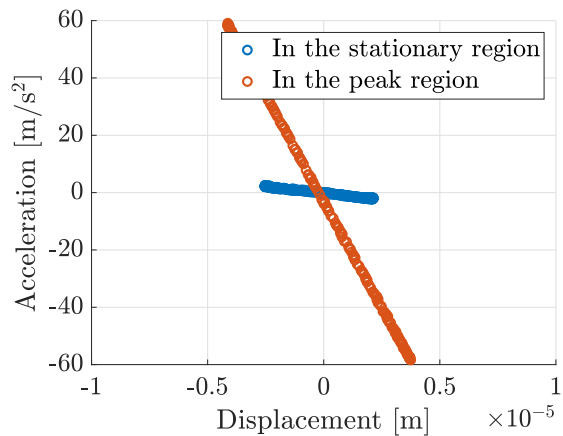

 (a) *Isolation support* accelerometer.

 (b) *Connection* accelerometer.

Figure 4.51: Stiffness diagrams displayed at two different times: in the stationary region and in the peak region of the response.

Figures 4.51 shows that in the stationary region, when no mode reacts, the slope of

the stiffness plot is much smaller than in the peak region. This means thus that when the supports are not solicited, they only act as simple guides. There is only a sliding motion since there is almost no stiffness. However, in the peak region, the slope of the stiffness diagram is increased. It means that the stiffness of the supports is increased. In fact, when the mode reacts, the corner of the expander deforms and the linear ball bearings work in bending. This is not what they are done for so their stiffness is increased. To conclude, this proves that the stiffness of the bearings is increased when there are peaks of resonance.

Numerical model of the expander with its load support and comparison with the experimental modal analysis

It has been shown in the previous section that modelling the loading supports by sliders only is not sufficient. Therefore, some stiffnesses need to be added in the expander model to correctly compute the different mode shapes of the structure.

To model the expander with its load support fixed on the shaker, the stiffnesses that had been placed under the expander to model it in a first time are kept. As a reminder, the suspension of the coil was modelled by a stiffness acting in the vertical direction and the suspension of the table by a stiffness in the vertical direction too but also in the three axes of rotation. It was illustrated in Figure 4.32.

To model the load support of the expander in the FEM, some stiffnesses are added. The linear ball bearings vertically guide the expander so the resistance along the vertical axis is very low and the stiffnesses acting in the plane and along the rotation axes are really high. In the following, the stiffnesses related to these bearing guides will be denoted by k_g . The two load isolation supports seem to be mainly used to sustain the mass of the expander and so it can be modelled by a stiffness along the vertical axes. However, it slightly prevents the torsion and the rotations so stiffnesses in the other directions can also be added. These stiffnesses will be denoted by k_i .

Therefore, there are twelve stiffnesses parameters (six for the bearings and six for the isolation supports) to introduce in the FEM. These parameters must be identified. By lack of time, they have only been determined manually. Their values are manually adjusted until the correlation between experimental and numerical results is acceptable. Therefore, an experimental modal analysis is needed to identify the experimental modes and their natural frequencies. The numerical ones obtained with NX can then be compared to these experimental results.

An impact testing on the expander with its loading support has already been done a few years ago in V2i. Its results are used here to determine the natural frequencies and the mode shapes of the structure. The acceleration had been measured in the three directions with 45 measurement points. Moreover, impacts have been done in two directions: in the vertical axis, and in the plane of the expander table as it is illustrated in Figure 4.52.

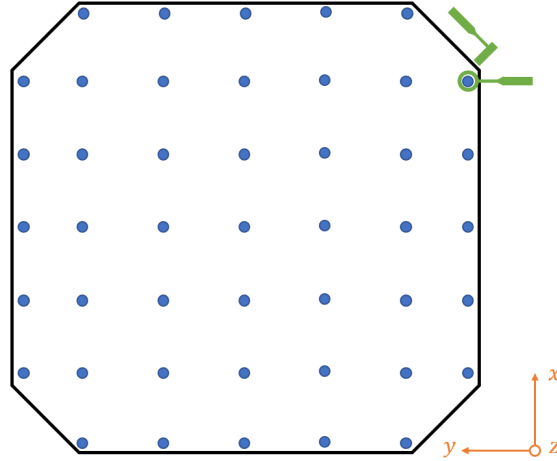


Figure 4.52: Location pattern of the accelerometers (blue disks) on the expander.

The natural frequencies and the damping coefficients are then extracted thanks to the p-LSCE method and the eigenmodes are obtained with the LSCF method. These experimental results are used to optimise the numerical model of the load supports by adjusting the stiffness parameters. Different values are tested and the ones that give the better correlation between analytical and experimental modal results are kept. To evaluate this correlation, the difference between the natural frequencies is computed and the MAC is evaluated. These stiffness values are gathered in Table 4.6:

	Translation [N/m]	Rotation [Nm/rad]
k_{gx}	10 000	10 000
k_{gy}	10 000	10 000
k_{gz}	10	10
k_{ix}	10	10
k_{iy}	10	10
k_{iz}	10 000	10

Table 4.6: Stiffnesses in rotation for the numerical model built in Siemens NX.

The MAC coefficients computed between the experimental modes and the final numerical modes obtained with these values are illustrated in Figure 4.53. Only the seven first modes are here considered.

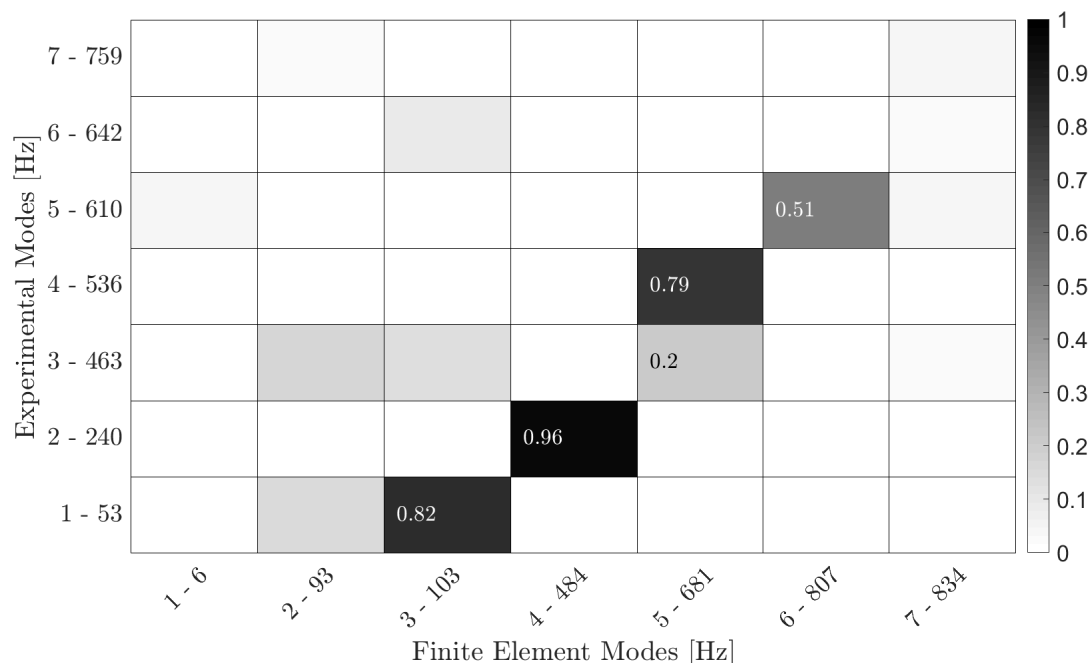


Figure 4.53: MAC between the modal experimental analysis and the model for the expander with its load supports.

It can be seen that the correlation is still rather poor. Indeed, only two poles have a MAC coefficient higher than 80%. Nevertheless, a diagonal of correlations higher than the others is observed. Only the most correlated modes are analysed: the experimental modes 1, 2, 4 and 5 and the numerical modes 3 to 6. The error between these natural frequencies can then be calculated. These are gathered in Table 4.7.

LSCE frequency [Hz]		FEM frequency [Hz]		Error ε_f [%]
Mode 1	53.38	Mode 3	103.26	-93.44
Mode 2	239.86	Mode 4	483.69	-101.66
Mode 4	535.71	Mode 5	680.92	-27.21
Mode 5	610.16	Mode 6	806.74	-27.22

Table 4.7: Natural frequencies of the head expander fixed on the table of the shaker obtained with the impact testing.

The natural frequencies obtained numerically are largely over-estimated. Many different stiffness values have been tried but none of them has given better results than those shown in Table 4.7. To get better results, an identification method should have been developed to determine these stiffness values. However, in this work, only one model update iteration has been performed so results are not satisfying. A more advanced study could be done in a future work.

Nevertheless, the deformation of these modes can finally be observed. Even if there exists a large gap between estimated and measured frequencies, the shape of the modes is well approximated. The first identified mode is a tilting mode. The second one is a torsion mode. The third one is the first butterfly mode and the fourth one is the second butterfly mode.

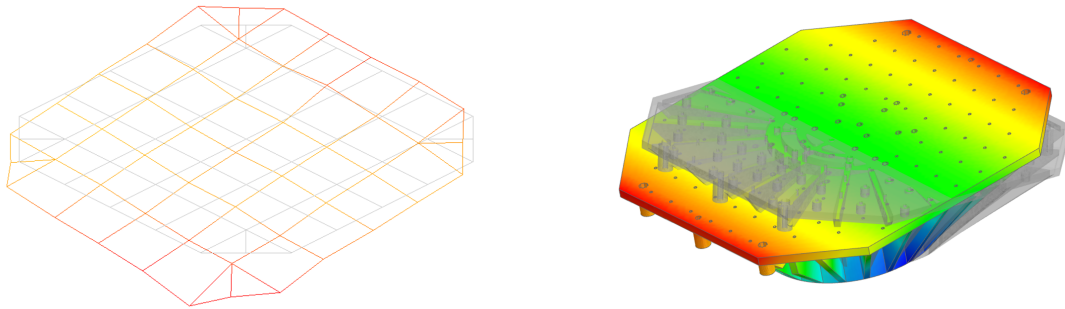


Figure 4.54: Experimental mode at 53 Hz (left), numerical mode at 103 Hz (right).

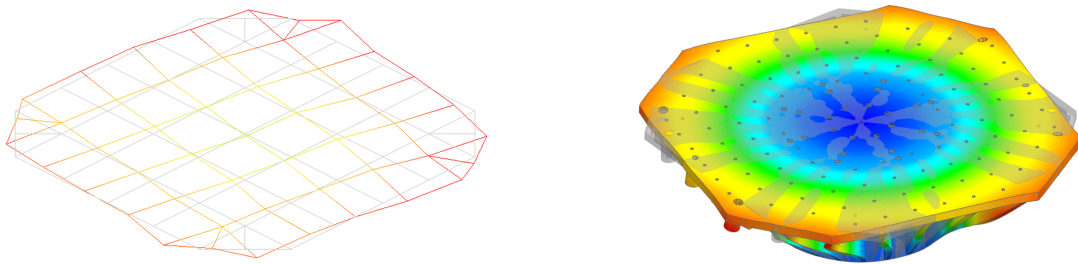


Figure 4.55: Experimental mode at 240 Hz (left), numerical mode at 484 Hz (right).

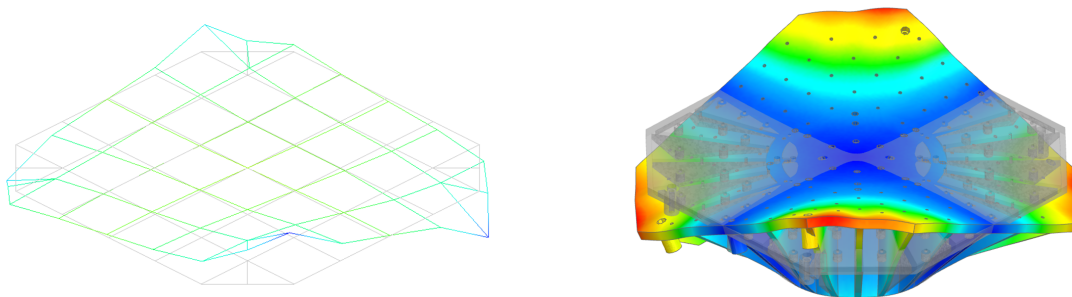


Figure 4.56: Experimental mode at 536 Hz (left), numerical mode at 681 Hz (right).

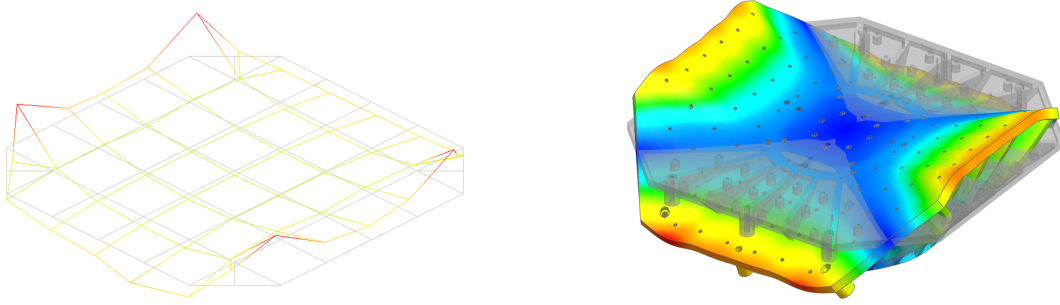


Figure 4.57: Experimental mode at 610 Hz (left), numerical mode at 807 Hz (right).

Coupling of the numerical model to the shaker model

Finally, a superelement of the expander and its load support is created in order to couple it to the shaker model. This is done in the exact same manner as without the load support and the same points as previously are included in the model (the four accelerometer points represented in Figure 4.47a).

By introducing this superelement in *Simulink*, the dynamics of the shaker/expander/load support assembly can be simulated. The synthesised FRFs can then be compared to the ones obtained with the sine sweep tests.

The conclusions being quite the same for the four accelerometers, only the acceleration-over-current and acceleration-over-voltage FRFs related to the *Right* accelerometer are displayed here. These are respectively shown in Figure 4.58a and 4.58b. The shape of the curves is well approximated by the virtual shaker but the frequencies are not. But this result was expected since the specimen was not perfectly modelled (cf. Table 4.7).

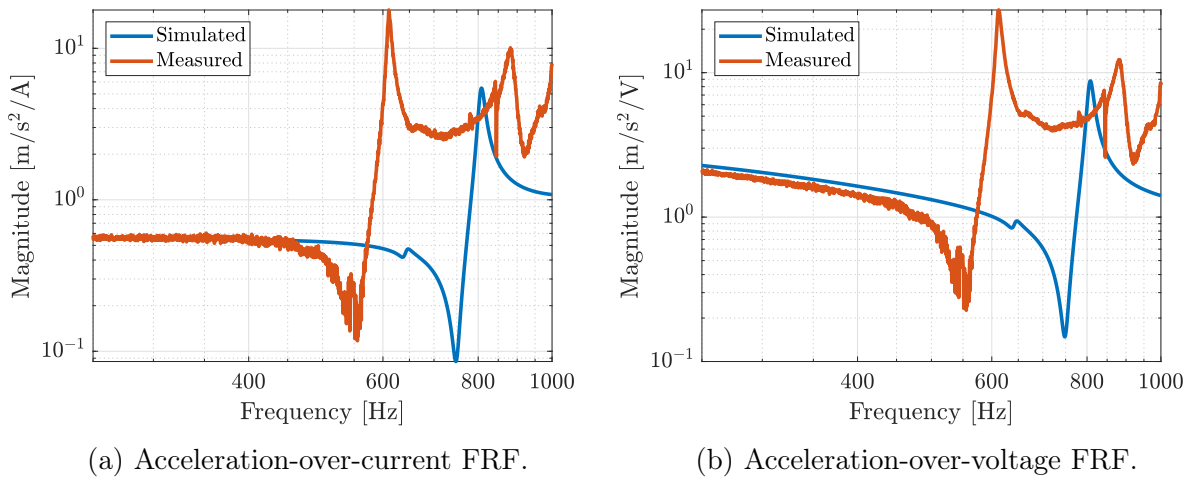


Figure 4.58: Expander and its load support fixed on the shaker, acceleration at the expander table extremity: comparison between measured and simulated FRFs.

4.4 Conclusion

To couple the model of the specimen to the numerical model of the shaker, the specimen has been modelled in two different ways. The first one is to use a numerical superelement and the second, an experimental superelement.

The numerical coupling of the specimen to the shaker model gives satisfying results for the smallest shaker. All the resonance peaks are not identified but the matching modes have frequencies close to the measured ones. For the largest shaker, even if there is a non-negligible error on the natural frequency estimations and that the comparison between experimental and numerical modes are not satisfying, the simulated results are still interesting. Indeed, not all the modes are predicted by the model but it allows to predict the amplitude of the resonance peaks and to anticipate the interactions between the shaker and the specimen between 600 Hz and 1 000 Hz. The experimental coupling of the specimen to the shaker model has only been tested on the smallest 100-lbf shaker. The method must be improved but it allows to identify the frequency of some of the resonance peaks and to predict their amplitude.

After that, the load supports of the 120-kN shaker expander have been analysed. It has been shown that at high frequencies, the load support guidance stiffens the structure. Therefore, the latter has been modelled by stiffnesses in the FEM. However, it has been shown that the results are not the expected ones. The results of the experimental modal analysis of the expander with the support have not allowed to validate the model. Therefore, the introduction of the model in the shaker model to simulate a test shaker is not conclusive either.

Chapter 5

Conclusion and perspectives

Conclusion and main results

Throughout this work, a virtual shaker model has been developed. The aim was to virtually simulate an entire vibration test. This has been performed in several steps. The first stage was to model an electromechanical shaker. The second one was to couple the model of a specimen to the model of the shaker. In this perspective, different methodologies have been theoretically proposed, and then applied on practical cases. Finally, experimental measurements have been taken to validate these methods. The final goal was to build a complete virtual shaker model of a large 120-kN shaker mounted in V2i lab.

In the state-of-the-art, the different components of an electrodynamic shaker have been presented to understand its operation. After that, the lumped parameter model of the shaker could be built. The shaker has been modelled by three degrees of freedom: one for the shaker table, one for the coil and one for the shaker body.

Thereafter, a suitable method has been developed to identify the parameters of the lumped mass model. When applying a sine sweep on the shaker of interest, the acceleration of the table, the voltage and the current of the coil have been recorded. An empty test and a loaded test have been performed, and based on their acceleration-over-current FRFs, the natural frequencies of the shaker have been obtained. Thanks to these measurements, the mechanical parameters have been identified. The electrical parameters have then been defined by performing an optimization of the difference between experimental and simulated curves. The results of the simulation have finally been compared to experimental results so that it was possible to validate the method.

The last chapter was dedicated to the second step of the virtual shaker testing design which was to couple the model of a specimen to the shaker model. Two different methods have been used. The first one consisted in building a numerical model of the specimen.

A finite element model has been developed and, by using a superelement, the numerical model has been reduced then coupled to the model of the shaker. The accelerations-over-current FRFs have finally been simulated and have been compared to the FRFs resulting from the sine sweep tests. This method has appeared to work well on a small shaker but less accurately on a larger shaker. Indeed, the natural frequencies obtained with the model were not the same than the measured ones and not all the modes were identified. After that, a second method has been presented. This time, an experimental model of the specimen was built thanks to the frequency-based substructuring. An experimental superelement has been coupled to the lumped mass model of the shaker. Thanks to this coupling, the accelerations-over-current FRFs could be simulated. In order to compare them to experimental ones, a sine sweep test has been performed with the concerned specimen fixed on the shaker. This has allowed to demonstrate that this method works rather well for small shakers but has not been tested on the largest one.

In the last chapter, the studied specimen was the expander. This piece has been largely studied as well as its load support guidance. Its mode shapes have been analysed with and without its load support. It has been shown that, even if the comparison between the experimental and numerical results was not fully satisfying, it allowed to predict the shapes of the modes and the coupling that can appear between the shaker and its device under test. The frequencies of resonance that are identified are not exactly the expected ones but it allows to say that beyond a certain frequency, there is a resonance phenomenon between the shaker and the expander.

Perspective for future works

At first, the complexity of the lumped parameter model of the shaker could be improved. In this work, only the vertical degrees of freedom of the lumped masses have been used. The transverse effects were neglected. However, it has been shown that the table of the shaker undergoes transverse accelerations. In a future work, the torsion and plane rotations could be added to the degrees of freedom. This has not been done in this work because it would have added a lot of difficultly identified additional parameters. For the first part of this work, the presented lumped-mass model was sufficient to model the shaker and to virtually test small masses. However, it has been shown later that it was not sufficient anymore when a large mass was fixed on the shaker. These additional degrees of freedom should be added to the model. Therefore, an idea that could be used to identify the rotational parameters is to perform sine sweep test campaigns with an off-centred mass. This could be done with an eccentricity along the x -axis, then in the y -axis and by comparing measured and simulated FRFs, the parameters could be optimised. The tilting modes of the shaker table could thus be identified.

Secondly, in this study, a lumped-mass model has been used but a more complex model could be developed. Indeed, the table of the shaker was considered to be rigid but it could be integrated entirely with a CAD model. The method presented to numerically couple a specimen to the model of the shaker could be used and the superelement of this table would be coupled to the lumped-mass model. Consequently, the latter would only contain the masses of the coil and of the body of the shaker. However, to do so, it is needed to have access to the coil in order to take measurements for the validation of the method but this was not possible in the scope of this work.

Moreover, the expander and its load support guidance have been modelled manually. Indeed, the parameters involved in the model have been identified through trials and errors. By lack of time, an automated method has not been developed. An optimization of these parameters would have been very time-consuming. To do such an identification, initial parameters first have to be fixed. Then one parameter must be varied. A derivative is computed between the results with the previous parameter and with the new one to determine if this parameter needs to be increased or decreased to improve the results. This must be done for each parameter entering in the model. The computation of the superelement would then be done twice per iteration. With the knowledge that the computation of the superelement can take between 15 and 50 minutes, it is clear that these calculations can take several days.

Finally, to complete the virtual shaker testing, the model of the controller could be added. The loop of the VST could be closed by the controller and a test campaign could be entirely simulated.

Appendices

Appendix A

Shaker specifications

In this work, two shakers are used to experimentally validate the methodology developed: the 120-kN DongLing shaker and the VTS VG-100 shaker. Their specifications are gathered in the Table A.1. This table allows to determine the feasibility of a test.

Characteristics		VTS VG-100 (445 N)	DongLing (120 kN)	
Freq. Range [Hz]		[5, 4500]	[5, 3000]	
Max peak force [kN]		0.1	120.0	
Max RMS force [kN]		0.1	120.0	
Max shock force [kN]		0.2	240.0	
Max acc. [g]	shaker	150.0	100.0	
	shaker + exp.	?	48.0	
	shaker + table	?	84.0	43.0
Max velocity [m/s]		2.54	2.0	
Max disp. [mm] (0-p)		19.05	38.0	
Moving mass [kg]		0.240	72.0	
Driver bar [kg]		/	/	/
Slip table [kg]		/	71.0	203.0
Head expander [kg]		/	174.0	
Admissible mass [kg]		?	1000.0	
Admissible torques [Nm]	pitch	?	3300.0	108600.0
	roll	?	3600.0	123700.0
	yaw	?	200.0	47400.0
	coil	?	2500.0	

Figure A.1: Shaker specifications.

Appendix B

LSCE method

This section explains how the natural frequencies and the damping coefficients of a structure are computed based on IRFs expression. The IRF related to coordinates r and s for the j^{th} sample of time can be expressed as [20]:

$$h_{rs}(j\Delta t) = 2Re \left(\sum_{k=1}^n A_{rs(k)} e^{\lambda_k(j\Delta t)} \right) \quad (B.1)$$

$$= 2Re \left(\sum_{k=1}^n A_{rs(k)} Z_k^j \right) \quad (B.2)$$

where $Z_k = e^{\lambda_k \Delta t}$ is related to the pole of mode k and $A_{rs(k)}$ is the residue of mode k associated to coordinates r and s . The complex conjugate pairs Z_k must then be determined.

These are considered as the roots of a polynomial of degree $q = 2n$ and are obtained using Prony's method:

$$\alpha_0 + \alpha_1 Z + \alpha_2 Z^2 + \dots + \alpha_q Z^q = 0 \quad (B.3)$$

If each p^{th} equation is multiplied by α_p and that they are then all added, it follows that:

$$\sum_{p=0}^q \alpha_p h_{rs}(p\Delta t) = 2Re \left(\sum_{k=1}^n A_{rs(k)} \sum_{p=0}^q \alpha_p Z_k^p \right) = 0. \quad (B.4)$$

To avoid the solution $\alpha = 0$, the last coefficient is imposed to be equal to 1: $\alpha_q = 1$. Therefore, the following equation is obtained:

$$\sum_{p=0}^{q-1} \alpha_p h_{rs}(p\Delta t) = 2Re \left(\sum_{k=1}^n A_{rs(k)} \sum_{p=0}^{q-1} \alpha_p Z_k^p \right) = 0. \quad (B.5)$$

These coefficients α can be estimated by using the measured impulse responses. If

$n_t \gg q$ measured values are considered, the following undetermined system is obtained:

$$\underbrace{\begin{bmatrix} h_{rs}(0) & h_{rs}(\Delta t) & \cdots & h_{rs}((q-1)\Delta t) \\ h_{rs}(\Delta t) & h_{rs}(2\Delta t) & \cdots & h_{rs}(q\Delta t) \\ \vdots & \vdots & \cdots & \vdots \\ h_{rs}((n_t-1)\Delta t) & h_{rs}(n_t\Delta t) & \cdots & h_{rs}((n_t+q-2)\Delta t) \end{bmatrix}}_{\mathbf{A}} \underbrace{\begin{Bmatrix} \alpha_0 \\ \alpha_1 \\ \vdots \\ \alpha_{q-1} \end{Bmatrix}}_{\mathbf{x}} = \underbrace{\begin{Bmatrix} -h_{rs}(q\Delta t) \\ -h_{rs}((q+1)\Delta t) \\ \vdots \\ -h_{rs}((n_t+q-1)\Delta t) \end{Bmatrix}}_{\mathbf{b}}$$

This LSCE method can be extended to the pLSCE method ([25], [27]) as described in Equation B.6 where N_o is the number of outputs, i.e., three times the number of accelerometers if they measure in the three directions, and N_i is the number of inputs, i.e., the number of impacts.

$$\underbrace{\begin{bmatrix} \mathbf{h}_1(0) & \mathbf{h}_1(\Delta t) & \cdots & \mathbf{h}_1((q-1)\Delta t) \\ \vdots & \vdots & \cdots & \vdots \\ \mathbf{h}_1((n_t-1)\Delta t) & \mathbf{h}_1(n_t\Delta t) & \cdots & \mathbf{h}_1((n_t+q-2)\Delta t) \\ \mathbf{h}_2(0) & \mathbf{h}_2(\Delta t) & \cdots & \mathbf{h}_2((q-1)\Delta t) \\ \vdots & \vdots & \cdots & \vdots \\ \mathbf{h}_2((n_t-1)\Delta t) & \mathbf{h}_2(n_t\Delta t) & \cdots & \mathbf{h}_2((n_t+q-2)\Delta t) \\ \vdots & \vdots & \cdots & \vdots \\ \mathbf{h}_{N_o}(0) & \mathbf{h}_{N_o}(\Delta t) & \cdots & \mathbf{h}_{N_o}((q-1)\Delta t) \\ \vdots & \vdots & \cdots & \vdots \\ \mathbf{h}_{N_o}((n_t-1)\Delta t) & \mathbf{h}_{N_o}(n_t\Delta t) & \cdots & \mathbf{h}_{N_o}((n_t+q-2)\Delta t) \end{bmatrix}}_{\mathbf{A}} \underbrace{\begin{Bmatrix} \alpha_0 \\ \alpha_1 \\ \vdots \\ \alpha_{q-1} \end{Bmatrix}}_{\mathbf{x}} = \underbrace{\begin{bmatrix} -\mathbf{h}_1(q\Delta t) \\ \vdots \\ -\mathbf{h}_1((n_t+q-1)\Delta t) \\ -\mathbf{h}_2(q\Delta t) \\ \vdots \\ -\mathbf{h}_2((n_t+q-1)\Delta t) \\ \vdots \\ -\mathbf{h}_{N_o}(q\Delta t) \\ \vdots \\ -\mathbf{h}_{N_o}((n_t+q-1)\Delta t) \end{bmatrix}}_{\mathbf{B}} \quad (\text{B.6})$$

The least-squares solution is given by:

$$\mathbf{x} = (\mathbf{A}^T \mathbf{A})^{-1} \mathbf{A}^T \mathbf{b} \quad (\text{B.7})$$

The *alpha* coefficients are then determined. It is explain in section 4.1.1 how to finally compute the poles (and so the natural frequencies and the damping coefficients).

Appendix C

PolyMAX stabilisation diagram

At this time, the p-LSCE method has been used to plot the stabilisation diagrams and obtain the stabilised poles. However, in order to compare these results with a second method, the PolyMAX method can be used. Therefore, the stabilisation diagram related to the impact testing done on the expander is shown in Figure C.1.

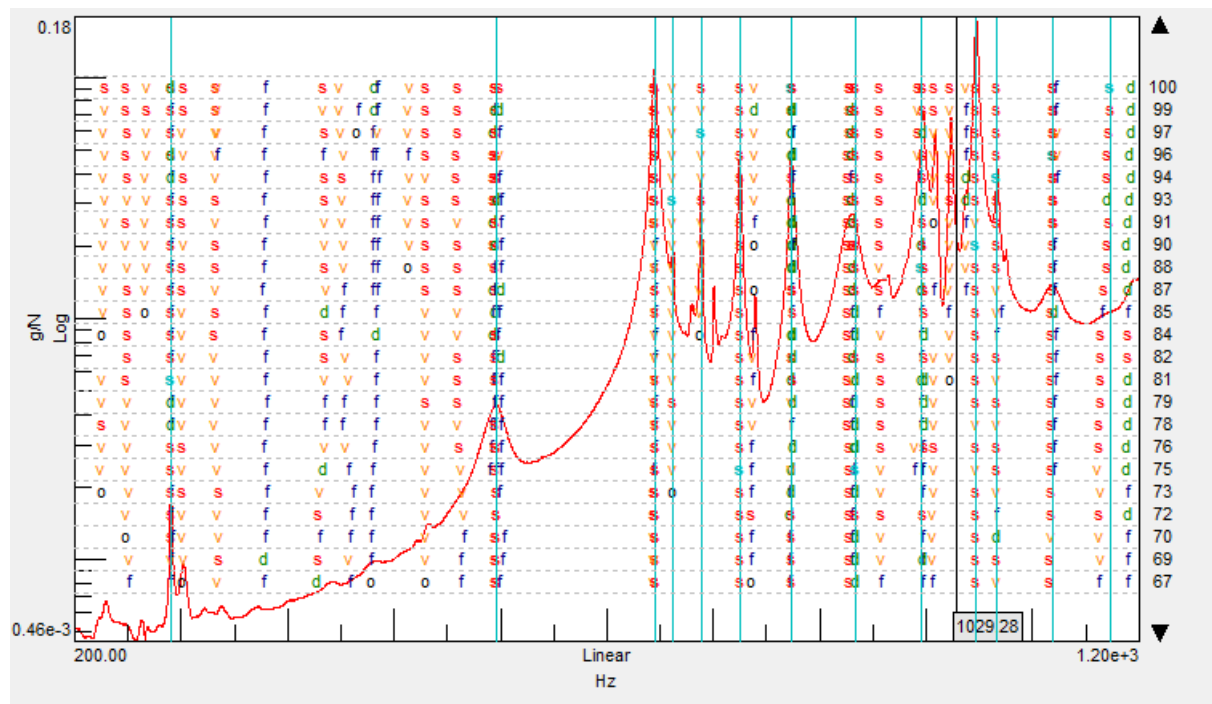


Figure C.1: Stabilisation diagram obtained with PolyMAX method.

It can be noticed that the resulting stabilised poles are very similar to those shown in Figure 4.28. The relative error computed between the natural frequencies obtained with p-LSCE and PolyMAX methods are gathered in Table C.1. This diagram is directly given by *LMS TestLab*.

	p-LSCE freq. [Hz]	PolyMAX freq. [Hz]	Relative error [%]
Mode 1	290.23	290.36	-0.03
Mode 2	598.3	596.50	0.02
Mode 3	744.4	745.28	0.1
Mode 4	825.7	825.14	0.07
Mode 5	874.9	873.56	0.15
Mode 6	927.4	933.11	-0.64
Mode 7	997.1	995.01	-0.06
Mode 8	1 046.8	1 046.73	0.01
Mode 9	1 118.47	1 118.35	0.06
Mode 10	1 197.1	1 172.98	1.63

Table C.1: High natural frequencies of the head expander fixed on the table of the shaker obtained with the impact testing.

Appendix D

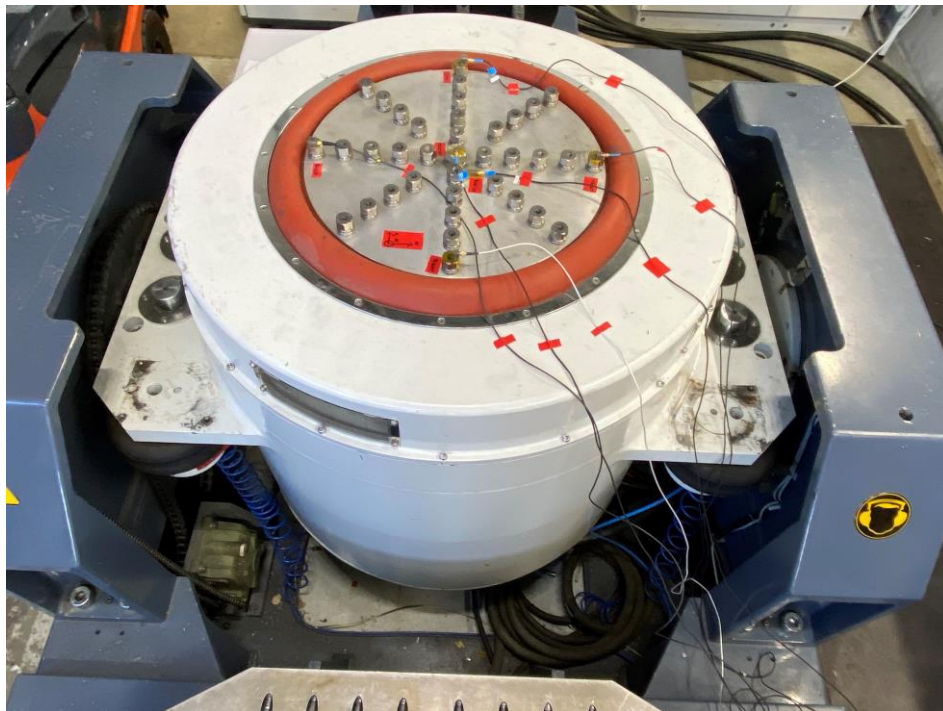
Vibration test reports

In this last appendix, a test report as it is usually done at V2i company is presented. Two test campaigns have been done on the 120-kN shaker in the scope of this work: one to validate the method used to build the shaker model and one to validate the method of coupling a specimen model to the shaker model. The reports gathering the details of both of them are shown in the following pages.

Vibration Test Report

Tested Item:

SHAKER MODEL VALIDATION



Type of test:

Sine sweeps

March 2022

Author:	C. ADAM 12/04/2022
Verification:	L. DECHAMBRE 12/04/2022

V2i s.a.

Liège Science Park
Avenue du Pré Aily, 25 – 4031 Liège - Belgium
Tél : +32-4-2871070 – Fax : +32-4-2871071
Website : www.v2i.be

V₂i



	Vibration test report Sine sweep	Report Shaker Model Test Campaign
		Date: 12/04/2022 Page: 2/4

1. Introduction

The subject of this report is to present the results of the vibration tests performed in the aim to validate the model of the 120-kN DongLing Shaker.

Since the tests are realised in open loop for a constant voltage, the tests are first performed in closed loop, by controlling the acceleration in order to determine the maximum allowable voltage to impose in the open loop test.

Two different tests are performed: with no load and with a load of 33kg.

2. Equipment Used

Electrodynamic Shaker	
Shaker:	DongLing ET-120 kN LS3 550 – 3 in. stroke
Amplifier:	SDA-120

Control and Acquisition	
Front end:	LMS Instruments SCADAS III mainframe System SCL2E20V – Serial number: 62190513
Computer:	V2i-Shaker-9

Software
LMS Test.Lab 21A for control, acquisition and post-treatment

Accelerometers						
<i>manufacturer</i>	<i>model</i>	<i>name</i>	<i>direction</i>	<i>function</i>	<i>serial number</i>	<i>calibration due date</i>
DYTRAN	3023A	Coil	triaxial	Control/ Measure	14170	21/05/2023
PCB	3023A02	Centre	triaxial	Measure	64600	23/11/2023
DYTRAN	3313A	Front	triaxial	Measure	1000	01/02/2024
DYTRAN	3023A	Left	triaxial	Measure	6532	26/08/2023
DYTRAN	3023M04T	Back	triaxial	Measure	10967	21/05/2023
DYTRAN	3313A3	Right	triaxial	Measure	15333	21/11/2023

3. Testing Procedure

3.1. Reference Axes and Vibration Tooling

In the next pages, the axes refer to the disposition described in Figure 1.

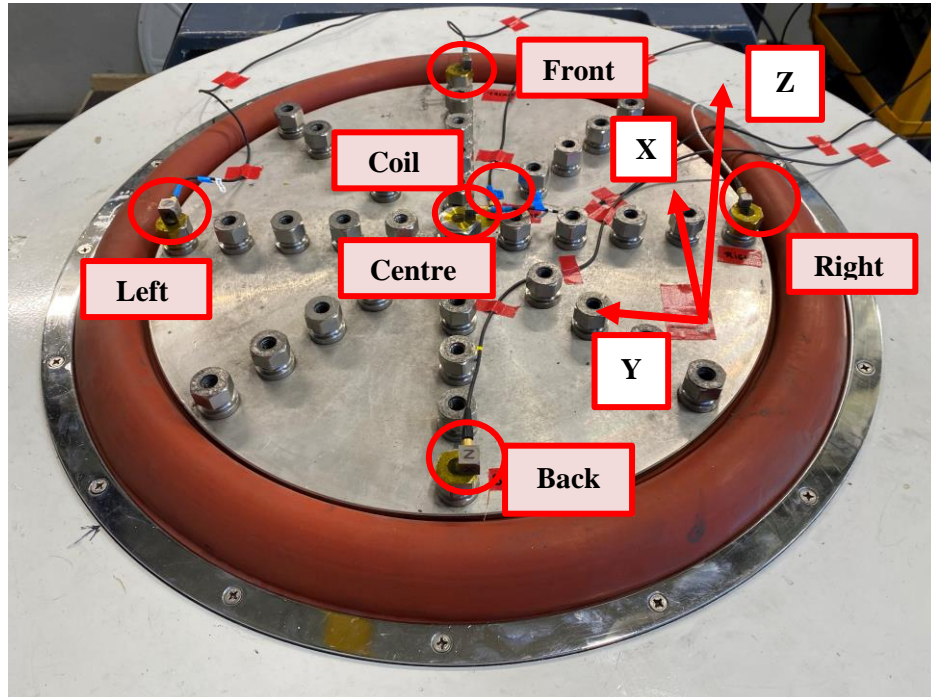


Figure 1: Definition of the empty test axes

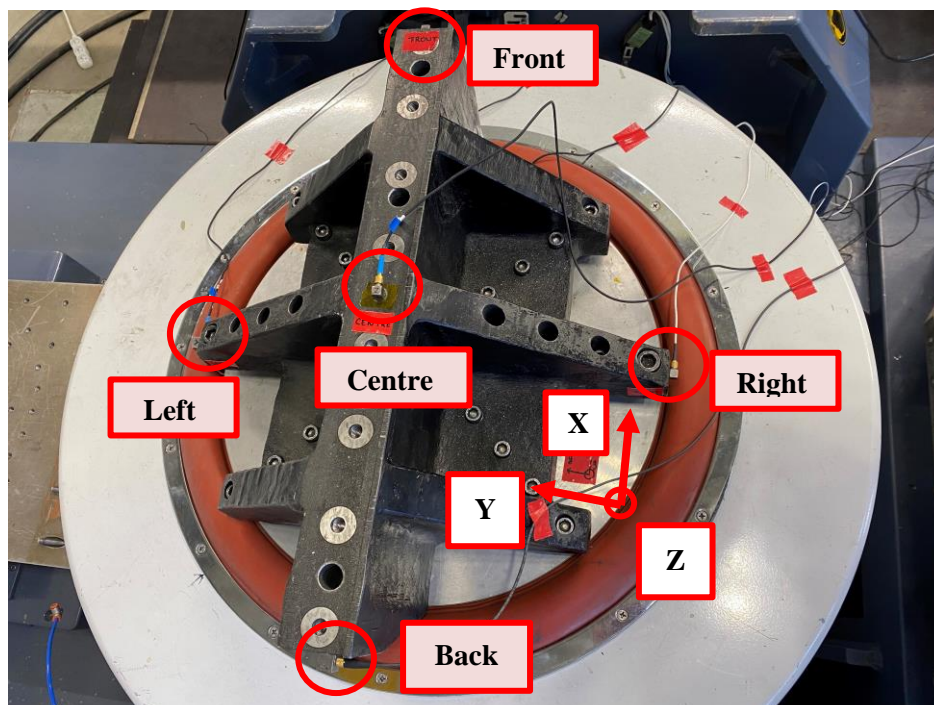


Figure 2: Definition of the 33-kg loaded test axes

In Figure 2, the “coil” accelerometer is still underneath the mass.

	Vibration test report Sine sweep	Report Shaker Model Test Campaign
		Date: 12/04/2022 Page: 4/4

3.2. Test Sequence

The chronological sequence performed on the tested item is given in Table 1

Test date	Test performed	Excitation axis
12/04/2022	Sine sweep – No mass – Close loop (0.5 g, 5 Hz – 2500 Hz)	Z
12/04/2022	Sine sweep – No mass – Close loop (0.2 g, 5 Hz – 100 Hz)	Z
12/04/2022	Sine sweep – No mass – Open loop (0.03 V, 5 Hz – 100 Hz)	Z
12/04/2022	Sine sweep – No mass – Open loop (0.15 V, 5 Hz – 100 Hz)	Z
12/04/2022	Sine sweep – No mass – Open loop (0.01 V, 5 Hz – 2500 Hz)	Z
12/04/2022	Sine sweep – No mass – Open loop (0.05 V, 5 Hz – 2500 Hz)	Z
12/04/2022	Sine sweep – With mass – Close loop (0.5 g, 5 Hz – 2500 Hz)	Z
12/04/2022	Sine sweep – With mass – Open loop (0.2 V, 5 Hz – 100 Hz)	Z
12/04/2022	Sine sweep – With mass – Open loop (0.007 V, 5 Hz – 2500 Hz)	Z
12/04/2022	Sine sweep – With mass – Open loop (0.05 V, 5 Hz – 2500 Hz)	Z

Table 1: Test sequence

3.2.1. Sine sweeps

Each of the sweeps detailed below has been applied to the tested structure in increasing direction. In order to avoid noisy measurements, the sine sweeps are performed with a higher level at low frequency. This is why there are two tables here: one for the whole frequency range and one for the low frequency range.

Frequency bandwidth	5 → 2500 Hz
Sweep rate	1 oct/min
Number of sweeps	1
Duration	9min8s
Direction	Up

Frequency bandwidth	5 → 100 Hz
Sweep rate	1 oct/min
Number of sweeps	1
Duration	4min27s
Direction	Up

Vibration Test Report

Tested Item:

SHAKER + EXPANDER MODEL VALIDATION



Type of test:

Sine sweeps

March 2022


Author:	C. ADAM 13/04/2022
Verification:	L. DECHAMBRE 13/04/2022

V₂i s.a.

Liège Science Park
Avenue du Pré Aily, 25 – 4031 Liège - Belgium
Tél : +32-4-2871070 – Fax : +32-4-2871071
Website : www.v2i.be

V₂i



	Vibration test report Sine sweep	Report Expander Test Campaign
		Date: 13/04/2022 Page: 2/5

1. Introduction

The subject of this report is to present the results of the vibration tests performed in the aim to validate the model of the expander of the 120-kN DongLing Shaker

Since the tests are realised in open loop for a constant voltage, the tests are first performed in closed loop, by controlling the tension in order to determine the maximum allowable voltage to impose in the open loop test.

Two different tests are performed: without and with the load support guidance of the expander


2. Equipment Used

Electrodynamic Shaker	
Shaker:	DongLing ET-120 kN LS3 550 – 3 in. stroke
Amplifier:	SDA-120

Control and Acquisition	
Front end:	LMS Instruments SCADAS III mainframe System SCL2E20V – Serial number: 62190513
Computer:	V2i-Shaker-9

Software
LMS Test.Lab 21A for control, acquisition and post-treatment

Accelerometers (no load support case)						
<i>manufacturer</i>	<i>model</i>	<i>name</i>	<i>direction</i>	<i>function</i>	<i>serial number</i>	<i>calibration due date</i>
DYTRAN	3023A	Coil	triaxial	Control/ Measure	14170	21/05/2023
PCB	3023A02	Centre	triaxial	Measure	64600	23/11/2023
DYTRAN	3313A	Front	triaxial	Measure	1000	01/02/2024
DYTRAN	3023A	Table	triaxial	Measure	6532	26/08/2023
DYTRAN	3023M04T	Body	triaxial	Measure	10967	21/05/2023
DYTRAN	3313A3	Right	triaxial	Measure	15333	21/11/2023

	Vibration test report Sine sweep	Report Expander Test Campaign
		Date: 13/04/2022 Page: 3/5

Accelerometers (with load support case)						
<i>manufacturer</i>	<i>model</i>	<i>name</i>	<i>direction</i>	<i>function</i>	<i>serial number</i>	<i>calibration due date</i>
DYTRAN	3023A	Coil	triaxial	Control/ Measure	14170	21/05/2023
PCB	3023A02	Centre	triaxial	Control/ Measure	64600	23/11/2023
DYTRAN	3313A	Front	triaxial	Measure	1000	01/02/2024
DYTRAN	3023A	Table	triaxial	Measure	6532	26/08/2023
DYTRAN	3023M04T	Body	triaxial	Measure	10967	21/05/2023
DYTRAN	3313A3	Right	triaxial	Control/ Measure	15333	21/11/2023
PCB	356A02	Bearing	triaxial	Measure	64633	06/07/2023
PCB	356A02	Connection	triaxial	Measure	64597	06/07/2023
PCB	356A02	Structure	triaxial	Measure	136347	06/07/2023
PCB	356A02	Isolation	triaxial	Measure	LW145493	06/07/2023

3. Testing Procedure

3.1. Reference Axes and Vibration Tooling

In the next pages, the axes refer to the disposition described in Figure 1.

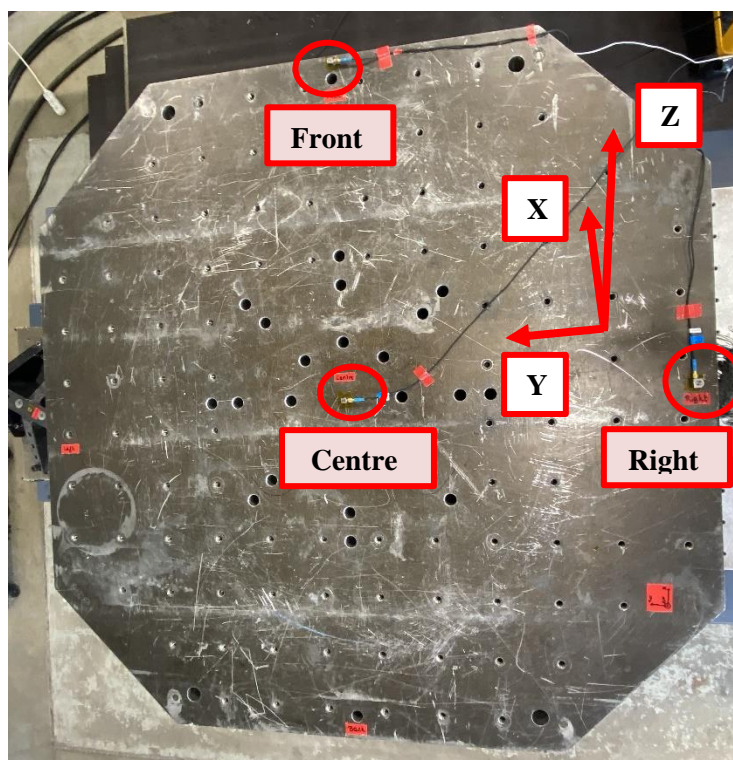
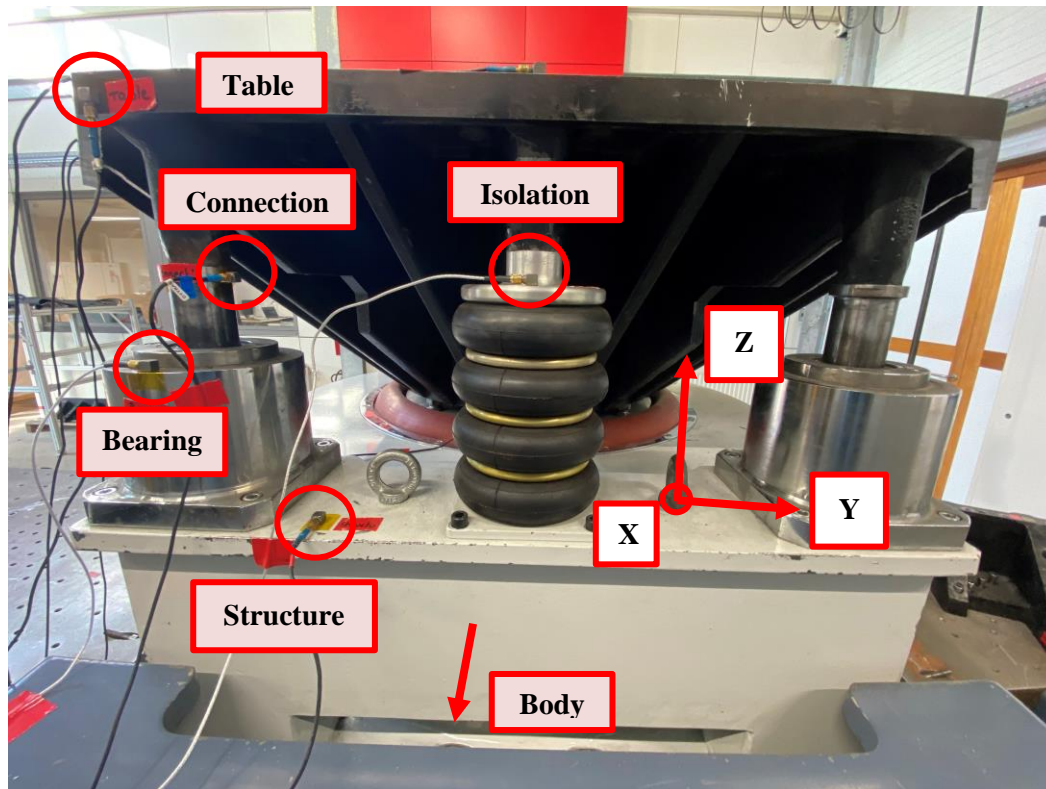


Figure 1: Definition of the empty test axes

**Figure 2: Definition of the 33-kg loaded test axes**

In Figure 1 and 2, there is a “coil” accelerometer underneath the mass.

3.2. Test Sequence

The chronological sequence performed on the tested item is given in Table 1

Test date	Test performed	Excitation axis
13/04/2022	Sine sweep – No support – Close loop (0.5 g, 5 Hz – 300 Hz)	Z
13/04/2022	Sine sweep – No support – Close loop (0.5 g, 250 Hz – 1000 Hz)	Z
13/04/2022	Sine sweep – No support – Open loop (0.01 V, 5 Hz – 1000 Hz)	Z
13/04/2022	Sine sweep – With support – Close loop (0.5 g, 5 Hz – 300 Hz)	Z
13/04/2022	Sine sweep – With support – Close loop (0.5 g, 250 Hz – 1000 Hz)	Z
13/04/2022	Sine sweep – With support – Open loop (0.1 V, 5 Hz – 300 Hz)	Z
13/04/2022	Sine sweep – With support – Open loop (0.01 V, 5 Hz – 1000 Hz)	Z

Table 1: Test sequence

3.3. Test Levels

To obtain experimental acceleration-over-current and voltage-over-current FRFs for the identification of parameters, the test campaign is realised in open-loop, with no control. However, open-loop tests may be dangerous since there is no security on the maximum acceleration that the shaker will undergo. In fact, there is a limit of table acceleration in the specifications of the shaker. Therefore, a first bench of preliminary tests is

	Vibration test report Sine sweep	Report Expander Test Campaign
		Date: 13/04/2022 Page: 5/5

performed in order to determine the maximum voltage to not exceed the defined limits. It is why some tests are performed in close-loop, imposing an acceleration and others are realised in open-loop, imposing a voltage.

For the close-loop tests, some were not able to pass. Because of the complex structure of the expander, there was a large anti-resonance peak. The controller fixed related to the accelerometer “coil” stopped the test because the acceleration at this point was larger than the defined limit. Therefore, to bypass this issue, three controllers have been defined and only the mean of the three accelerations needed to be below this limit.

3.3.1. Sine sweeps

Frequency bandwidth	5 → 1000 Hz
Sweep rate	1 oct/min
Number of sweeps	1
Duration	7min45
Direction	Up

Frequency bandwidth	5 → 300 Hz
Sweep rate	1 oct/min
Number of sweeps	1
Duration	6min7s
Direction	Up

In Figure 3, the shape of the input voltage is shown. To avoid noisy measurements at low frequency, the voltage is higher at low frequency than at high frequency. It is decreased progressively until 100 Hz and is finally set to 0.01 V.

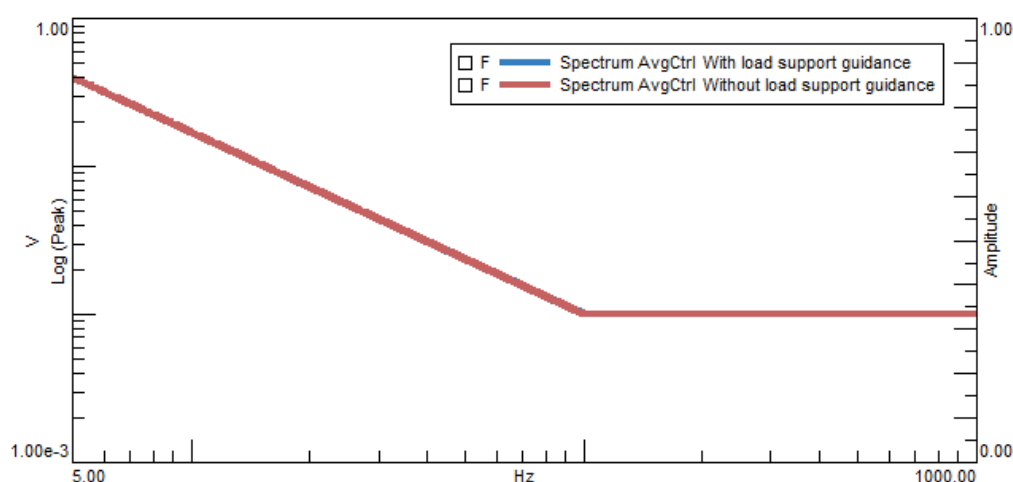


Figure 3: Shape of the input voltage

Bibliography

- [1] J. Martino and K. Harri. “The shaker parameters estimation, a first step to virtual testing”. In: *MATEC Web of Conferences*. Vol. 148. Edp Sciences. 2018, p. 05003.
- [2] G. F. Lang, D. Snyder, et al. “Understanding the physics of electrodynamic shaker performance”. In: *Sound and vibration* 35.10 (2001), pp. 24–33.
- [3] G. F. Lang. “Electrodynamic shaker fundamentals”. In: *Sound and vibration* 31.4 (1997), pp. 14–23.
- [4] N. Tiwari, A. Puri, and A. Saraswat. “Lumped parameter modelling and methodology for extraction of model parameters for an electrodynamic shaker”. In: *Journal of Low Frequency Noise, Vibration and Active Control* 36.2 (2017), pp. 99–115.
- [5] M. Remedias et al. “Virtual testing: a pre-and post-test tool for base-driven space-craft testing”. In: *Aerospace Testing Seminar*. 2017.
- [6] S. Hoffait et al. “Virtual shaker testing at V2i: measured-based shaker model and industrial test case”. In: *Conference proceedings of ISMA2016-USD2016*. 2016.
- [7] S. Hoffait, F. Marin, D. Simon, J.-C. Golinval. “Virtual Shaker Testing: development and application to assess control strategy issues”. In: *Analyse vibratoire Expérimentale* (2016).
- [8] B. K. Thoen et al. “Controller upgrade for the HYDRA hydraulic shaker facility”. In: *12th European Conference on Spacecraft Structures, Materials and Environmental Testing*. Vol. 691. 2012, p. 79.
- [9] J. Martino and K. Harri. “Virtual shaker modeling and simulation, parameters estimation of a high damped electrodynamic shaker”. In: *International Journal of Mechanical Sciences* 151 (2019), pp. 375–384.
- [10] S. Manzato et al. “Validation of a Virtual Shaker Testing approach for improving environmental testing performance”. In: *Proceedings of the ISMA*. 2014, pp. 1169–1181.
- [11] S. Waimier et al. “Modelling and experimental validation of a coupled electrodynamic shaker and test structure simulation model”. In: *Proceedings of the 27th International Conference on Noise and Vibration Engineering, Leuven*. 2016.
- [12] S. Ricci et al. “Virtual shaker testing: a novel approach for improving vibration test performance”. In: *Proceedings of ISMA 2008: international conference on noise and vibration engineering, vols. 1-8*. Katholieke univ Leuven, Dept Werktuigkunde. 2008, pp. 1767–1782.

- [13] S. Hoffait et al. “Measured-based shaker model to virtually simulate vibration sine test”. In: *Case Studies in Mechanical Systems and Signal Processing* 4 (2016), pp. 1–7.
- [14] G. Coppotelli et al. “Challenges of coupling effective masses and shaker models for virtual shaker testing”. In: *AIAA Scitech 2020 Forum*. 2020, p. 1444.
- [15] L. Martini. “Real-time control of an electrodynamic shaker”. MA thesis. University of Bologna, 2015.
- [16] P. S. Varoto and L. P. R. de Oliveira. “On the force drop off phenomenon in shaker testing in experimental modal analysis”. In: *Shock and Vibration* 9.4, 5 (2002), pp. 165–175.
- [17] Leandro Della F. and H. A. Grundling. “Design of a robust model reference adaptive voltage controller for an electrodynamic shaker”. In: *Eletronica de Potencia* 13.3 (2008), pp. 133–140.
- [18] PROSTER. *Digital LCR Tester Manual*. English. 21 pp.
- [19] A. Brandt and K. Ahlin. “Sampling and time-domain analysis”. In: *Sound and vibration* 44.5 (2010), pp. 13–17.
- [20] J.-C. Golinval. *Vibration testing and experimental modal analysis*. 2021.
- [21] A. Girard and N. A. Roy. “Modal effective parameters in structural dynamics”. In: *Revue Européenne des éléments finis* 6.2 (1997), pp. 233–254.
- [22] T. Irvine. “Effective modal mass and modal participation factors”. In: *Available on the web on site: <http://www.vibrationdata.com/tutorials2/ModalMass.pdf>. (last access on march 7 2007)* (2013).
- [23] Siemens. “Modal effective parameters in structural Digital Signal Processing Knowledge booklet”. In: *Testing Knowledge Base compilation* (2019), pp. 75–87.
- [24] C. Adam. *Experimental modal analysis of a plane structure*. University of Liège, 2021.
- [25] LMS international. *Theory and Background*. 2000.
- [26] M. Afshar and S. Khodaygan. “Enhanced stabilization diagram for automated modal parameter identification based on power spectral density transmissibility functions”. In: *Structural Control and Health Monitoring* 26.7 (2019), e2369.
- [27] A. Amorosi. “Development of an automated impact testing modal analysis procedure using revised algorithms and laser vibrometry”. MA thesis. Université de Liège, 2020.
- [28] S. Hoffait, J. Ligot, M. Bertha, S. Moschini, D. Simon, J.-C. Golinval. “The poly-reference least square complex frequency identification revised to improve damping estimation”. In: *Aero+* (2019).
- [29] B. Peeters et al. “The PolyMAX frequency-domain method: a new standard for modal parameter estimation?” In: *Shock and Vibration* 11.3-4 (2004), pp. 395–409.

- [30] M. Pastor, M. Binda, and T. Harčarik. “Modal assurance criterion”. In: *Procedia Engineering* 48 (2012), pp. 543–548.
- [31] J.-C. Golinval. *Theory of vibration*. 2020.
- [32] M. Géradin and D. J. Rixen. *Mechanical vibrations: theory and application to structural dynamics*. John Wiley & Sons, 2014.
- [33] E. A. Pasma et al. “Frequency based substructuring with the virtual point transformation, flexible interface modes and a transmission simulator”. In: *Dynamics of Coupled Structures, Volume 4*. Springer, 2018, pp. 205–213.
- [34] R. G. Budynas and J. K. Nisbett. *Mechanical Engineering Design de Shigley*. 2017.
- [35] G. Kerschen. “On the model validation in nonlinear structural dynamics”. PhD thesis. ULg-Université de Liège, 2002.